

Polarization modeling and predictions for DKIST, part 9: flux distribution with FIDO

David M. Harrington,^{a,*} Friedrich Wöger,^b Amanda J. White^{ORCID},^{b,c} and
Stacey R. Sueoka^a

^aNational Solar Observatory, Makawao, Hawaii, United States

^bNational Solar Observatory, Boulder, Colorado, United States

^cUniversity of Colorado, Department of Astrophysical and Planetary Sciences,
Boulder, Colorado, United States

Abstract. Astronomical instruments greatly improve wavelength multiplexing capabilities by using beam splitters. In the case of the 4-m National Science Foundation’s Daniel K. Inouye Solar Telescope (DKIST) solar telescope, over 70 W of optical power is distributed simultaneously to four instruments, each with multiple cameras. Many DKIST observing cases require simultaneous observations of many narrow bandpasses combined with an adaptive optics system. The facility uses five dichroic optical stations to allow at least 11 cameras and two wavefront sensors to simultaneously observe ultraviolet to infrared wavelengths with flexible reconfiguration. The DKIST dichroics required substantial development to achieve very tight specifications over very large apertures of 290 mm diameter. Coating spectral variation occurs over <1 nm wavelength, comparable with instrument bandpasses. We measure retardance spectral variation of up to a full wave and diattenuation varying over $\pm 10\%$ per nm. Spatial variation of Mueller matrix elements for coatings in both transmission and reflection requires careful metrology. We demonstrate coatings from multiple vendors exhibit this behavior. We show achievement of 5-nm root mean square (RMS) reflected wavefront and 24-nm RMS power with coatings over $8\ \mu\text{m}$ thick. We show mild impacts of depolarization and spectral variation of polarization on modulation efficiency caused by the dichroic coatings. We show an end-to-end system polarization model for the visible spectropolarimeter instrument, including the dichroics, grating, analyzer, and all coated optics. We show detailed performance for all DKIST dichroics for community use in planning future observations. © *The Authors. Published by SPIE under a Creative Commons Attribution 4.0 International License. Distribution or reproduction of this work in whole or in part requires full attribution of the original publication, including its DOI.* [DOI: [10.1117/1.JATIS.7.4.048005](https://doi.org/10.1117/1.JATIS.7.4.048005)]

Keywords: instrumentation; polarization; Mueller matrix; National Science Foundation’s Daniel K. Inouye Solar Telescope.

Paper 21118 received Sep. 14, 2021; accepted for publication Dec. 7, 2021; published online Dec. 28, 2021.

1 Introduction: DKIST and Polarization Models for Calibration

The National Science Foundation’s Daniel K. Inouye Solar Telescope (DKIST) on Haleakalā, Maui, Hawai’i, is presently ending the construction phase and beginning early operations. A recent summary is in Ref. 1. The 4.2-m-diameter off-axis $F/2$ primary mirror folds a 4.0-m-diameter circular beam. Four separate spectropolarimeters (SPs) are being installed in the coudé laboratory, each with multiple sensors of various imaging capabilities and wavelength ranges. All instruments have spectral resolving power $>30,000$ to over 300,000. Each instrument has optomechanical methods to scan the instrument sensor field of view (FoV) across a much larger portion of the DKIST beam. All instruments deliver imaging spectropolarimetry of some kind either by scanning wavelengths with Fabry–Perot systems, stepping slit masks across a focal plane, tilting field scanning mirrors near pupil planes, and/or using imaging fiber bundles. These techniques build up imaging spectropolarimetric capability over visible and near-infrared

*Address all correspondence to David M. Harrington, dharring96@gmail.com

wavelengths. DKIST is specified to be able to operate at least 11 cameras simultaneously. The sensors typically run at frame rates of a few Hz to >40 Hz. This multi-instrument operation achieves the combined spatial, spectral, and temporal polarimetric goals.

DKIST uses six mirrors to relay light to a rotating coudé laboratory to provide flexible capabilities.^{2–10} The first two mirrors, comprising the off-axis Gregorian telescope, are static with respect to the alt/az telescope mount. DKIST has a Gregorian Optical System (GOS) with calibration, apertures, and targets built around the Gregorian focus. The GOS also contains retarders, polarizers, and artificial light sources at other levels.^{7,11–16} Four polarimetric instruments presently spanning the 380- to 5000-nm wavelength range are in various phases of construction or installation on the summit in the coudé lab. The visible spectropolarimeter (ViSP) is a three-arm slit-based SP. The diffraction-limited near-infrared spectropolarimeter (DL-NIRSP) is a fiber-bundle fed imaging SP. The cryogenic near-infrared spectropolarimeter (Cryo-NIRSP, CN) is a slit-based infrared optimized system. The visible tunable filter (VTF) is planned to begin installation soon as a tunable Fabry–Perot-type imaging SP.^{17,18} DKIST also has two high speed (30 Hz) 4K full frame cameras within the visible broadband imager red and blue instruments (VBI-red and VBI-blue, recently achieving first light as shown in Ref. 19),^{20–26} The DKIST active optics system and adaptive optics systems (AO) coordinate alignment of the beam.^{4,6,27–31} As construction progresses, the mirror controllers can position their mirrors based on lookup tables that calculate the best position based on telescope elevation, azimuth, temperature, and temperature gradient across M1.²⁷ For now, the mirrors are only positioned to a single static position with beam pointing variations as the system changes azimuth, elevation, and coudé table angle as a reasonable alignment.

Three static mirrors level and collimate the beam in the coudé laboratory (M7 through M9). CN can receive all wavelengths to 5000 nm and beyond using a pick-off mirror called M9a insertable after M9. This current M9a optic excludes CN from simultaneous use of the AO system. We note that an upgrade to allow simultaneous use of CN with other instruments is in progress. If M9a is not inserted in the beam, the 10th mirror (M10) is the deformable mirror (DM) for the AO system. Following the DM, a sequence of dichroic beam splitters (BS), windows, and/or mirrors called the facility instrument distribution optics (FIDO) allows changing of instrument configurations on a timescale of less than half an hour. The FIDO optics allow simultaneous operation of three polarimetric instruments optimized for 380 to 1800 nm while using the facility AO system for correction to provide diffraction-limited performance.^{7,8,18,29,32} All AO-assisted instruments see the first beamsplitter in the wavefront correction system (WFC-BS1) in transmission. The optics are designed such that the wedge angles are matched in each optic, and every instrument sees either two or four beamsplitters in transmission to compensate for the wedge and associated wavelength variation in beam deflection.

All instruments are supported by the DKIST data center. The center can receive and calibrate an expected 8 TB of data on an average day.^{33–35} We refer the reader to recent papers outlining the various capabilities of the first-light instruments.^{3,5,7,8,36} Complex polarization modulation and calibration strategies are required for multi-instrument astronomical systems.^{7,8,11,12,37,38} Accurate polarimetry is a key design driver. The planned 4-m on-axis European Solar Telescope will also require similar calibration considerations.^{39–41} Many solar and night-time telescopes have performed polarization calibration of complex many-mirror pathways.^{42–65}

This paper continues a series deriving polarization performance expectations for the DKIST telescope and instruments. In Ref. 66, we outlined the DKIST optical layout and system Mueller matrix properties when using a simple enhanced silver mirror coating model. In Ref. 67, we showed polarization calibrations of a night time telescope with a ViSP using the daytime sky.

Spectral interference fringes also adversely impact polarization accuracy for astronomical instruments requiring optical fringe modeling and/or removal methods through design and data processing.^{52,53,64,68–80} In Ref. 81, we applied the Berreman calculus^{82,83} to polarization fringes formed in multilayer crystals with predictions and data collected in the lab and at a solar telescope. We then extended this calculus in Ref. 81 to include fringe magnitude estimates in converging and diverging beams. We designed and built several newly upgraded polarization optics based on polycarbonate and optically contacted crystal designs in Ref. 84. These retarders

suppress polarization fringes by one to three orders of magnitude compared with the previously designed multilayer crystal optics. We also identified alignment errors between individual crystals as a major source of retarder error.

We investigated spatial variation of retardance across multilayer retarders made of polished crystals, stretched polycarbonate, and ferroelectric liquid crystals in Ref. 85. This variation was then included in the DKIST optical model to show polarization calibration errors as functions of field angle and wavelength. In Ref. 86, we extend the coating efforts of Ref. 66 to many mirror types from multiple vendors, highly enhanced metal coatings, hundred-layer dichroic coatings, and our system of BSs. We show additional mirror measurements and new ellipsometric metrology from an outside vendor (J.A. Woollam) in Ref. 87 at a range of incidence angles matching the DKIST mirrors to improve the system polarization model.

We updated our laboratory metrology equipment to measure spatial variation of transmission to better than 0.01%, polarizer contrast ratio in excess of 100,000, and orientation changes in the polarizer extinction axis at levels below 0.002 deg. We combined these polarizer imperfections with spatial variation of the calibration retarders. This includes spatial transmission variation combined with the retardance spatial variation reported previously in Ref. 85. We showed in Ref. 88 estimates for the calibration accuracy impact using our newly measured calibration polarizer optical properties including spatial variation across individual beam footprints as well as optomechanical misalignments in a Mueller matrix propagation model.

We have a dedicated metrology tool called the National Solar Observatory Coudé lab Spectro-Polarimeter (NCSP) described in Ref. 87. This system calibrates the full telescope using either our Gregorian focus calibration lamp or the solar beam itself. Preliminary calibrations match the metrology predictions very well.⁸⁷ Misalignment produces spectral oscillations in retardance. This in turn introduces coupling between temperature changes and the spectral drift of these elliptical retardance oscillations. We showed in Ref. 87 detection of the clocking oscillations outlined in Ref. 84 with calibrations both on-sun and with the DKIST calibration lamp. We also showed in Ref. 87 successful on-sun use of the optically contacted calibration retarder and system calibration with time-efficient calibration sequences.

In this paper, we detail design and fabrication issues in the dichroic coatings and substrates on very large (290 mm) apertures used in the DKIST BSs. Very tight reflected and transmitted wavefront specifications were driven by the need to minimize noncommon path wavefront errors post-AO correction as well as to preserve focus and multi-instrument bore-sighting. Reflected wavefront irregularity is below 10-nm root mean square (RMS) with reflected power <24-nm RMS. Transmitted wavefront irregularity is below 4.5 nm RMS with the same or better power. We show coatings up to 104 layers and over 8.3- μ m thick designed for low diattenuation and several aspects of polarization calibration. Narrow spectral features are present with optical full-width half-maximum (FWHM) features smaller than 0.2 nm. These narrow spectral features can be over 10% diattenuation, a full wave of retardance and 30% transmission. Typical metrology tools at >1 nm resolving power (slit band width) are not capable of measuring and alerting the buyer of very large polarization issues. High-performance instruments can see polarization aberrations from a number of sources including noncollimated beams and asymmetric coatings^{89–93} with recent studies pointing out that dichroic coatings can create polarization aberrations⁹⁴ in large missions, such as NASA's HabEx, Roman (WFIRST), and LUVOIR. We report here spatial variation of all Mueller matrix components across apertures up to 290 mm with large variation of all relevant Mueller matrix terms (transmission, diattenuation, retardance, and depolarization) strongly wavelength-dependent and concentrated in these narrow spectral features. We show measurements of similar behavior for reference on other commercial dichroic coatings used in the DKIST instrument DL-NIRSP. We also show nonuniformities and spectral features from two commercial off the shelf dichroics of short-pass and long-pass from Thorlabs in the appendices.

For astronomical instruments working at high spectral resolving power in general, issues with dichroic coatings should be carefully considered. Solar instruments in particular often only measure some small bandwidth about particular spectral lines. If care is not taken with specification, design, and metrology, issues we outline as follows can become major performance issues.

2 DKIST Wavelength Multiplexing: Dichroics and Windows

Dichroic coatings are commonly designed many-layer stacks of dielectric materials optimized to reflect certain wavelengths and transmit other wavelengths. Beam samplers often use an uncoated surface Fresnel reflection to send a small percentage of all wavelengths to one system while transmitting most of the beam to other parts of the system. At DKIST, we developed a suite of coude optics including custom designed coatings to distribute various wavelengths to the multiple instruments using a series of dichroic BSs, windows, and/or mirrors. With this series of optics, we are currently able to operate 11 scientific cameras and three wavefront sensor cameras all simultaneously with great flexibility in intensity and wavelength coverage.

2.1 Optical Layout: FIDO Dichroics and Windows

The optical path for DKIST is designed to deliver a collimated beam in the rotating laboratory where the suite of dichroic and window BSs can distribute light to all instruments simultaneously. In Fig. 1(a), we show a schematic cartoon for the DKIST optical path. The 7th mirror (M7) folds the light coming into the lab to a particular convenient height with the beam parallel to the laboratory platform floor. M8 collimates the beam. M9 folds the beam toward the 10th mirror (M10) which is the AO system DM. There is a removable pickoff mirror called M9a that presently is inserted to feed CN. This station is planned to be upgraded to a dichroic BS (M9b) to allow simultaneous use of CN with all other instruments, adding two cameras to total 13 simultaneously operated. After the DM, the beam encounters the series of FIDO BS stations to distribute light to the various instruments.

Figure 1(b) shows the on-summer FIDO sequence starting with the beam incident from M9 toward the DM. The beam reflecting off the DM encounters the first BS feeding the AO system (BS1) is shown in cyan in Fig. 1(a). The three cameras within the WFC all operate near 530 to 540 nm wavelength using the uncoated first surface reflection. The rest of the FIDO coude lab stations are denoted CL x where x is a number. Station CL2 reflects toward ViSP and the blue channel of VBI. The station CL2a splits the beam between ViSP and the blue channel of VBI.

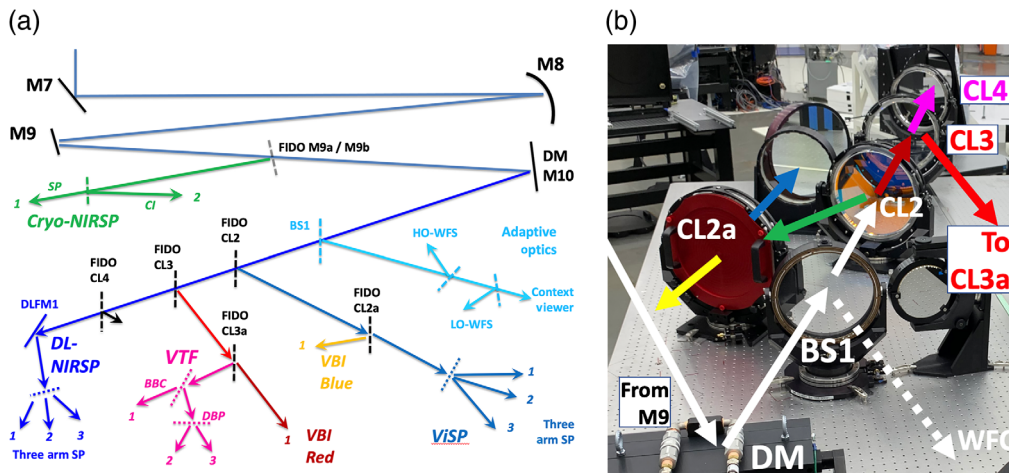


Fig. 1 (a) A DKIST coude lab cartoon layout, beginning with mirrors M7 through the DM M10. FIDO optic mounting stations CL2, CL2a, CL3, CL3a, and CL4 can be configured using a suite of mirrors, windows, and dichroics to optimize the configuration for particular use cases feeding instruments VBI red and blue, ViSP, DL-NIRSP, and VTF. The M9a mirror picks off the CN beam (planned to be a BS M9b for simultaneous use). The first beam splitter (BS1) past the DM is permanently mounted and feeds the AO system WFS and CI with an uncoated surface Fresnel reflection. (b) The main FIDO optical mounting location populated by the full 317-mm diameter optics in the DKIST coude lab. The CL3a station is out of the image off to the right. The first DL-NIRSP fold mirror is immediately behind the CL4 station. We show colored arrows representing the beam separation either reflected off of or transmitted by optics at the different CL stations to illustrate wavelength separation.

The station CL3 reflects toward station CL3a which splits the red channel of VBI and the VTF. The station CL4 currently is simply wedge compensation with a window used in transmission toward DL-NIRSP. CL4 offers possibilities for expansion to other instruments in reflection off CL4. We note that all polarimeters (ViSP, VTF, and DL) see two CL stations in transmission with compensating wedges. The two VBI channels are relatively wide field imagers and are more tolerant of some mild dispersion and displacement of the optical beam.

2.2 Science Drivers for FIDO Configurations

A key feature of DKIST is its wavelength diverse first-light instrumentation suite that covers the spectral range from 380 to 5000 nm. Each instrument is optimized for a limited wavelength range that, in many cases, partially or completely overlaps with that of other instruments in the suite. Wavelengths corresponding to particular atomic and molecular transitions encode information about, e.g., plasma motion and magnetic field properties. The simultaneous observation of many solar spectral lines using a variety of detection techniques is of vital importance for a comprehensive scientific interpretation of the data.

Several concepts have provided guidance for the design of the FIDO. An instrument should either receive all or no light within a particular bandpass to maximize the observational efficiency for the instrument that does receive the light. Coatings were optimized in the 380 to 1800 nm wavelength range. We require the ability of directing the beam with a particular bandpass into any one of the various instruments that can operate in that bandpass, depending on the scientific use case. A repositioning of FIDO elements should not require a subsequent manual realignment of the downstream instrument optics. Instruments operating at short wavelengths should be optically close to the WFC in the beam path to minimize internal seeing effects. At any time, all coude locations (CLs) need to be occupied with FIDO elements to avoid focus shifts that cannot be compensated within the instruments. The CLs for the FIDO elements were fixed in the DKIST optical design to establish the space envelopes for each instrument.

Initially, a standard set of FIDO elements was suggested that would be able to address many anticipated scientific observation use cases and feed all post-adaptive optics instruments with at least one bandpass within its operating wavelength range. With the help of an international group of scientists, the DKIST Science Working Group, the original beamsplitter suite for this standard setup was defined as:

- C-BS555: This optic was anticipated to be most often used at CL-2; when at that location it reflects the short wavelength band (<555 nm) into the VBI blue and ViSP channels, whereas all other light is transmitted.
- C-BS950: This optic was anticipated to be most often located at CL-3 in a standard configuration; when at this location, the remaining short wavelength band (<950 nm) of the light transmitted by the optic at CL-2 will be reflected into the VTF and VBI red channels, whereas the remaining infrared position of the light is transmitted into the DL-NIRSP channel.
- C-BS465: This beamsplitter was anticipated to be most often located at CL-2a, to direct the short wavelength band (<465 nm) into the VBI blue channel and transmit the remaining band into the ViSP channel.
- C-BS680: This beamsplitter was anticipated to be most often used at CL-3a to reflect the short wavelength band (<680 nm) into the VTF and transmit the remaining light into the VBI red channel.
- C-BS643: This FIDO element provides an alternate to C-BS680 (typically located at CL-3a) that reflects the short wavelength band below 643 nm thereby transmitting the scientifically important $H\alpha$ diagnostic (656.3 nm) instead of reflecting it like C-BS680 does.

Overall, choosing k optics (for the CLs) out of a group of n available FIDO elements allows to create $N = \frac{n!}{(n-k)!}$ configurations. The selected standard set described above already yields $N = 120$ theoretical arrangements of the elements, although not all of them may result in a scientifically useful light distribution.

To address additional scientific observations, further optical elements were identified as necessary to direct the DKIST science beam with a specific bandpass into a specific instrument:

- C-W1 and C-W3 are windows that are antireflective coated on both sides and can be used at any CL location.
- C-W2 is only antireflective coated on the backside to address the use case where an instrument is fed with the $\sim 3.5\%$ Fresnel reflection off the uncoated surface. In particular, this optic was anticipated to be used most often at CL-2a to leverage the VBI blue to provide context for VISP data, albeit with reduced efficiency. Yet, this optic can also be used at any other CL.
- C-M1 was needed for the ability to integrate, test, and commission instruments individually which required one mirror to ensure that all light can be directed into any instrument being integrated.

Taking into account these additional options for the four flexible CLs results in $N = 3024$ potential arrangements. Again, not all of these may be viable for use in scientific observations; however, this number demonstrates the flexibility of the FIDO design.

To support a user finding their best configuration for a given scientific observation use case, the DKIST project provides a freely distributed FIDO configuration tool. Figure 2 shows screen shots of this tool as it is used to select particular wavelengths for various instruments. Each of the narrow wavelength bands used by the instruments correspond to scientifically valuable solar diagnostics. For instance, the current DL-NIRSP filter set is listed for each of the three camera arms in the upper right corner of Fig. 2. The third camera has two choices corresponding to 1430 nm for the Si X spectral line or 1565 nm for the Fe I spectral line. VBI and VTF currently have four filters each shown in the lower middle of Fig. 2. ViSP is flexibly configured over the visible spectrum using an instrument performance calculator (IPC), so a very long list of spectral lines and the associated atoms or molecules is included and available for all three ViSP cameras. The lower left-hand corner of Fig. 2 shows a schematic for the FIDO optics and the associated wavelength range sampled with current filters available for each of the instruments. CN is not included presently as it does not currently work simultaneously with other instruments.

We note that we have several FIDO upgrades in progress. A new optic called M9b should allow relatively high reflection of IR wavelengths of CN while giving high transmission to the AO-assisted instruments at short wavelengths. We also are fabricating a suite of dichroics, which are partially reflecting in the 380 to 950 nm bandpass while preserving high transmission to the longer wavelength DL-NIRSP cameras at 950 to 1800 nm wavelengths. We are pursuing dichroic designs with 50/50, 30/70, and 70/30 relative splits between transmission and reflection to allow a flexible distribution of the same wavelength to the suite of visible wavelength instruments.

2.3 FIDO Coatings, Footprints, and Substrates

The substrate absorption features and all coating properties must be known from UV to IR wavelengths to appropriately model possible issues such as IR leaks through filters, UV damage to polymers, and heating on various optics. Many issues depend on which optics are mounted upstream. Modeling glass internal absorption is required for transmissive optics to get appropriate heat loads. We show in Table 1 the current status of dichroic and window coatings used in the transmissive optics. All the dichroics are long pass type with the notation of Coudé (C) BS followed by the transition wavelength in nanometers (465, 555, 643, 680, and 950). There are also a set of windows denoted Coudé Window (W) and then a serial number for 1, 2, 3. We note that the C-W2 optic is only back-side coated. The final optic listed is the WFC-BS1. The uncoated front surface feeds the wave front sensor while the back side is coated per Table 1.

Each coating begins with a strippable layer and then a stack of oscillating high index and low index dielectrics finished by an outer layer. The first column of Table 1 shows the dichroic or antireflection coating type. The second column shows the number of layers in the coating design. The third column shows the total physical thickness of the coating. The fourth column shows the coating run number for the final delivered optic. The fifth column shows the stack of

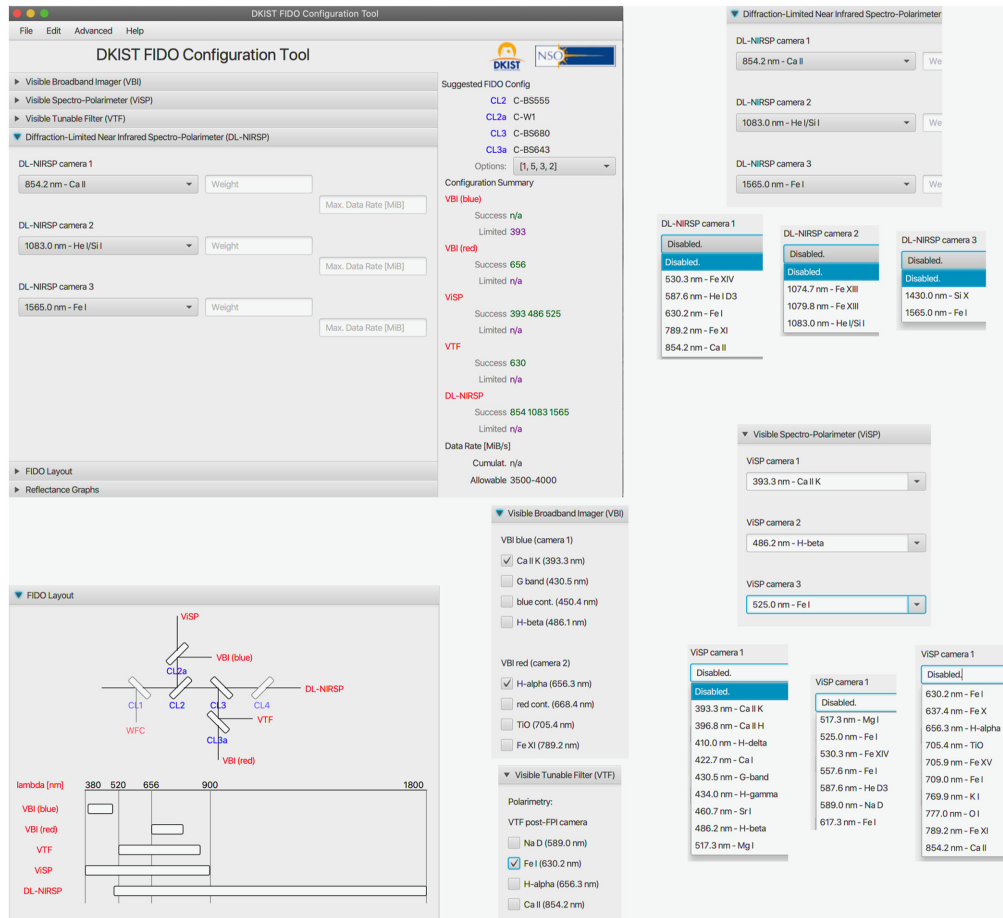


Fig. 2 Screenshots of the FIDO configuration tool used by observers during proposal preparation and submission. The main tool tab is in the upper left. The lower left shows the wavelength bands sent to the various instruments for the particular FIDO configuration. The upper right shows the three cameras of DL-NIRSP with the drop-down menus showing the filters available in the three DL camera arms. The bottom right shows the three camera arms within ViSP. As ViSP has three camera arms, all possible spectral lines are available as options for all three ViSP cameras. The ViSP IPC needs to be run to ensure proper ViSP configuration. The two screenshots near the lower middle show the VBI blue and red channel filter options along with the four VTF filter options.

high- and low-index dielectrics. The sixth column shows the material used for the thick outer layer exposed to air and physical contact. The seventh column of Table 1 shows the glass substrate material as either Heraeus Infrasil 302 or Suprasil 3002. There were issues acquiring Infrasil during the project that led to some substrates to be fabricated out of the synthetic fused silica material.

We describe in detail later how the thickness of the coatings can create spectrally narrow features in all components of the Mueller matrix both in reflection and transmission. We compute the optical thickness of the stack at 500 nm wavelength in the eighth column of Table 1. For the SiO₂-coating material, we use an index of 1.459 at 500 nm and 1.43 at 1500 nm. For the TiO₂, we use an index of 2.16 at 500 nm and 2.06 at 1500 nm. We combine the total thickness of each material in the coating stack at the appropriate refractive index and multiply by two to get the optical thickness in waves seen for a beam propagating through the entire coating stack and reflecting back through the stack to interfere at the air interface ($2dn/\lambda$).

Figure 3 shows two images of the FIDO BSs on the summit at the facility. Figure 3(a) shows the wavelength splitting for BS-555 reflecting cyan and transmitting orange. The optic is shown out of the custom interchangeable mount. Figure 3(b) shows on-sun observations with BS-555 using the 2.8 arc minute field stop. Roughly 71 W of optical power is in the beam incident on BS-555. Beam footprints and the wavelength split are obvious in the color of the optical beam.

Table 1 FIDO dichroic and window coating design properties.

Name	Layers	Thick (μm)	Run number	Stack of materials	Outer layer	Material	Waves 500 nm	Δ Wedge (arcsec)
C-BS-465	24	1.49	10-0374	$\text{SiO}_2 - \text{TiO}_2$	SiO_2	Infrasil	9.9	-0.750
WBBAR1N	16	0.78	10-0372	$\text{MgF}_2 - \text{Ta}_2\text{O}_5$	MgF_2		4.6	
C-BS-555	72	4.44	10-0362	$\text{SiO}_2 - \text{TiO}_2$	SiO_2	Infrasil	30.5	+0.022
WBBAR1N	16	0.78	10-0360	$\text{MgF}_2 - \text{Ta}_2\text{O}_5$	MgF_2		4.6	
C-BS-643	88	6.58	10-0482	$\text{SiO}_2 - \text{TiO}_2$	SiO_2	Suprasil	44.7	-0.404
WBBAR2	10	0.69	10-0481	$\text{SiO}_2 - \text{ZrO}_2$	MgF_2		5.0	
C-BS-680	104	8.04	10-0502	$\text{SiO}_2 - \text{TiO}_2$	SiO_2	Suprasil	46.8	-0.338
WBBAR2	10	0.69	10-0500	$\text{SiO}_2 - \text{ZrO}_2$	MgF_2		5.0	
C-BS-950	88	8.33	10-0475	$\text{SiO}_2 - \text{TiO}_2$	SiO_2	Infrasil	57.7	-0.495
WBBAR2	10	0.69	10-0471	$\text{SiO}_2 - \text{ZrO}_2$	MgF_2		5.0	
C-W1-f	16	0.69	10-0261	$\text{MgF}_2 - \text{Ta}_2\text{O}_5$	MgF_2	Infrasil	4.6	-0.345
C-W1-b	16	0.69	10-0263	$\text{MgF}_2 - \text{Ta}_2\text{O}_5$	MgF_2		4.6	
C-W2-b	16	0.69	10-0289	$\text{MgF}_2 - \text{Ta}_2\text{O}_5$	MgF_2	Suprasil	4.6	-0.091
C-W3-f	16	0.69	10-0261	$\text{MgF}_2 - \text{Ta}_2\text{O}_5$	MgF_2	Infrasil	4.6	-0.330
C-W3-b	16	0.69	10-0263	$\text{MgF}_2 - \text{Ta}_2\text{O}_5$	MgF_2		4.6	
WFC-BS1-b	16	0.76	10-0231	$\text{SiO}_2 - \text{HfO}_2$	MgF_2	Infrasil	5.0	—

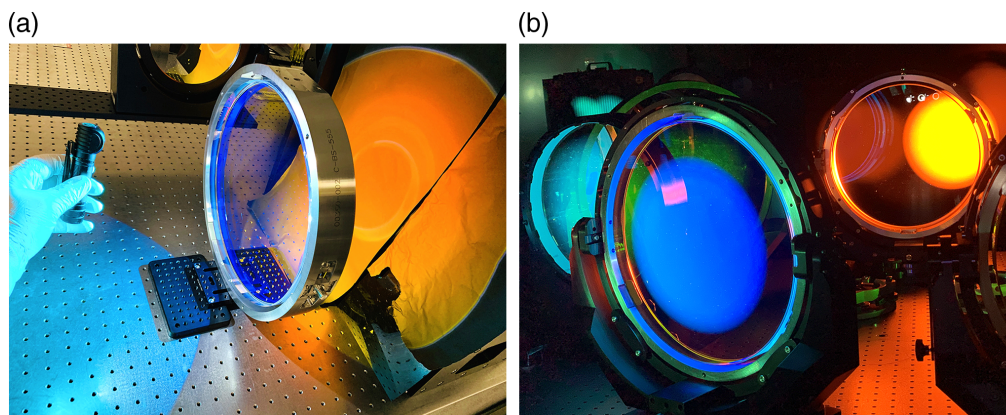


Fig. 3 (a) A lab inspection image of the BS-555 dichroic reflecting wavelengths below 545 nm while transmitting wavelengths beyond 570 nm. The optic is outside of the cell mount showing fixtures used for the 180 deg rotation at specific mounting stations. The incidence angle-dependent shift in transmission can be seen in (b) a darker orange color at the top of the transmitted aperture changing to yellow at the bottom of the transmitted aperture. The right-hand image shows an optical bench during on-sun observing using BS-555 along with other optics. DKIST was using the 2.8 arc minute field stop at Gregorian focus. The beam footprint for this optical station is visible as the blue circle seen on the surface of the optic.

Another challenge with these BSs is the requirement of rapid exchange and optical realignment. To compensate for beam displacement and dispersion, both the magnitude of the wedge and the orientation of the wedge must be accurately matched and mounted. For the DKIST FIDO dichroic suite, we specified the wedge of 0.5 deg (1800 arc seconds) to be the same magnitude for all optics to within 1 arc second physical angle. The ninth column of Table 1 lists the wedge magnitude measured by the manufacturer (Zygo) with a digital autocollimator. The mean wedge was 1799.66 arc seconds, only 0.341 arc seconds below the nominal target with a peak-to-valley spread of 0.77 arc seconds. The wedge clocking after the optic is bonded into a precision custom cell is below ± 0.3 deg. The wedge magnitude similarity of 0.77 arc seconds and wedge clocking constraint of ± 0.3 deg ensure that both the beam displacement and the dispersion are nearly identical with each optic.

These interchangeable optics see a range of beam footprints and apertures depending on the mounting station. The footprints for each field angle diverge from the pupil plane located on the DM. There is a slight divergence given the $F/6250$ theoretical (estimated $F/4600$ as built) focal ratio of the coudé laboratory beam. Table 2 lists the optical footprint and aperture for each optical station accounting for the elliptical shape at 15-deg incidence angle. The first column lists the mounting locations. Coudé lab stations for the FIDO dichroics are denoted CL x where x is the number of the station. To compensate for dispersion and translation from the wedge, all instruments see two of these wedged substrates in transmission. The second column shows the beam footprint at each optical station for any individual field angle with no substantial FoV (0'). We note this is effectively the same illumination as when using the DKIST pinhole target at Gregorian focus. The third column of Table 2 lists the illuminated aperture for the beam receiving the 2.83 arc minute circular solar FoV.

The DKIST FIDO BSs can be used at optical stations with footprints <240 mm and up to 290 mm with a varying degree of field separation. Figure 4 shows the smallest footprints on the WFC-BS1 up to the largest footprint at station CL4 just before entry into the DL-NIRSP instrument optics. We note that the beam has a 200-mm-diameter pupil on the DM just ahead of BS1. The 4-m entrance pupil (M1) was demagnified by 20 \times and the field divergence is increased by the same factor. The DKIST beam is very close to collimated ($F/6250$ design, estimated $F/4600$ as built) with the fields diverging away from the pupil located at the DM. Beam footprints from Fig. 4 can be correlated with the illumination pattern in Fig. 3(b) showing actual solar illumination in DKIST at station CL2 during August, 2021, on-sun testing. We note that the mild $F/6250$ nominal focal ratio ($F/4600$ as built focal ratio) causes roughly an ~ 1 mm increase in individual footprint diameters as the beam diverges away from the pupil. Footprints of the individual color circles in Fig. 4 increase from 202 mm on the DM to about 210 mm at CL4 station. This small increase in individual footprint diameter is negligible compared with the field divergence separating these individual footprints in Fig. 4.

2.4 FIDO Example Configuration

We outline in this section a single configuration for the FIDO optics that operates all the cameras within all the DKIST instruments simultaneously. We show the BSs and stations in Table 3. The WFS-BS1 sends a 4% Fresnel reflection from the uncoated fused silica front surface to the AO

Table 2 FIDO illumination and apertures.

Station	0' footprint	2.8' FoV aperture
DM	202 mm \times 209 mm	202 mm \times 210 mm
BS1	202 mm \times 209 mm	217 mm \times 225 mm
CL2	202 mm \times 209 mm	232 mm \times 241 mm
CL3	202 mm \times 210 mm	248 mm \times 257 mm
CL4	202 mm \times 211 mm	263 mm \times 273 mm

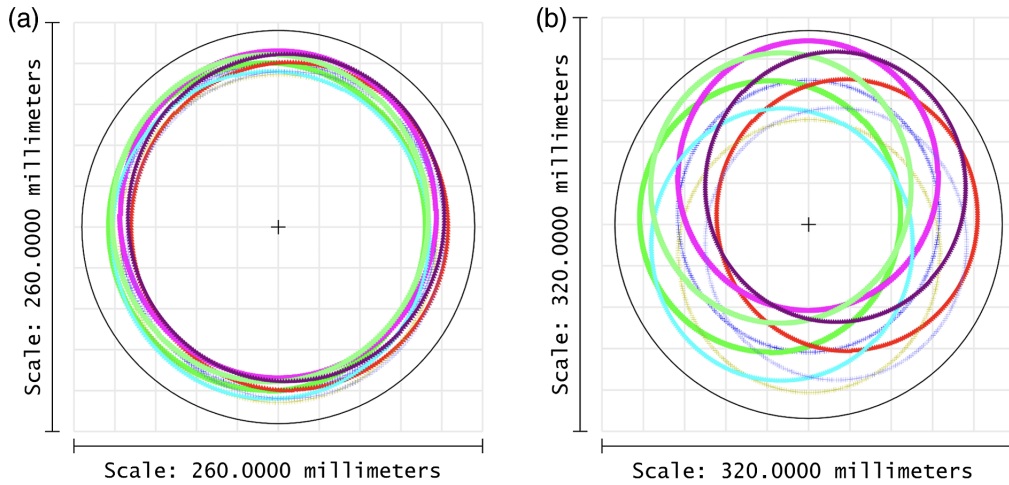


Fig. 4 Beam footprints on FIDO optics for the 2.8 arc minute field angle beam propagating past the AO system. (a) The WFC-BS1 footprint. (b) FIDO coatings can be illuminated over apertures of 241 mm at station CL2 up to 273 mm at station CL4. The footprints diverge away from the pupil (DM) toward the instruments at roughly 0.5 deg angle corresponding to the field divergence. The mild $F/6250$ nominal focal ratio ($F/4600$ as built) causes ~ 1 mm increase in individual footprint sizes at $202 \text{ mm} \times 210 \text{ mm}$.

Table 3 FIDO config.

Station	Optic
CL2	C-BS-555
CL3	C-BS-680
CL4	C-W3
CL2a	C-W2
CL3a	C-BS-643
M9b	M9b

system. This system operates the low-order wavefront sensor (LO-WFS), the high-order wavefront sensor (HO-WFS), and the context viewer camera. In station CL2, we mount dichroic C-BS-555 where we reflect wavelengths shorter than 555 nm toward ViSP and VBI-blue. In station CL3, we mount dichroic C-BS-680 to reflect wavelengths between 555 and 680 nm toward VTF and VBI-red. The final station CL4 has the window C-W3 with broad band antireflection coefficients on all surfaces for high transmission. With the planned upgrade to M9b, we can also add the CN SP and context imager (CI) to the camera list operating at long wavelengths.

In the station CL2a, we install the window C-W2 which sends the 4% Fresnel reflection from the uncoated front surface towards VBI-blue. This camera operates as a CI and science channel simultaneously with ViSP using reduced flux. ViSP can be configured to operate three cameras over a diverse range of spectral lines. In Table 4, we arbitrarily choose the three ViSP camera wavelengths to cover the Ca II H and K lines at 393 nm, the H_β line at 486 nm, and the photospheric Fe I line at 525 nm. In station CL3a, we install the dichroic C-BS-643 which would transmit 643 to 680 nm toward the VBI-red camera observing H_α at 656 nm. The reflected beam would allow VTF to observe in the 555- to 643-nm wavelength range. The VTF has one filter for the Fe I 630 nm line in this wavelength range.

In Table 4, we list the VTF as observing this 630 nm line. We note that VTF operates three separate cameras simultaneously. Two cameras are synchronized and operated as a dual-beam SP with simultaneous images at a single wavelength. The etalons scan the spectral line in steps of

Table 4 13 cameras.

Camera	λ (nm)
ViSP arm 1	393
ViSP arm 2	486
ViSP arm 3	525
VTF 1	630
VTF 2	630
VTF 3	630
DL-NIRSP VIS	854
DL-NIRSP NIR1	1083
DL-NIRSP NIR2	1565
VBI blue	393
VBI red	656
CN SP	4600
CN CI	4600
LO-WFS	539
HO-WFS	539
WFS CV	532

a few picometers. These two cameras can be compared with the spectrograph instrument calibrations as these cameras scan in wavelength to sample the spectral line. The third camera is set to observe continuum wavelengths adjacent to the spectral line and also is synchronized with the two polarimetric cameras. These three cameras all operate at wavelengths very close to 630 nm and are treated as one wavelength range, similar to spectrograph calibrations for our purposes here.

A highly transparent FIDO window C-W3 is installed in station CL4. The DL-NIRSP would thus receive all wavelengths from 680 nm to the cutoff of the Infrasil transmission near 3000 nm wavelength. We configure DL-NIRSP in Table 4 for observation at 854 nm using the visible wavelength camera. We set the two near-infrared cameras to the 1083 and 1565 nm lines. For reference, we list the wavelengths for the three AO system cameras all clustered around green wavelengths (G-band). Both the HO-WFS and the LO-WFS have a 21-nm FWHM band pass filter (Chroma ET-539-21x). The context viewer has a 10-nm FWHM filter.

2.5 FIDO Substrate Retardance in Transmission

We detail the material and polarization properties of the substrates in Table 5. The stress optic coefficient (SOC) is listed in the second column. It was measured at 633 nm wavelength for Heraeus Infrasil to be 3.61 nm per cm per bar. A slightly lower value of 3.54 nm per cm per bar is listed for the synthetic Suprasil family at the same wavelength. There is typically some mild wavelength dependence of the SOC that we show impacting our sample measurements in later sections. We derive the sensitivity to stress for the FIDO 43-mm thick substrates in the third column of Table 5. We derive roughly 15 nm of phase retardance per bar of stress (155 nm/MPa). The fourth column of Table 5 translates this to roughly 9-deg retardance. As the FIDO optics operate in two different orientations with respect to gravity, the intrinsic stresses from 1 g loading will produce some very small differences in optic performance.

Table 5 FIDO substrate birefringence and retardance.

Optic material	SOC ($\frac{\text{nm}}{\text{cm}\cdot\text{bar}}$)	Stress sensitivity (nm/bar)	Stress sens. (deg/bar)	Refract. index homogen.	Intrinsic stress (nm/cm)	Intrinsic birefring. 43 mm	Retardance degrees at 633 nm
Infrasil 302	3.61	15.5	8.8	610^{-6}	5	21.5 nm	12 deg
Suprasil 3002	3.54	15.2	8.6	310^{-6}	5	21.5 nm	12 deg

The FIDO optic stress was estimated using finite element models to be below 0.1 MPa (1 bar) peak to peak across the entire optic. The peak stresses are concentrated outside the clear aperture and are concentrated near the three mounting fixtures attached to the edge of the substrate. We can expect possibly a few nm of transmitted phase retardance varying with gravity in the DKIST FIDO substrates from these mounting stresses.

The refractive index homogeneity is listed as the fourth column of Table 5 with the Suprasil being twice as uniform on all three spatial axes. We note that the manufacturer performed magneto-rheological finishing (MRF) on small subapertures to control transmitted wavefront by polishing out low-order refractive index spatial variation. We detail in later sections some strong differences in transmitted wavefront due to index inhomogeneities. We required the FIDO glass grades 302/3002 where refractive, striae, and intrinsic stress birefringence are controlled in all three spatial directions. However, the MRF subaperture correction was still required to meet our stringent transmitted wavefront requirements. The intrinsic residual strain birefringence within the Heraeus glasses was specified at <5 nm/cm as shown in the fifth column of Table 5. This translates to a possible 21.5 nm of intrinsic retardance attributable to the 4.3-cm thick substrates in the sixth column and 12 deg retardance shown in the seventh column. The combination of stress birefringence and intrinsic birefringence will be anticipated and calibrated using the field angle-dependent demodulation matrix. Some mild depolarization is also anticipated from the spatial average over the nonuniformities inside any individual beam footprint.

2.6 FIDO Dichroic Transmitted Wavefront

The transmitted wavefront error (TWE) for these BSs represents a combination of the substrate properties and the coatings. Most of the substrates had precoat TWEs with only a few nm RMS error well described using only the low-order Zernike modes. We do note that a few substrates ended up with more complex spatial behavior due to refractive index inhomogeneities at higher order. As examples, Fig. 5 shows the TWE with power removed through select optics. The BS-465 in Fig. 5(a) and BS-950 in Fig. 5(c) are typical of most other FIDO dichroics. Figure 5(b) for BS-680 shows concentric radial features with a relatively small size but larger amplitude spike near the center of the aperture. This BS-680 TWE was somewhat mitigated by the subaperture MRF polishing procedures. The relatively large size of the tooling compared

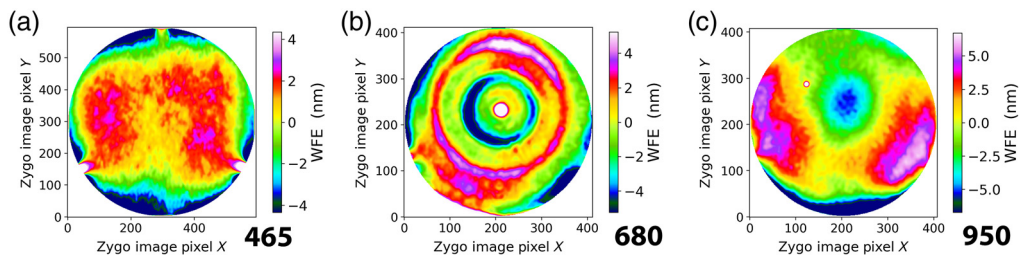


Fig. 5 The TWE with power removed through select FIDO dichroics over the full 290 mm aperture. (a) BS-465: a ± 4.2 nm color scale. (b) BS-680: a ± 5 nm color scale. The high spatial frequency features are present in the uncoated glass substrate and are attributed to less homogeneous glass refractive index. The small spatial scale features were not mitigated with the subaperture MRF process applied to all our dichroics. (c) BS-950: a ± 7 nm color scale.

with the small size of the TWE feature in this synthetic Suprasil 3002 substrate prevented removal of these higher order terms.

Figure 6(b) shows the RMS variation of the TWE after the power term is removed. This irregularity does not seem to have any obvious correlation with coating thickness. All windows and BSs were below 5-nm RMS irregularity after the power term is removed. Trends in the power term of TWE with increasing coating thickness are less obvious. Figure 6(a) shows the power term of TWE through the substrate. The green and blue dots show the two different orientations relative to gravity. We also note that we did a single repeat measurement of the BS-680 part in transmission after roughly 3 weeks and found substantial relaxation of the TWE power term as well.

2.7 FIDO Dichroic Reflected Wavefront

The FIDO dichroic BSs have reflected wavefront errors that contribute to postadaptive optics noncommon path WFE at levels of typically <10-nm peak to valley (PV) after the power term is removed. The 5.25-nm RMS specification was passed for the front surface (S1) figure in reflection for the dichroics in most circumstances. Figure 7 shows example reflected wavefront maps with power removed for the BS-465, BS-643, and BS-950. In most of the dichroics, a smooth low-order behavior is seen across the aperture. For the BS-643, we note that the overall reflected

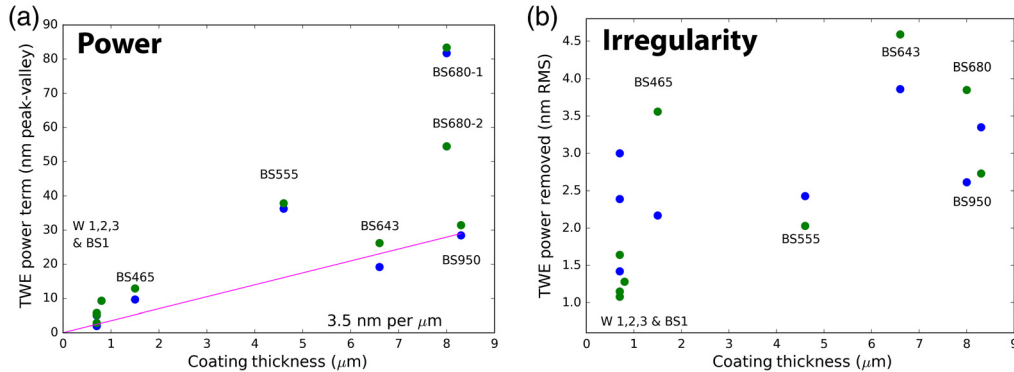


Fig. 6 (a) The power term of the TWE. Blue and green dots show different orientations with respect to gravity. The trend line shows a manually generated 3.5 nm of power per micron of coating thickness. We note that the BS-555 and initial tests of BS-680 are well above this line. Temporal change in coating stress discussed below was identified and also contributes to the variance against this arbitrary trend line. (b) The RMS variation of TWE in nm after the power term is removed. This power-removed irregularity was mostly low order variation but without much correlation with coating thickness.

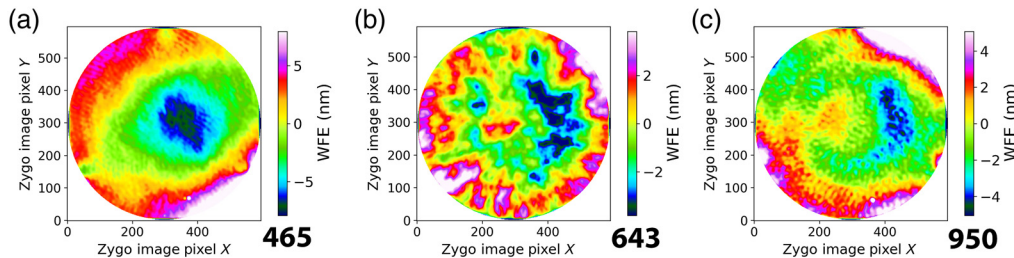


Fig. 7 The front reflecting surface (S1) figure error in nanometers after removal of the power term over the full 290-mm diameter aperture at 633 nm wavelength. We choose a few representative dichroics showing a variety of behavior. (a) BS-465: a scale of ± 7 nm with large, slightly decentered feature dominating the spatial behavior. (b) BS-643: a smaller ± 3.5 nm scale where more spatial structure at smaller scales is visible. (c) BS-950: a ± 5 nm scale with the outer edges having the most significant deviation in surface shape.

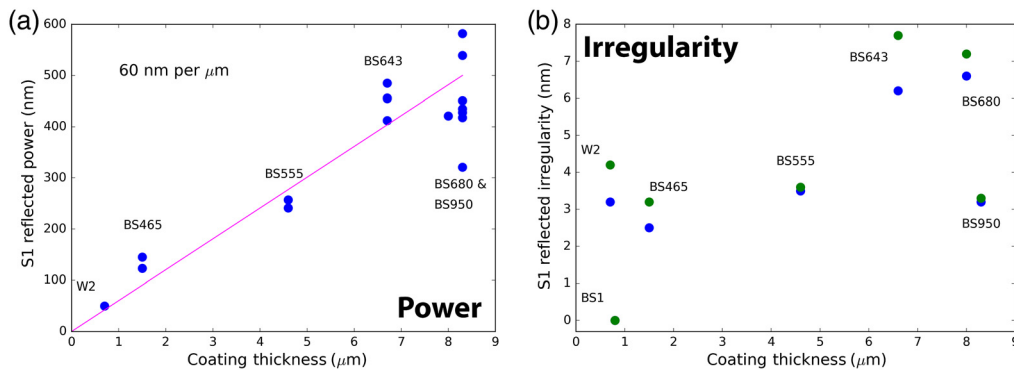


Fig. 8 (a) The power term in the front surface figure impacting the reflected beam. We overlay a linear trend line at 60 nm of surface figure power per micron of coating physical thickness to guide the eye. We note that the multiple repeated tests of BS-680 and BS-950 showed a substantial relaxation of this stress over a time scale of weeks post coating. (b) The RMS surface figure variation (irregularity) with tip/tilt and power removed. Blue and green show the variation with gravity in the actual mount as the optic is rotated from 0 deg to 180 deg against gravity. There does not seem to be a correlation with coating thickness.

wavefront is lower magnitude but has more detectable features at smaller spatial scales (higher orders).

The coating stress introducing power follows a trend of roughly 60-nm PV power per micron of coating thickness. Figure 8(a) shows the first surface reflection power term for both orientations of each dichroic as well as C-W2 uncoated front surface (unbiased). We show additional points for the thicker dichroic coatings as we monitored the reflected wavefront of these dichroics over some months. Figure 8(b) shows the RMS surface figure error in reflection after removal of the power term. There does not seem to be obvious trends in this power-removed RMS error with coating thickness. We also note that the green and blue points represent the two different optic orientations against gravity showing there is some small differences between the two intended FIDO mounting configurations.

There was significant temporal evolution of the power term in the reflected surface of the optic due to a change in the stress of the coating. The processing of these dichroics did not include any postcoating heating steps. These simple (cost effective) evaporative coatings are porous. In the fabrication of the first few dichroics, we did not account for a temporal term when setting the bias power ground into the substrate. For subsequent dichroics (950, 680, and 643) we biased the reflective first surface 100-nm PV power below the fresh coating power target to account for the coating stress relief in the first 2 months postcoating. Figure 9(a) shows the temporal evolution of power [Zernike term two (Z_2), defocus] from the dichroic first surface reflection. The dashed lines show the stress test optics as ST. We note that the first attempt at BS-950 was the first stress test for a full sized optic. Given the measured temporal behavior, we proceeded to test full sized optics for all other coatings. We also note that we added 100 nm to the BS-465 measurement to put the power from this relatively thin coating on the same vertical scale as the other dichroics. Figure 9(b) shows the residual power in the as-built dichroics on the last reflected WFE measurement. This represents the power term in the reflected beam as the optics were accepted including the bias power term ground into the substrate.

We evaluated our thickest coating on a full sized stress test optic for more than a year (ST-950). In Fig. 10, we show the long-term temporal evolution of coating stress as measured by the vendor in reflected surface figure power over the full 290 mm aperture. We saw a similar reduction of coating stress over longer terms. At the recommendation of the coating vendor, we decided to bake the optic given concerns about humidity and/or slow coating oxidization. There is substantial temporal evolution anticipated by DKIST for these coatings for the reflected power term. We note that the VTF and two VBI channels can accommodate substantial power with focusing optical elements. The ViSP currently implements a manual refocusing procedure. For now, the residual power in reflection is within the depth of focus of the ViSP allowing for efficient reconfiguration of the DKIST optics. Automated refocusing of the ViSP can be implemented if required given the possible change of coating stress over time.

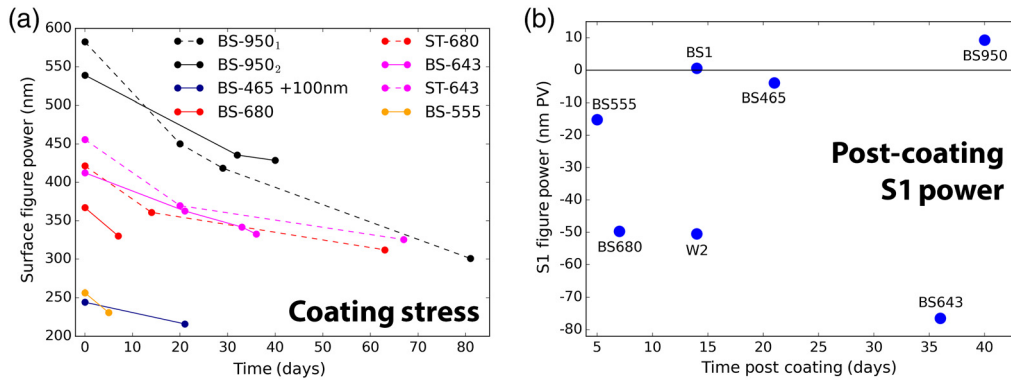


Fig. 9 (a) Temporal evolution of the coating power with time after coating. We denote the stress test full sized coated optics with ST-. The actual as-built BSs are denoted BS-. We note that BS-950 was stripped and recoated with the initial optic denoted BS-950₁ and the second coating delivered to the summit denoted as BS-950₂, in addition to having a full sized stress test optic (ST-950). All of the dichroic coatings relaxed over time. (b) The power in nanometers PV left after the last metrology data was collected representing the most relaxed coating stress value we measured.

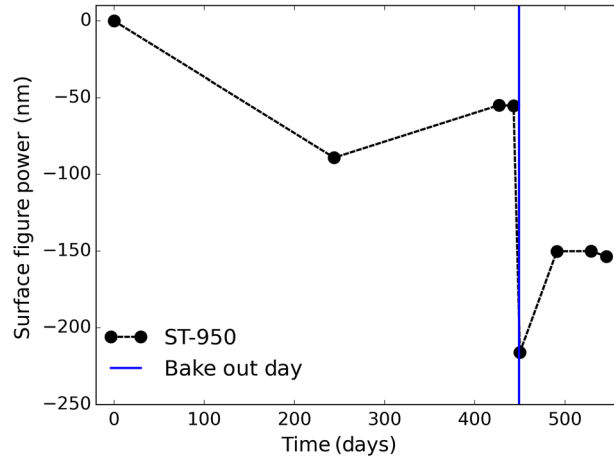


Fig. 10 The temporal evolution of the coating stress induced first surface (S1) power (PV surface figure) for the stress test dichroic (ST-950) with time after coating over roughly 1.5 years. This dichroic was baked on day 448 shown as the vertical blue line to assess stress relief and temporal evolution with measurements on days 443 and 450 bracketing the event. The coating stress did cause a reduction in the PV surface figure power by ~ 100 nm over several months. This was stable to 30 nm over another few months. After baking, the coating changed rapidly over a few weeks but again settled to a new lower value.

2.8 FIDO Dichroic Beam Splitter C-BS-950

The C-BS-950 optic was the most challenging with a coating near $8.3 \mu\text{m}$ thickness. We detail this coating here as an example of the most challenging case. All FIDO coatings were thoroughly characterized and summarized in [Appendix C](#). We performed most of the coating uniformity testing and model verification using the dichroic 950 formula with more than 13 test coating runs detailed in [Appendix 7.5](#). We show in this section examples of the final performance including narrow spectral features in intensity and polarization. The uniformity testing in reflection and transmission is done at the vendor Infinite Optics Inc. (IOI) over the full 290-mm aperture. High spatial and spectral resolution Mueller matrix mapping on 100 mm diameter apertures in transmission is done with our custom system including investigations of stress birefringence and intrinsic substrate birefringence. We compare with an outside ellipsometric vendor mapping the

Mueller matrix in reflection on a 100-mm diameter aperture. We summarize with calculations of depolarization caused by the spatial variation estimated for this type of coating.

2.8.1 BS-950: final coating reflection and transmission spectral features

The final BS-950 coating run 10-0475 transitions from more than 95% reflective at 960 nm wavelength to better than 95% transmissive at 1000 nm wavelength. Figure 11 shows transmission and reflection measured on several different samples at the vendor (IOI). We compare this metrology with our Boulder-based custom National Solar Observatory Lab Spectro-Polarimeter (NLSP) previously used in our works on DKIST polarimetry.^{81,81,84–88} Figure 11(c) shows our NLSP measurements on witness samples at 0 deg and 15 deg incidences. With the visible system spectral resolving power of roughly 1.4-nm FWHM, we can easily resolve narrow transmission spectral features.

2.8.2 BS-950: narrow spectral features reflection

The BS-950 dichroic coating has several narrow spectral bandpasses where the transmission can drop by more than 10%, the diattenuation can reach more than 20% and the retardance can change by more than 250 deg over 1 nm wavelength. These kinds of narrow features (spikes) are very common in dichroic coatings but are only seen if the metrology equipment has spectral resolving power far better than 1 nm.

There are a few spectral features at large magnitudes with more of them concentrated at shorter wavelengths. This BS-950 optic was designed to be used behind other dichroics so optimization emphasis was put on longer wavelengths in the reflection band. Figure 12 shows the polarization and intensity measured with our NLSP setup in the Boulder labs in early 2021. Two bare aluminum-coated mirrors were used at roughly 50-deg incidence, while the BS-950 witness sample was mounted at 15 deg. The reflectivity is shown in Fig. 12(a), diattenuation in Fig. 12(b), and retardance in Fig. 12(c).

Figure 13 shows the same data set on the final BS-950 dichroic coating from run 10-0475 with reflectivity shown in Fig. 13(a), diattenuation in Fig. 13(b), and retardance in Fig. 13(c). For this figure, we highlight a 7-nm spectral window from 588 to 595 nm near a common solar astronomy spectral line pair for the sodium doublet 588.0 and 589.5 nm. Had this feature been spectrally shifted by 1 nm, a 7% drop in throughput, 10% diattenuation, and 270 deg per nm retardance spectral gradient would be present in DKIST observations, necessitating more stringent calibration and stability requirements.

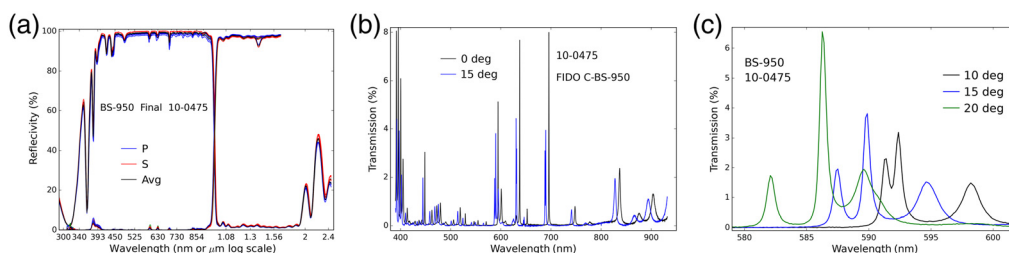


Fig. 11 Reflectivity and transmission for the final delivered C-BS-950. The nominal design reflects 380 to 920 nm and transmits 1000 to 1800 nm. (a) The IOI measured reflectivity and transmission covering a wide wavelength range for both *S*- and *P*-linear polarization states. We note the strong absorption at wavelengths shorter than 380 nm. Narrow spectral features are present in our data recorded with NLSP. (b) Our NLSP measurements of transmission at 0 deg in black and 15 deg incidence in blue for the bandpass where the coating is designed for high reflection. (c) Our NLSP measurements in a narrow spectral region around the 590 nm bandpass showing how ± 5 deg incidence angle change changes these narrow spectral features. Black, blue, and green represent 10 deg, the nominal 15 deg, and 20 deg, respectively. There are three narrow spectral features that both shift toward the blue and themselves separate as the incidence angle increases.

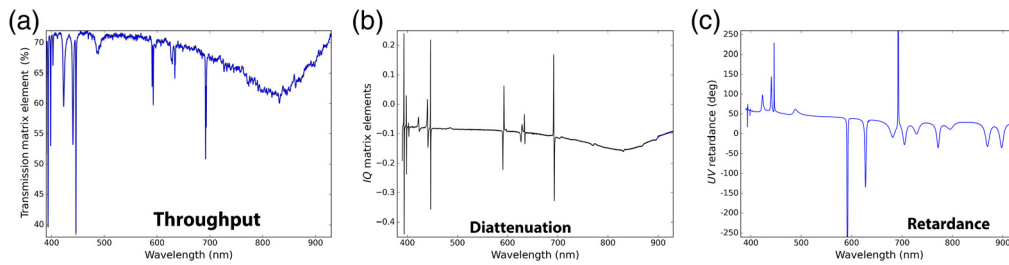


Fig. 12 (a) The intensity, (b) diattenuation, and (c) retardance in reflection for the final delivered C-BS-950 coating. Our NLSP system measured coating witness sample at 15 deg incidence angle from run 10-0475 in a K-cell type test setup. Note the smooth spectral variation includes two bare aluminum-coated samples near 55 deg incidence showing the 850-nm reflectivity drop and associated diattenuation.

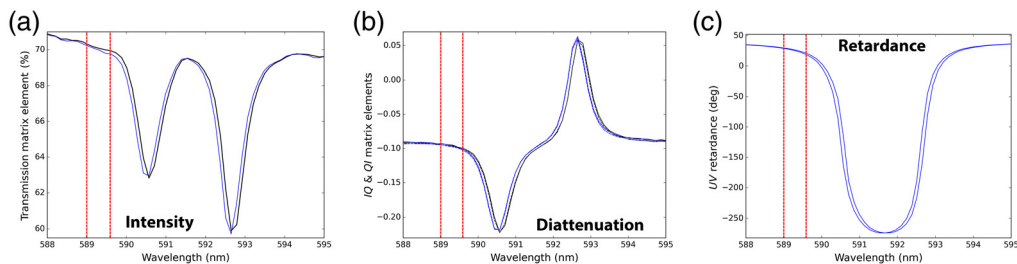


Fig. 13 The NLSP K-cell measurements for the final delivered C-BS-950 coating witness sample at 15 deg incidence in reflection from run 10-0475 in a K-cell type test setup. We highlight a narrow 7 nm bandpass from 588 to 595 nm near the sodium doublet spectral line. (a) The total throughput of the K-cell as the II Mueller matrix element. Black and blue colors show two repeated measurements. (b) The diattenuation. There are four curves plotted. Solid and dashed lines correspond respectively to the IQ and QI elements of the Mueller matrix. Blue and black colors show two repeated measurements taken sequentially. (c) Retardance in the UV and VV elements of the Mueller matrix. The two lines represent the two repeated sequential measurements. The vertical dashed red lines denote the sodium doublet at 589.0 and 589.6 nm.

2.8.3 BS-950: 290mm aperture spatial variation for reflection and transmission

The coating uniformity strongly depends on the wavelength. The narrow spectral features as well as wavelengths near the transition from reflective to transmissive see greatly increased spatial variations. Mapping of the IOI coating chamber was done with nine samples in a cross pattern. One sample was at the aperture center. Four samples were at a radius of 75 mm separated by 90 deg clocking covering an aperture diameter of 150 mm. Four more samples were at a 145-mm radius also each separated by 90 deg covering the full 290-mm-diameter FIDO BS aperture. Figure 14 shows reflection and transmission spectra from all data sets provided by IOI during metrology in Fig. 14(a). Figure 14(b) shows the difference of the nine individual samples from the center measurement. The coating absorption features as well as the transition wavelength are far more variable.

2.8.4 BS-950: transmission spatial variation in 100 mm aperture with NDSP3

These FIDO dichroic coatings have measurable spatial variation in transmission over relatively smaller apertures. As examples, we had included 4-in.-diameter fused silica substrates in preliminary coating stress testing from the part SN12, run 10-0195. See Appendix 7.5 for additional details on testing the spatial and spectral variation of the BS-950 dichroic coatings. We upgraded our Maui laboratory SP at the DKIST Science and Support Center to a three spectrograph setup we call NDSP3. We measured spatial maps of transmission variation for the BS-950 coating in

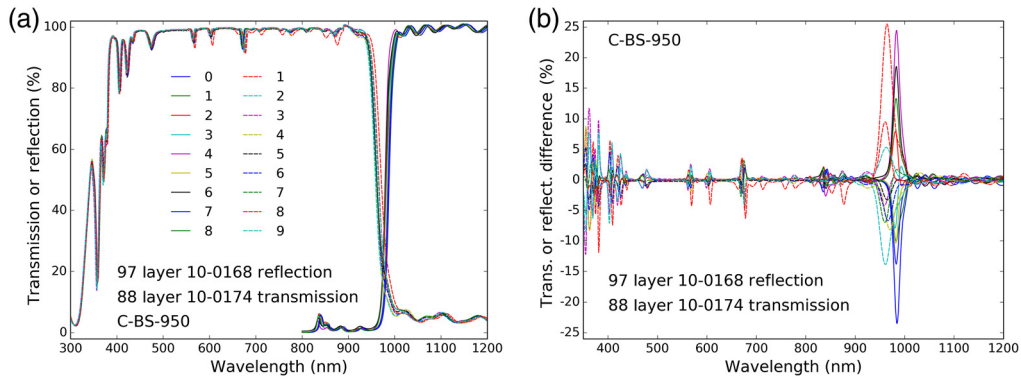


Fig. 14 (a) Reflectivity and transmission differences from a uniformity data set with nine samples covering the full 290-mm diameter aperture. We show uniformity on a preliminary 97 layer test coating 10-0168 initially measured in reflection shown as dashed lines. We subsequently changed the design slightly to an 88-layer coating. The 88 layer uniformity in transmission is shown as solid lines. (b) The difference of the eight outer samples from the central sample for both the 97-layer and 88-layer coating runs. Uniformity differences are largest in the narrow spectral features as well as at the 950-nm transition wavelength. Given the 2-nm spectral resolving power of this data, the magnitude of the narrow spectral features is greatly reduced, but the features themselves are obvious.

April, 2021. We used a rosette spatial sampling with a 2-mm-diameter collimated beam and 1.5-mm spatial steps covering a 103-mm-diameter aperture (see Fig. 42 of Ref. 84, 6, for example, rosette sampling). Figure 15 shows an example spatial map at 1075.5 nm wavelength.

2.8.5 BS-950: Mueller matrix transmission spatial variation, NLSP, 84 mm aperture

Coating polarization properties are expected to vary spatially with inhomogeneous coating layers both in reflection and transmission. We also expect substantial contributions to the transmission

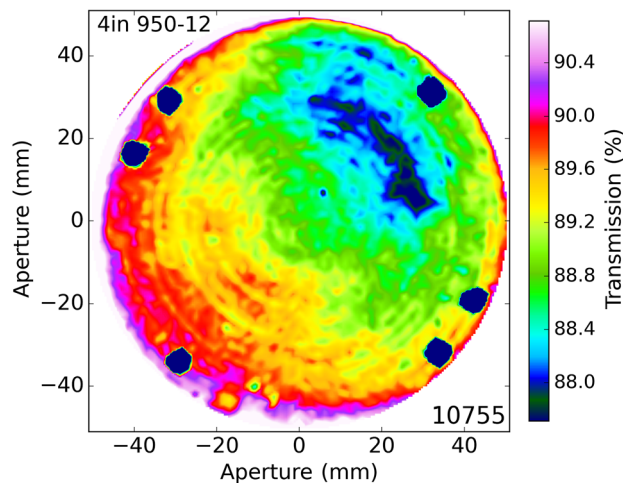


Fig. 15 The spatial variation of transmission over a 103-mm-diameter aperture measured with NDSP3. The BS-950 dichroic formula coating was deposited in run number 10-0195 on a coating stress sample serial number SN-12 during preliminary testing. We show the spatial transmission map at a wavelength of 1075.5 nm. There are a series of square and circular uncoated rough areas on the outer edge of the aperture used to coalign the interferometric wavefront measurements that show up as nearly zero transmission. The color scale has been set as the median of the transmission over the aperture with a scale of $\pm 1.5\%$. Note that the general form of the spatial variation is a strong function of wavelength.

polarization properties from both the intrinsic birefringence of the glass substrates as well as through stress birefringence. We show here transmission Mueller matrix measurements.

The synthetic fused silica glass substrates used in our coating stress testing were provided by Nikon with 21 mm thickness. The intrinsic birefringence was specified at <5 -nm retardance per cm of path, which is the same specification as the Heraeus Infrasil 302 and Suprasil 3002 used in the FIDO optics (35 mm BS1, 43 mm dichroics and windows). We similarly expect the mounting stresses from the V-block-type filter holder used in our NLSP measurements to introduce substantial stress birefringence in the vertical direction. With the SOC of fused silica near 3.5 nm per cm per bar and a thickness of 21 mm, we anticipate several degrees retardance.

Retardance was derived from Mueller matrix measurements taken in April, 2021, with our Boulder-based NLSP system on a 4-in.-diameter stress test sample. We show an example retardance spatial map at 9737 \AA wavelength covering an 84-mm aperture in Fig. 16(a). Figure 16(b) covers $15,651 \text{ \AA}$ wavelength in the same data set. In Fig. 16(c), we show the retardance spectra derived at all 169 spatial locations. We also show the standard deviation of the retardance across the aperture at every wavelength multiplied by $10\times$ for a convenient reference. The top row of Fig. 16 shows maps where the V block clamp was screwed down tightly. The bottom row used a setup with greatly reduced clamping forces, barely enough to secure the optic in the translation stages. The spatial form of the retardance changes substantially. The magnitude also drops by a few to several degrees net retardance attributable to glass birefringence. The spatial variation for the higher stress graphics in the top row is relatively constant at a 10σ value near 5 deg (or 1σ value near 0.5 deg). The spatial variation remains relatively constant, even though the coating retardance drops from a peak near 34 deg down to 5 deg in the high stress setting. The red spectra also show the total overall retardance drops substantially between high stress and low stress measurements. For instance, the peak is 34 deg retardance when stressed but only 27 deg when mounted with low stress. We also note that there is substantial variation at wavelengths in and around the transition from reflective to transmissive, in the 900 to 1000 nm range.

A coating-based variation of over 1.4 deg retardance measured over this aperture would linearly scale to 5 deg retardance over a 290-mm FIDO optic aperture. Scaling could easily

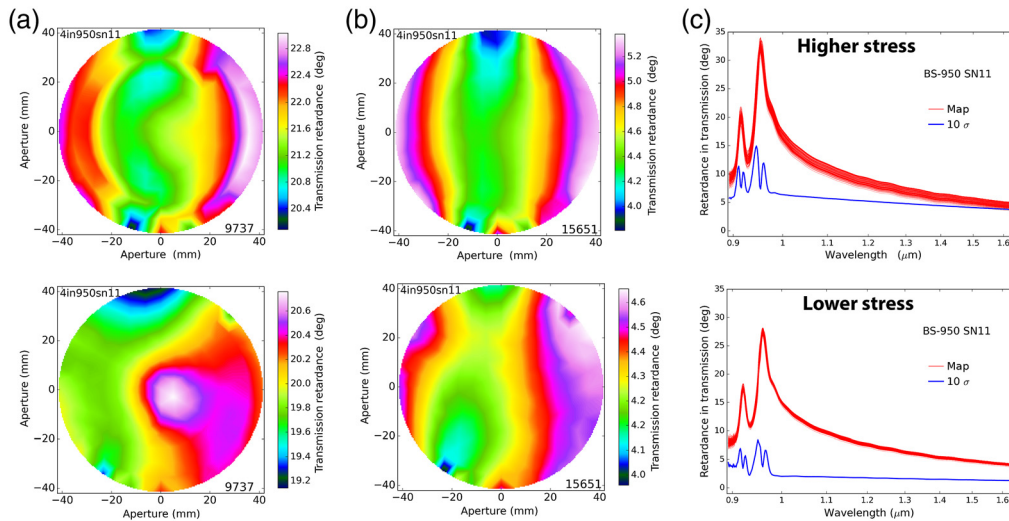


Fig. 16 (a), (b) A spatial map of linear retardance in transmission derived from the U to V elements of the Mueller matrix across an 84-mm aperture of a 4-in.-diameter BS-950 stress sample SN11 at 15-deg incidence angle recorded in April, 2021. The wavelength in Angstroms is noted in each graphic with (a) 9737 \AA and (b) $15,651 \text{ \AA}$. (c) Linear retardance spectra at all 169 individual spatial points as thin red curves. The thick blue curve shows the $10\times$ the standard deviation of retardance across the aperture. The top row shows a higher stress tight clamp mounting. The bottom row shows a low stress mounting to reduce substrate stress birefringence. (c) The spatial variation of retardance as the blue curve is a relatively constant 10σ around 5 deg at most wavelengths, even though the net retardance of the combined coating and substrate falls from 34 deg at 950 nm to 6 deg at 1600 nm wavelength. The higher stress mounting shows spatial variation a factor of more than 2 higher.

be of higher power (e.g., quadratic) leading to relatively larger terms in the DKIST FIDO optics. This would need to be separated from the intrinsic birefringence and stress birefringence in the substrate. Two main impacts are apparent. First, we expect depolarization from the average over the aperture to reduce the magnitude of detected Stokes vectors. Second, we expect some mild field dependence to be introduced to the modulation matrix as the beam footprints for all fields do not coincide (dichroics are not pupil conjugate). Given the relative lack of detectable coating spatial variation in the design transmission bandpass, the substrate is likely a substantially larger contribution to the overall depolarization.

Figures 17(a) and 17(b) show example spatial maps of the diattenuation. Figure 17(c) shows the diattenuation spectra in red along with the 5σ spatial variation in blue. The spatial variation of diattenuation was not substantially detectable with our nominal single map systematic error limit roughly at 0.05% amplitudes for this data set. We show a data set with reduced clamping forces and also a 45-deg rotation with respect to Fig. 16. The rotation decouples intrinsic substrate stress (rotating with the substrate) and stress birefringence from clamping forces (fixed in the instrument). We note that the diattenuation in transmission is below $\pm 0.2\%$ for this coating for wavelengths longer than 990 nm.

Figure 18 shows the circular retardance in transmission over the same 84 mm aperture. Figures 18(a) and 18(b) show spatial maps. These spatial maps follow the stress birefringence spatial patterns seen in the linear retardance. Figure 18(c) shows the circular retardance spectra in red and the 5σ variation across the aperture in blue. The circular retardance is barely detectable outside the coating transition wavelengths. See Appendix 7.5 for more details.

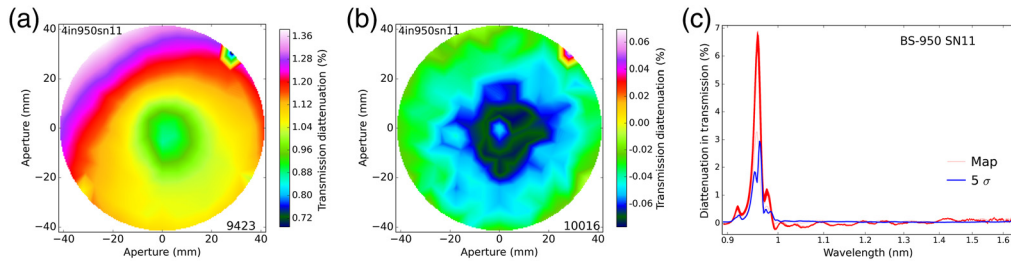


Fig. 17 (a), (b) A spatial map of diattenuation in transmission derived from the Mueller matrix across an 84-mm aperture of a 4-in.-diameter BS-950 stress sample SN11 at 15 deg incidence angle recorded in April, 2021. The wavelength in Angstroms is noted in each graphic with (a) 9423 Å and (b) 10,016 Å. (c) Diattenuation spectra at all 169 individual spatial points as thin red curves. The thick blue curve shows the $5\times$ the standard deviation of diattenuation across the aperture. The spatial variation of diattenuation is near the NLSP systematic error limits for detection.

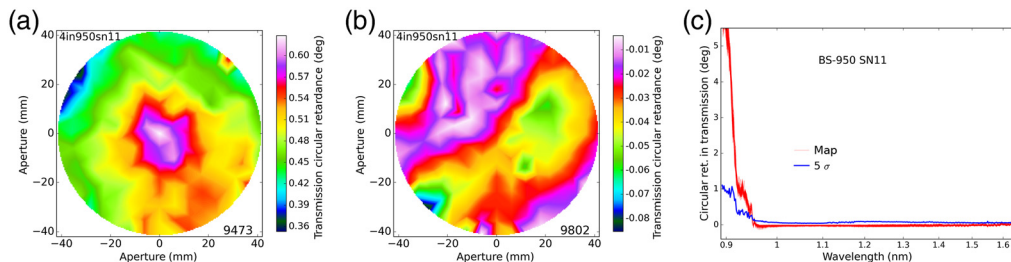


Fig. 18 (a), (b) A spatial map of circular retardance in transmission derived the Mueller matrix across an 84-mm aperture of a 4-in.-diameter BS-950 stress sample SN11 at 15-deg incidence angle recorded in April, 2021. The wavelength in Angstroms is noted in each graphic with (a) 9473 Å and (b) 9802 Å. (c) Circular retardance in transmission spectra at all 169 individual spatial points as thin red curves. The thick blue curve shows the $5\times$ the standard deviation of circular retardance across the aperture. The spatial variation of circular retardance follows the stress birefringence pattern.

2.8.6 BS-950: Reflected Mueller matrix spatial map, RC2 ellipsometer, 100 mm

We funded an outside vendor, J.A. Woollam, to collect reflected Mueller matrix spatial maps of our 4-in.-diameter coating stress test samples. We use this to demonstrate spatial variation in reflection as well as for comparison between a typical 2 nm spectral resolving power instrument and our <0.3 nm instruments. A spatial map was done in a spiral pattern using 95 spatial samples on one of our BS-950 stress test samples serial number (SN-04). Woollam used their RC2 ellipsometric system and translation stages to cover a 100-mm diameter aperture. We note that the Woollam RC2 system used has a spectral resolving power of roughly 2-nm FWHM. These narrow spectral features resolved by our 0.3-nm FWHM system show larger magnitudes and correspondingly more spatial variation concentrated at the particular wavelengths where coating properties change spectrally. These measurements agree well with our two NSO-built systems as well as the metrology provided during testing and acceptance by the coating vendor (Infinite Optics).

We highlight the strong spectral dependence of the spatial variation by subtracting the aperture average from the 95 individual measurements. Figure 19 shows several very narrow spectral features (spikes) with some features in retardance being barely visible in intensity and vice versa. The reflectance can vary by up to $\pm 20\%$ in the short wavelength absorption features. This dichroic was optimized to be used with other BSs (e.g., BS-465, 555) so the performance at wavelengths short of 465 nm is not optimal. There are retardance features in reflection near 600 and 700 nm wavelength that vary by over ± 130 deg. The spatial variation of reflectance is over $\pm 10\%$ at short wavelengths.

The spatial maps of the intensity and polarization parameters have both large spatial variation and similarly strong wavelength dependence. Figure 20 shows the spatial maps at select wavelengths for particular polarization parameters derived from the Mueller matrix measurements. Wavelengths were chosen to highlight some of the worst spatial variation. The spatial form Mueller matrix element variation can have circular symmetry as well as gradients across the aperture.

For instance, at the 589-nm science wavelength corresponding to the sodium doublet line common in solar observing, the unpolarized reflectivity has $<4\%$ variation, diattenuation is effectively noise limited below $\pm 0.1\%$ diattenuation, and retardance varies by <1.2 deg peak-to-peak. However, in Fig. 20(a), the retardance uniformity in the top right-hand graphic is more than 65 deg across the aperture after only a shift of 13-nm wavelength to 576 nm. Similarly, the diattenuation in the top middle graphic varies by about 5% peak to peak, 50 times larger than at 589 nm. The reflectance uniformity in the top right-hand graphics has similar spatial morphology but is actually about twice as uniform at 576 nm compared with 589 nm.

2.9 Depolarization from Spatial Variation: Footprint Averaged Mueller Matrices

There are two separate impacts to consider when using an optic having spatially variable Mueller matrix elements. First, the average over the individual footprints at any particular field angle will

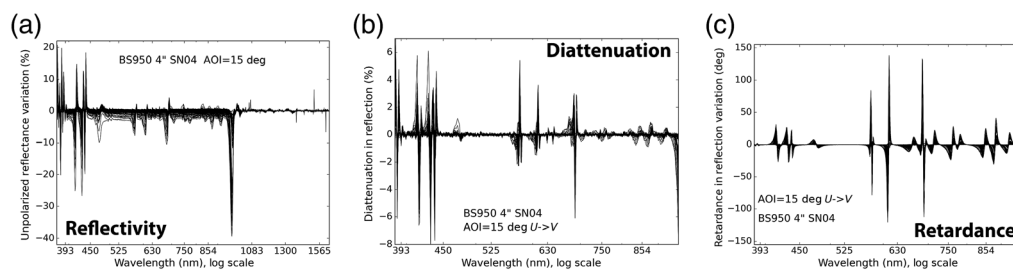


Fig. 19 The spatial variation of measured Mueller matrix elements for the BS-940 stress test sample SN04 at 4 in. diameter. (a) The unpolarized reflectance spatial variation over the full metrology wavelength range covering both reflection and transmission bandpasses. (b) The I to Q diattenuation while (c) the U to V retardance highlighting the reflection bandpass 380 to 950 nm.

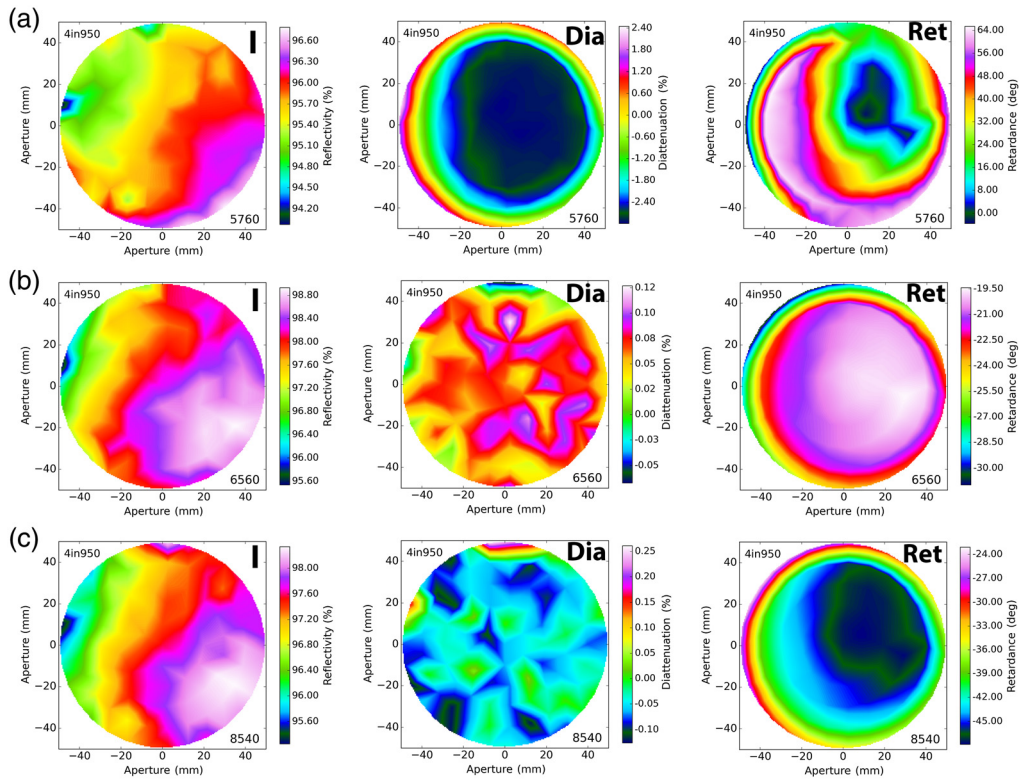


Fig. 20 The spatial maps of select polarization properties derived from the 95 point reflective Mueller matrix maps on the BS-950 dichroic coating stress test sample measured at 15 deg incidence. Maps cover a 100-mm-diameter aperture on a 114-mm substrate or 88% aperture. (a) One of the worst offending wavelengths at 576 nm. (b) The 656-nm science wavelength (H_{α}). (c) The 854-nm science wavelength (Ca II NIR). The left column shows reflectivity maps for unpolarized light (the I Mueller matrix element). Color scales range roughly 2% to 3% PV for all wavelengths. The middle column shows Q diattenuation. The 576-nm map ranges by over 5% with much variation outside a 75% aperture. The other two wavelengths are scaled by $<0.3\%$ peak-to-peak. The right column shows the U to V retardance in degrees. Variation outside a 75% aperture is also seen along with a substantial pattern in the aperture. There is over 60 deg retardance variation at 576 nm but <5 deg at 656 nm even after removing the coating behavior outside an 80% aperture.

create depolarization. This depolarization is easily calibrated provided the optical beam is stable, and the calibrator is well fit for all relevant errors. In practical terms, the DKIST beam wander and calibration optic uncertainties are far larger than any particular depolarization caused by the FIDO dichroics. The second major impact is in having a system Mueller matrix that depends on the field angle. This field dependence also is easily calibrated with a field-dependent demodulation matrix for the system. For DKIST, the individual field angle footprints shown in Sec. 2.3, Fig. 4 does not separate by more than 30% of their diameters at the FIDO optical station furthest from the pupil plane (DM, M10). DKIST software already has the capability to implement a field-dependent demodulation matrix, and some mild changes in these Mueller matrix elements is anticipated.

We create a simple model for the depolarization caused by a spatially variable Mueller matrix using the stress sample measurements presented in Sec. 2.8.5. We take the transmission map, Q diattenuation map, and elliptical retardance map and create a polarization preserving Mueller matrix at every spatial point across the optic aperture. We choose the data from 1057 nm wavelength. The transmission aperture variation was 1.71% RMS but with a 40.5% PV. The Q diattenuation spatial map has a mean value of -14.9% with 0.88% RMS variation but a PV of 17.3% dominated by a small spot of very high diattenuation from in Fig. 17.

The U to V retardance aperture map has a mean value of 11.1 deg with an RMS variation of 0.19 deg with a PV of 0.93 deg. The Q to V retardance aperture map has a mean value of -0.10 deg with an RMS variation of 0.10 deg and PV of 0.67 deg. The Q to U retardance

aperture map has a mean of -0.01 deg, an RMS of 0.006 deg, and a PV of 0.05 deg. Depolarization is estimated by propagating all possible fully polarized input Stokes vectors through each spatial point across the aperture. For each input vector, we average the output Stokes vectors over the aperture then compute the degree of polarization (DoP) of the resulting aperture-averaged vector.

In our first scenario, we just isolate the transmission, Q diattenuation, and the UV retardance. We make a Mueller matrix at every point across the aperture using transmission and a theoretical (physical) Mueller matrix using the measured values. In Table 6, we list the average, RMS, and PV values across the simulated aperture relevant for each parameter listed in the first column. We show in Fig. 21 a map of the depolarization as $1-(\text{DoP})$ for all fully polarized input Stokes vectors over the Poincaré sphere for the aperture averaged output Stokes vectors propagating through the simulated spatially variable optic. Figure 21(a) shows the largest depolarization at a linear polarization orientation of 45 deg and 135 deg corresponding to $\pm U$ inputs as well as circular polarization of ± 1 corresponding to $\pm V$ inputs. The lowest depolarization is seen for Q inputs corresponding to 0 circular polarization and linear orientations of 0 deg and 90 deg.

We also make a second scenario with the same spatial maps but now with 20 times increased spatial variation of the retardance terms. We also include the nonzero mean values for Q to U and Q to V retardance. We take each spatial map of each elliptical retardance component, subtract the mean, multiply by 20, and then add the mean back to this increased residual error. This increases the spatial variation without changing the mean behavior of the prior simulation. The third column of Table 6 shows the aperture statistics of the relevant Mueller matrix element. Figure 21(b) shows this scenario but now with asymmetries due to the elliptical retardance.

As a simple demonstration, we follow Chipman et al.⁹⁵ (Sec. 6.11 depolarization) and implement Eq. (6.80) also listed here in Eq. (1). We compute the average degree of polarization (AvgDoP) for all possible fully polarized input Stokes vectors (a Poincaré sphere map) shown in Fig. 21. In Eq. (1), the variable θ corresponds to the angle of linear polarization and the Stokes Q and U components. The variable η corresponds to the degree of circular polarization:

Table 6 Depolarization scenarios.

Variable	Scenario 1	Scenario 2
Transmission RMS	1.7%	1.7%
Transmission PV	40.5%	40.5%
Q diattenuation Avg	-14.9%	-14.9%
Q diattenuation RMS	0.88%	0.88%
Q diattenuation PV	17.3%	17.3%
UV retardance Avg	11.1 deg	11.1 deg
UV retardance RMS	0.19 deg	3.8 deg
UV retardance PV	0.93 deg	18.6 deg
QV retardance Avg	0 deg	-2.0 deg
QV retardance RMS	0 deg	2.0 deg
QV retardance PV	0 deg	13.4 deg
QU retardance Avg	0 deg	0.2 deg
QU retardance RMS	0 deg	0.12 deg
QU retardance PV	0 deg	1.0 deg

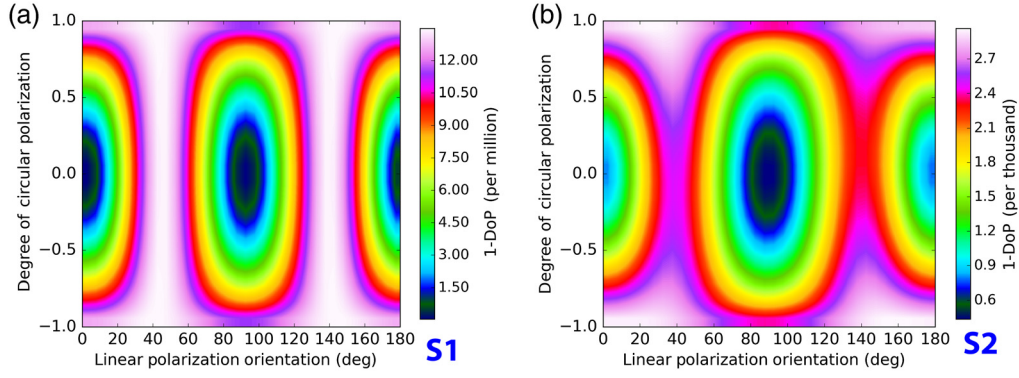


Fig. 21 The depolarization map for two different FIDO coating spatial variation scenarios computed as 1-DoP for the full range of fully polarized input Stokes vectors. The horizontal axis represents linear inputs (QU) while the vertical axis represents circular input (V). (a) Scenario 1 with transmission, Q diattenuation, and UV retardance only at nominal measured levels. (b) Scenario 2 with the fully elliptical retardance variations adjusted to be 20 times larger magnitudes than measured. (b) A few parts per thousand and (a) below 12 parts per million. As this optic has stronger U to V retardance, inputs at 45 deg and 135 deg orientation (U terms) see the highest depolarization. A pure $\pm Q$ input is preserved best with the lowest 1-DoP values.

$$\text{AvgDoP} = \frac{1}{2\pi} \int_0^\pi \int_{-\pi/2}^{\pi/2} \text{DoP}[MS(\theta, \eta)] \cos(\eta) d\eta d\theta. \quad (1)$$

We note that any Stokes vector propagating through the Mueller matrix at any single spatial point in our model would have the DoP preserved at 100%. However, when we average the Stokes vectors across the beam footprint and then compute the AvgDoP, we see depolarization in the range of 1 to 10 parts per million. As expected for our simple model, there is only UV retardance in the simulation so an input Q vector is preserved (the clean vector), while Stokes vectors with UV terms are depolarized by the spatially variable retardance. In Fig. 21(b), the symmetry is broken and the elliptical retardance tilts the regions of higher depolarization between hemispheres.

The AvgDoP index is 99.9992% in our first scenario with depolarization at 0 to 12 parts per million across the input Stokes vector map. The second scenario has an AvgDoP of 99.82%, showing a fraction of a percent depolarization caused by the 20 times increase in UV retardance spatial variation along with the fully elliptical retardance terms included also at 20 times larger spatial variation than measured. We also note that we ran these simulations with a 1000 \times increased retardance spatial variation. The AvgDoP index was 44.6% with high depolarization as expected from averaging over a highly variable aperture. Depolarization is expected to be well below a few percent at all wavelengths used by the DKIST FIDO optics, and efficiency losses are calibrated out with our standard demodulation procedures.

We note that the depolarization caused by FIDO is very small compared with other sources even within DKIST. In Ref. 14, the $F/13$ beam through the calibration retarders depolarized the beam by roughly 0.5%. In Ref. 85, we showed how a continuously rotating modulator introduced depolarization to the modulation matrix creating a few percent efficiency losses but otherwise no impact to the system calibration accuracy. In Ref. 84, we extended the modulation calculations and showed how spatially variable retardance in the modulator created depolarization causing efficiency losses as well as field dependence calibrated by standard procedures. The ViSP polycarbonate modulator upgrade in Sec. 2.6 of Ref. 84 for instance has over 30 deg retardance spatial variation but only a few percent efficiency loss when demodulated. In Ref. 66, we showed how the aperture average over the aluminum-coated $F/2$ primary mirror and $F/2$ to $F/13$ conversion of the enhanced protected silver-coated secondary mirror created diagonal depolarization at levels of 0.1% to 0.2%. In Ref. 88, we show how spatial variation of retardance across the calibration retarder and calibration polarizer both within a single beam footprint and across a misaligned, asymmetric sequence of orientations causes calibration errors. The FIDO

dichroics are static through an observation and are easily calibrated with some mild efficiency loss during demodulation at some particular wavelengths.

2.10 DL-NIRSP Dichroic Beam Splitters from Alluxa Measured in NLSP

The DKIST DL-NIRSP (DL) instrument camera arms are fed by two dichroic BSs and a mirror. These DL dichroics are from Alluxa, a different vendor than the DKIST FIDO dichroic coatings, and with different spectral optimization criteria. Narrow spectral features are also present in these dichroics. We show here transmission and reflection polarized spectra for comparison as a typical commercial solution commonly used in astronomical instruments.

2.10.1 DL BS: Mueller matrix measured in transmission with NLSP

Figure 22 shows NLSP transmission Mueller matrix data for a range of incidence angles. The nominal 30 deg incidence for DL-BS1 is highlighted in magenta. The first dichroic DL-BS1 is reflective in the 500 to 880 nm bandpass and is transmissive in the 920 to 2500 nm bandpass. The dichroic works at a nominal angle of incidence of 30 deg with a ± 3 deg spread from the converging $F/10$ beam. The dichroic is coated on a 16-mm-thick fused silica substrate with a parallelism better than 30 arc seconds over a 158 mm \times 84 mm aperture. The reflection and transmission spec is for $>95\%$ in band performance.

The second dichroic DL-BS2 is reflective in the 900- to 1320-nm bandpass and is transmissive in the 1380- to 2500-nm bandpass. The dichroic works at a nominal angle of incidence of 37 deg with a ± 3 deg spread from the converging $F/10$ beam. The dichroic is coated on a 17-mm-thick fused silica substrate with a wedge angle of 0.75 deg toleranced at ± 0.1 deg over a 138 mm \times 62 mm aperture. The reflection and transmission spec is for $>95\%$ in band performance.

These DL-NIRSP BSs have some spectrally narrow transmission features that could impact the ~ 1 nm bandpasses used in the instrument. Figure 23 shows transmission derived from the NLSP Mueller matrix measurement only at 30 deg incidence angle and only covering the appropriate specified bandpass. Some narrow spectral transmission features are seen in the shorter wavelength transition optic at amplitudes up to 10%.

The anticipated diattenuation in transmission is also less than 2% magnitude for most of the DL-NIRSP first light wavelengths. The first camera arm of DL has filters at 530.3, 587.6, 630.2, 789.2, and 854.2 nm. The second camera arm has a first-light filter set covering a narrow range of 1074.7, 1079.8, and 1083.0 nm. The retardance in transmission is spectrally smooth. The third camera arm sees both Alluxa dichroics in transmission with only two filters anticipated at DKIST first light of 1430 and 1565 nm. Figures 24(a) and 24(b) show NLSP transmission Mueller matrix data for diattenuation and retardance, respectively. Only the in-band data is

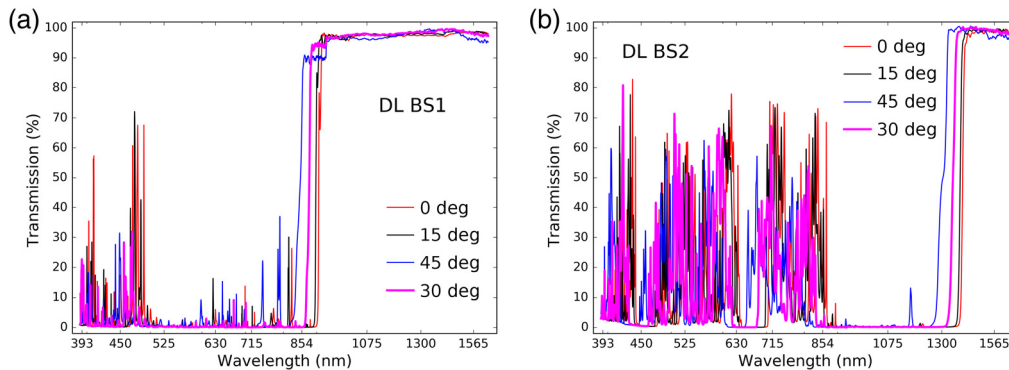


Fig. 22 DL-NIRSP spectrograph BS witness sample transmission derived from NLSP Mueller matrix data at incidence angles 0 deg, 15 deg, 30 deg, and 45 deg. (a) The first beam splitter DL BS1 with a nominal transition around 900 nm wavelength at 30 deg incidence. (b) The second BS DL BS2 with a nominal transition around 1350 nm wavelength. DL-BS2 operates at 37 deg incidence.

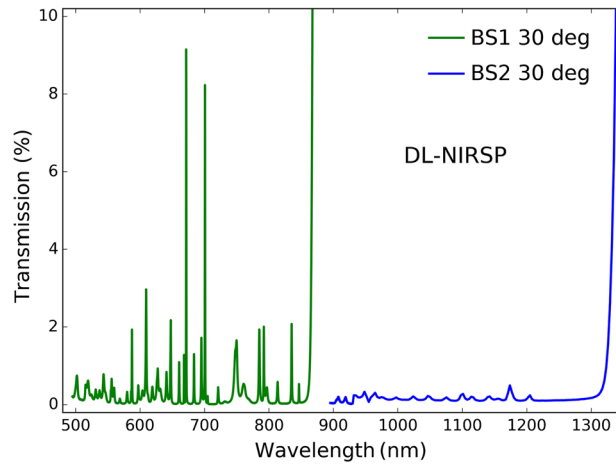


Fig. 23 DL-NIRSP spectrograph BS witness sample properties derived from NLSP Mueller matrix data at 30-deg incidence angle. Left shows the transmission with green denoting BS1 and blue denoting BS2. Only data from the appropriate transmission bandpass are shown.

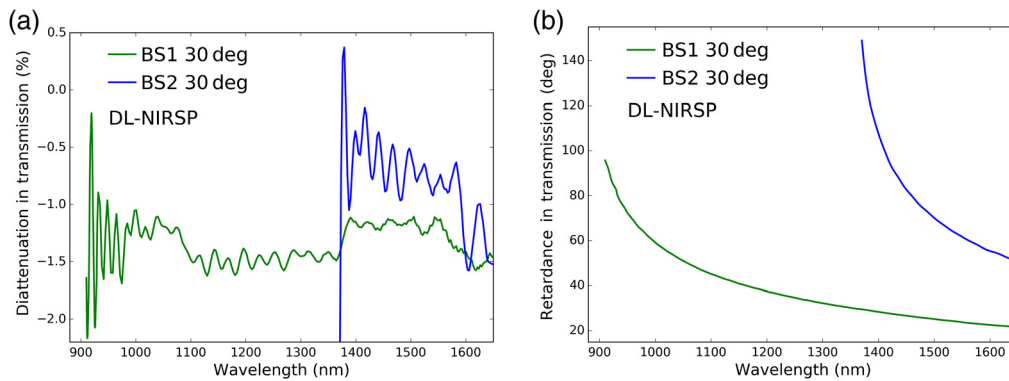


Fig. 24 The transmitted beam diattenuation in the appropriate bandpass for the DL-NIRSP BS. (a) Diattenuation. (b) Retardance. Green shows DL-BS1. Blue shows DL-BS2. We note that these BSs were designed to transmit to 2500 nm. We show both curves at 30 deg incidence though DL-BS2 operates at 37 deg.

plotted. Green shows the DL-BS1 at 30 deg incidence for wavelengths longer than 900 nm. Blue shows the measured DL-BS2 at 30 deg incidence for wavelengths longer than 1380 nm even though the actual incidence angle is 37 deg.

2.10.2 DL BS: Mueller matrix measured in reflective K-cell with NLSP

We measured the DL BSs in April, 2021, using a reflective K-cell. The K-cell is three mirrors configured to maintain the exit beam parallel to the incident beam, sometimes called an image rotator or K-mirror. The two outer mirrors of the K-cell used some of the DKIST M1 bare aluminum 2020 recoating witness samples. These two aluminum mirrors worked near incidence angles of 55 deg with ellipsometry on these samples shown in [Appendix 6.4](#). The DL BS coating sample was placed near incidence angle 30 deg in the central reflective station of the K-cell. We show here the polarized properties of the dichroic BS coatings along with the ellipsometry on the M1 outer samples. The difference between the M1 curves and the full K cell measurement is attributable to the DL BS dichroic coatings alone.

Figure 25 shows the retardance in the appropriate reflection band. The first dichroic has many narrow spectral features in retardance. The vertical red lines indicate the current DL filter wavelengths. The 789-nm filter falls on the edge of one of these features, suggesting strongly variable wavelength dependence of the retardance, which will show up in the system modulation matrix.

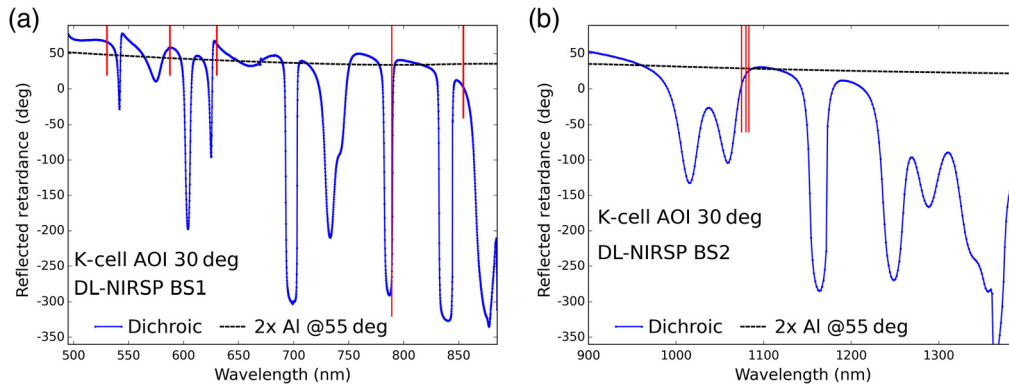


Fig. 25 The reflected beam retardance in the appropriate bandpass for the DL-NIRSP BSs for a K-cell measured in NLSP. (a) DL-BS1 working in the 500 to 880 nm bandpass. (b) DL-BS2 working in the 900 to 1320 nm bandpass. The K-cell is shown in blue. The dashed black line shows two bare aluminum mirrors alone at 55 deg incidence. Vertical red lines indicate the first light filter wavelengths in DL.

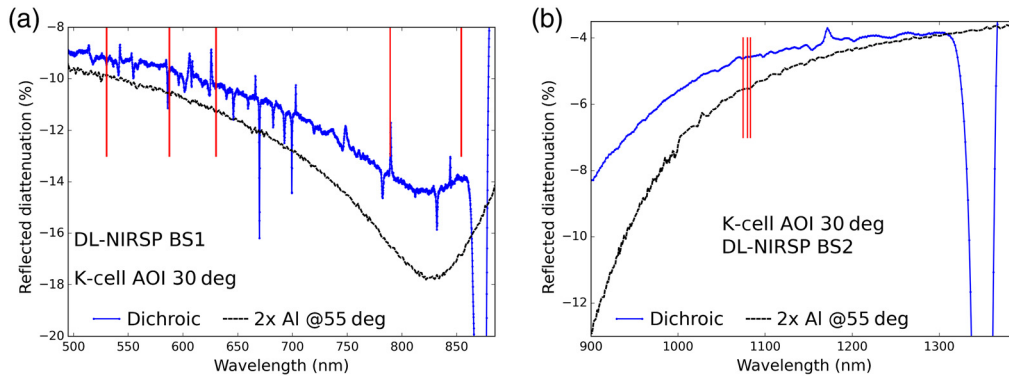


Fig. 26 The reflected beam diattenuation in the appropriate bandpass for the DL-NIRSP BSs for a K-cell measured in NLSP. (a) DL-BS1 working in the 500 to 880 nm bandpass. (b) DL-BS2 working in the 900 to 1320 nm bandpass. The K cell is shown in blue. The dashed black line shows two bare aluminum mirrors alone at 55 deg incidence. Vertical red lines indicate the first light filter wavelengths in DL.

Figure 26 shows the diattenuation of the K cell. For these BSs, the diattenuation features are much more spectrally narrow and are at magnitudes of only a few percent peak to peak. We note that our metrology system used here only has spectral resolving power of 0.30-nm FWHM. The narrowness and plentitude of the spectral features suggests a thick, many layer coating. We would need a metrology system with spectral resolving powers at or below 0.01 nm to measure the polarized spectra similar to the DKIST instruments.

2.11 Dichroic Summary

We showed in this section the detailed designs for the suite of dichroic BSs. Coating materials, designs, substrates, wedges, and materials properties were shown. We detailed the stringent wavefront requirements for power and irregularity at several nanometer RMS levels in the presence of coatings many microns thick and substrates 43 mm thick over 290 mm apertures.

For astronomical instruments working at spectral resolving powers of tens of thousands to hundreds of thousands, the narrow spectral features present in intensity and polarization require careful design consideration and high spectral resolving power metrology (FWHM < 0.3 nm). We showed detailed metrology of the BS-950 dichroic as an example of the many considerations required for doing polarimetry at high spectral resolving power with sizable optic apertures. Narrow spectral features were shown in intensity, retardance, and diattenuation. Retardance

spectral gradients of a wave per nanometer and diattenuation gradients of 10% per nanometer were present. Spatial variation of the coating properties was very strong functions of wavelength. We showed another commercial vendor dichroic used in DKIST DL-NIRSP as a comparison. Another two commercial dichroics from Thorlabs showing the same behavior is detailed in [Appendix 7.10](#). We show similar detailed metrology for all other DKIST FIDO dichroics in [Appendix C](#).

We detailed an example of coating spectral and spatial variation of diattenuation and elliptical retardance using our custom NSO Mueller matrix spectral mapping equipment as well as commercial ellipsometry. We showed transmission spatial variation for both coating and substrate properties at spectral resolving powers of 0.3 nm. We showed substrate stress birefringence and intrinsic birefringence combined with coating variation. Apertures ranged from 84 to 290 mm diameters to show how even relatively small dichroic filters would be subject to spatial and spectral variation of intensity and polarization.

These spatial nonuniformities were strong functions of wavelength. Beam apodization and depolarization are consequences that can be anticipated and calibrated. Dichroic coatings can be designed for low diattenuation and spectrally smooth retardance. With high spectral resolving power models and metrology, astronomical instruments can plan for and calibrate the behavior of these dichroics. These spatial and spectral variations are to be expected for thick dichroic coatings, but the impacts can be easily mitigated through care in design, appropriate metrology and samples to measure the actual coating performance, and calibration techniques that account for both spectral and spatial variation of all elements of the Mueller matrix.

3 System Model for DKIST Instruments

We show examples of system throughput to instrument modulators and derivation of modulation matrices using the metrology for all coated optics. Characterization of all coated optics at appropriately high spectral resolving power over a wide wavelength range allows for accurate estimation of many astronomically relevant instrument performance parameters. As examples, we show here the prediction of the ViSP modulation matrix using a typical first light FIDO configuration using the mirror (C-M1) and a window (C-W2). With the dichroic coating spectra presented in this paper, it is straightforward to predict modulation matrices for any dichroic or window combination. We used the relatively low ultraviolet throughput at 320 to 350 nm along with UV irradiation testing to show polycarbonate would be long lasting when used as modulators within DKIST instruments. We fabricated polycarbonate modulators for ViSP and DL-NIRSP.

3.1 ViSP: Optical Overview and Deriving Modulation Matrices

The ViSP instrument is fed by a transmission through the optic at FIDO station CL2a. The ViSP feed optics follows a Schiefspiegler type with spherical mirrors optimized for the slit focal plane. After the slit mask, the beam is folded, propagates through the modulator and then is folded twice again before reaching the collimating lens. The pupil image forms on the grating and is dispersed. Three camera arms each with their own lenses, select particular bandpasses for imaging through polarizing beam splitters. [Figure 27](#) shows the optical design layout.

3.2 ViSP: Fold Mirror Ellipsometry for RMI Coating on FM2, FM3, FM4

Retardance and diattenuation spectra at the appropriate incidence angle are required for every optic ahead of the analyzer to create an accurate modulation matrix prediction. We showed previously in [Ref. 86](#) examples of mirror coating measurements typically only at 45 deg incidence. In our previous works, we used a coating model derived from 45 deg incidence data sets to predict performance at other incidence angles. Of course, having an accurate coating model enables other more detailed analysis such as assessing depolarization and Mueller matrix behavior when averaging over a footprint in powered optics at diverse incidence angles or in an optical system with nonzero FoV. We did preliminary estimates in [Ref. 66](#). Ellipsometry vendors can provide metrology on samples at a range of incidence angles as an alternate option with the associated cost and schedule.

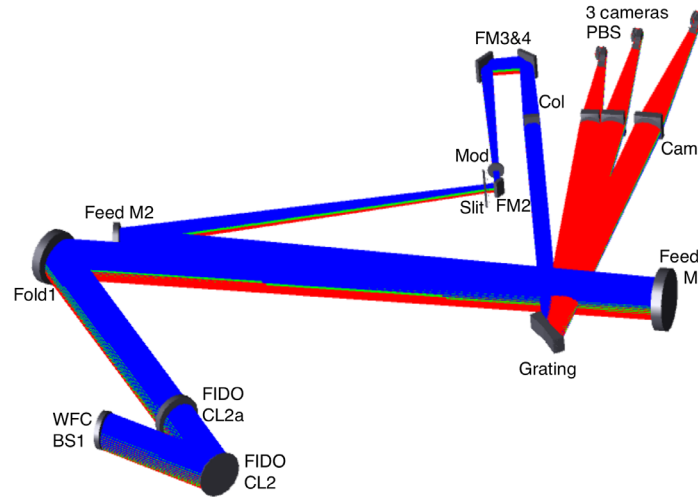


Fig. 27 The ViSP optical path for a particular configuration. We begin with the beam transmitted through WFC-BS1. FIDO station CL2 reflects to ViSP while station CL2a transmits to ViSP. The ViSP instrument relay optics then use Fold 1, Feed 1, and Feed 2 to create the F/ 32 focus on the slit mask. The beam diverges through the slit to a series of fold mirrors (denoted FM). FM2 folds onto the rotating elliptical polycarbonate modulator. Then FM3 and FM4 direct the beam back to the collimating lens. The grating reflects and disperses to three arms each with camera lenses (Cam) along with filters and the PBS.

We show here example ellipsometry data from J.A. Woollam on the ViSP fold mirrors 2, 3, and 4. Mirrors 3 and 4 share the same coating run and both are mounted in the beam at the same 45 deg incidence angle. ViSP fold mirror 2 was a different coating run and is used at 47.7 deg incidence. Figure 28 shows ellipsometry-derived retardance and diattenuation for both coating witness samples covering incidence angles from 15 deg to 60 deg in steps of 5 deg. Even though FM2 has nominally the same coating, the typical shot to shot coating layer thickness variation produces obvious and substantial differences between coating runs.

3.3 ViSP: Coating Model for the Entire Optical Feed

Creating a modulation matrix requires a Mueller matrix for every coated optic for every wavelength at the appropriate incidence angle. We created a simple model for our metrology tool called the National Solar Observatory Coudé Spectro-Polarimeter (NCSP) shown in Sec. 5,

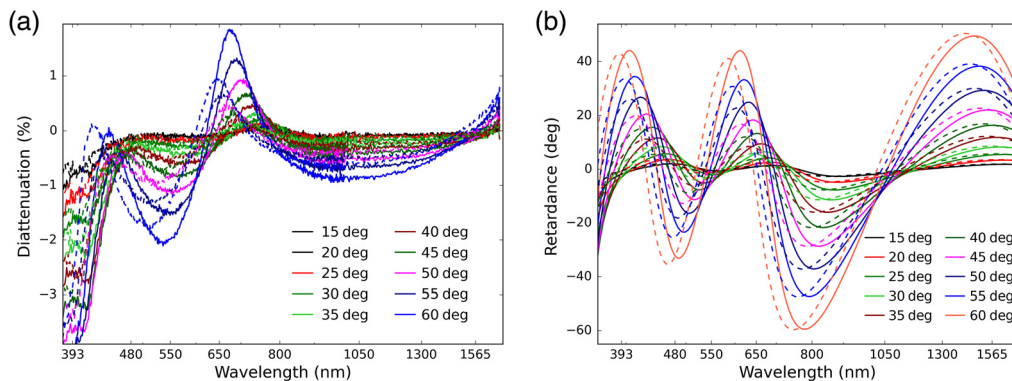


Fig. 28 The Woollam ellipsometry for the two enhanced protected silver RMI coatings on ViSP fold mirrors after the modulator. FM2 is coated with one run at AOI 47.7 deg shown as the solid line. Mirrors FM3 and FM4 in the second coating run are shown as dashed lines and both are mounted in the instrument at 45 deg incidence. Measurements were done at incidence angles of 15 deg to 60 deg in steps of 5 deg. (a) Diattenuation. (b) Retardance. The two coatings are similar but with noticeable thickness differences between runs.

Figs. 13–15 of Ref. 87. For a DKIST scientific instrument, the optical feed is typically more complex and involves at least one dichroic coating.

We show calculations for the ViSP here. An abbreviated table showing only the mirrors in the modulation matrix model is shown in Table 7. Ellipsometry for several coatings shown in Appendix C of Ref. 87 has been done on witness samples for every mirror in this list at incidence angles from 15 deg to 60 deg in steps of 5 deg. There are several mirrors at incidence angles at or below 10 deg where the mirror coating properties are below typical systematic error limits and are ignored. For instance, we note in Appendix 6.3 that we have ellipsometry on DKIST M9 which matches a coating model of 30-nm ZnS overcoating 30 nm of Al₂O₃ very well. At 10 deg incidence, we choose to ignore the polarization for this coating to reduce noise from any metrology or interpolation. The predicted retardance and diattenuation at 10 deg incidence is small. We note that the antireflection coatings are mostly known and have little polarization influence. We detail in Appendix D of Ref. 86 the known antireflection coatings for the DKIST optics as well as the ViSP lenses. See Figs. 69, 71, and 72 of Ref. 86. Vendors for the coatings in this

Table 7 Modulation matrix: incidence and coatings.

Optic	AOI (deg)	Source	Coating
M7	45	Ellipsometry	D.EAg
M8	5	Ignore	EMF (elip. data)
M9	10	Ignore	Zygo (elip. data)
M10 DM	15	Ellipsometry	D.EAg
WFS-BS1	15	Ignore	IOI WBBAR1
C-M1	15	Ellipsometry	IOI 6-7766
C-BS-W2	15	Ignore	IOI WBBAR1
V-FoldM1	28	Ellipsometry 27.5 deg	IOI 6-7879
V-Feed1	2.2	Ignore	IOI 6-7879
V-Feed2	12.3	Ellipsometry 15 deg	IOI 6-7767
Slit glass	5.4	Ignore	ECI
V-FoldM2	47.7	Ellipsometry 47.5 deg	RMI
Modulator	0	Rotating retarder	MLO, IOI
V-FoldM3	45	Ellipsometry	RMI
V-FoldM4	45	Ellipsometry	RMI
V-Coll	0	Ignore	IOI AR
V-Grating	Var	Diattenuator	Newport, AI
V-Cam	0	Ignore	IOI AR
V-Filters	0	Ignore	—
V-PolBS L1	0	Ignore	Optimax AR
V-PolBS	0	Analyzer	—
V-PolBS L 2	0	Ignore	Optimax AR
V-FoldM5	45	Ignore	Prot. Ag
V-BeamCom	67.5	Ignore	Prot. Ag

system model include evaporated metal films (EMF), Zygo Corp., Infinite Optics Inc. (IOI), Evaporated Coatings Inc. (ECI), Rocky Mountain Instrument (RMI), Newport Richardson Grating Labs (protected aluminum), and Optimax. Meadowlark Optics (MLO) fabricated the modulator using windows coated by IOI.

For optics after the analyzer, the polarization response contributes to an imbalance between the brightness of the orthogonally polarized dual beams. The polarizing beam splitter (PBS) has telecentric lenses on both entrance and exit interfaces (L1 and L2, respectively). The beam leaving the PBS is folded by mirror number 5 (FoldM5, FM5) at 45 deg incidence and the beam combiner assembly (BeamCom) at 67.5 deg incidence. The retardance and diattenuation do not contribute to the modulation matrix. We discuss the coatings and beam imbalance caused by the reflectivity differences between S and P beams on these optics (Fig. 29).

Another complication in modeling the DKIST science instruments is that the modulator can be used over a range of orientations and with variable starting angle. The modulator was detailed in Ref. 84 with custom coatings from IOI. Thus, we separate the mirror coating model into a grouping of mirrors ahead of the modulator and behind the modulator. DKIST instruments, like most astronomical SPs, are designed with mirror fold angles in the $\pm Q$ plane along with a $\pm Q$ analyzer. This way mirrors can be combined (grouped) together, and the mirror retardance does not degrade modulation efficiency. We show such a combination of the ViSP mirrors in Fig. 29.

3.3.1 ViSP: polycarbonate modulator

The modulator for ViSP is a rotating elliptical retarder fabricated using three layers of polycarbonate. The optic is described extensively in Ref. 84. It was designed to mitigate interference fringes in the ViSP $F/28$ beam as well as providing beam deflection of 2.3 arc seconds to minimize beam wobble and artifacts from the corresponding image motion as the modulator rotates. The modulator is mounted after the slit, which protects the modulator from substantial heating and UV damage. The slit is addressed in more detail in Appendix 5.2.1.

3.3.2 ViSP: diattenuation model for the grating

A further detail required to estimate beam throughput is the grating diattenuation to get the relative beam efficiencies correct. Gratings are also mounted to fold and diattenuate in the $\pm Q$ plane, parallel to the analyzer orientation. ViSP uses a 316 line per mm Newport Richardson Grating Lab blazed at 63.4 deg. The grating was coated by paradigm, depositing a nominal coating of 70 nm of Al protected by 25 nm of SiO_2 . Each order of a coated grating has variation in Q diattenuation with wavelength and dispersion angle. The ViSP can be configured with a range of grating tilt angles to send a range of spectral orders to the three separate camera arms. The camera arms also rotate about the grating to ensure that the particular wavelength from the particular grating order is imaged on the center of the sensor. The ViSP IPC optimizes the

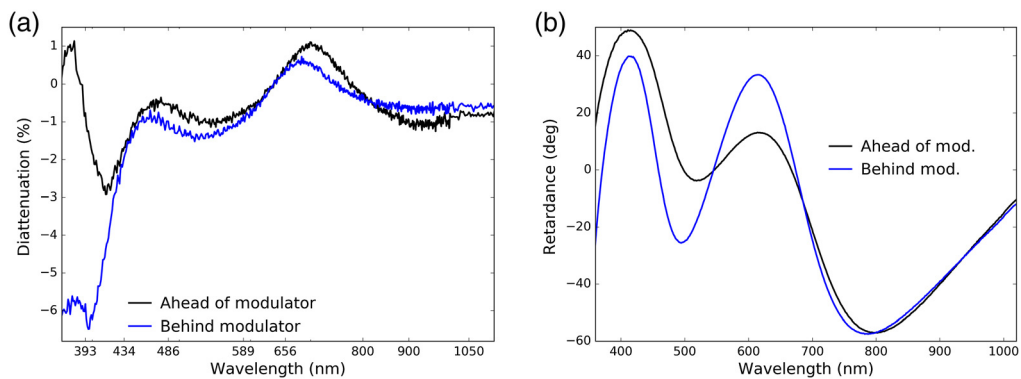


Fig. 29 (a) The diattenuation of the various mirrors grouped ahead and behind of the modulator to derive the modulation matrix in a particular ViSP configuration. (b) Retardance combined for the two optic groups.

grating and camera angles to ensure high throughput accounting for the intensity of both polarization states. The grating polarization also needs to be modeled and measured to make an accurate prediction of the beam intensities through the analyzer.

With a system model based on metrology for the coating polarization ahead and behind the modulator, it becomes relatively straightforward to insert the modulating retarder at a range of orientations and rotational schemes along with a grating Q diattenuation to predict the actual modulation matrix elements in a range of configurations. As an example, Fig. 30 shows the ViSP team grating reflectivity and diattenuation used in the IPC. Modeling polarization of gratings including protected aluminum coatings along with polarization mitigation using shadow casting techniques is an ongoing effort.^{96,97} Figure 30(a) shows the transverse electric (TE) mode for the P linear polarization state as blue lines with the transverse magnetic (TM) mode for the S linear polarization state as red lines Figure 30(b) shows the Q diattenuation in black. As the grating tilt angle is varied about the 63.4 deg nominal blaze, the different orders selectable by the ViSP cameras will have different intensities and also different balance between the two orthogonally analyzed beams.

3.3.3 ViSP: polarizing beam splitter and beam combiner

The PBS assembly lives after the grating reflection, camera lens transmission, and both prefilter and order sorting filter optical stations. This optic separates two orthogonally polarized linear states in the $\pm Q$ local coordinate frame (horizontal and vertical with respect to the optical bench) and functions as the analyzer. The polarization state of the beam exiting the analyzer is always $\pm Q$ with the brightness (not polarization) varying as the modulator rotates. The diattenuation and retardance of subsequent optics such as fold mirror 5 and the beam combiner assemblies contribute to the relative intensity difference between the beams (beam imbalance). A contrast ratio minimum of 20:1 was specified so $>95\%$ of the efficiency is preserved through this BS. The optical performance of these components is detailed in Appendix A. For modeling the modulation matrix, we need to only know that the modulation is preserved to better than 95% through the contrast ratio specification. Throughput and a flux model does require the reflectivity of both polarization states.

3.4 ViSP: Modulation Matrix Summary

We show in this section a coating model from DKIST M7 through the FIDO dichroics and all significant contributing ViSP optics using metrology at appropriate incidence angles. Similar to the NCSP system calibrations presented in Ref. 87, all optics from M7 to the modulator

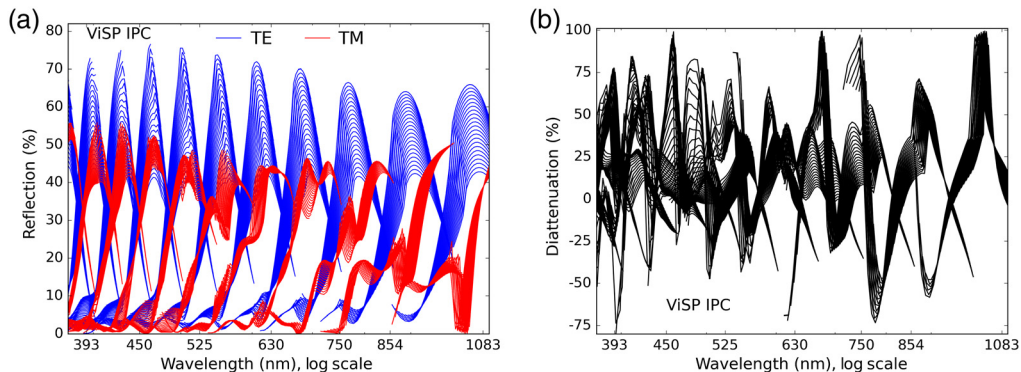


Fig. 30 (a) The reflectivity for P in blue and S in red as example performance calculations for the ViSP grating used in the IPC. (b) The diattenuation. Each curve shows a different angular configuration including the grating diffracted exit angle for a range of grating tilt angles. The ViSP instrument can tilt the grating as well as rotate the three camera arms about the grating to measure particular grating orders. The IPC optimizes the camera and grating orientations to put three desired wavelengths in the three different camera arms selecting different grating orders and grating tilt angles, optimizing polarization performance given the reflectivity and diattenuation.

contribute to the modulation matrix. Optics behind the modulator are designed to preserve and analyze Stokes Q . Unlike NCSP, the ViSP has multiple folds and a grating between the modulator and the analyzer. These aft optics preserve Stokes Q exiting the modulator. The grating diattenuation calculations contribute to the relative balance to the two orthogonally analyzed beams. With these coating and grating models, estimation of the field dependence and a tolerance analysis is straightforward. Details are in [Appendix A](#).

4 Summary of Coating Impacts for DKIST

The FIDO beamsplitter suite provides DKIST with an enormous flexibility for reconfiguration of the science beam for a large variety of observing scenarios with the available instruments. Meeting each substrate's optical specification in terms of reflected and transmitted wavefront over their clear aperture of 290 mm is challenging alone. However, significant additional consideration has to be given to the thick dichroic coatings with tens to nearly one hundred layers and over 8 μm physical thickness. These coatings produce narrow spectral features that can change diattenuation by more than $\pm 10\%$ and more than a full wave of retardance. Metrology should include high spectral resolving powers, a factor of 10 or so narrower than more common vendor reports at few nanometer bandwidths. The spatial uniformity of coatings is a strong function of wavelength, being an order of magnitude or two worse around the narrow spectra features than at other wavelengths. However, coatings can be designed with diattenuation constraints to minimize the coating process to layer thickness variations. We show in the [Appendix C](#), in particular Secs. 7.3 and 7.2, examples of how the coating models do predict narrow spectral features, but the exact wavelengths and spectral form of the models do not match the as-built metrology in all details. For astronomical instruments working with narrow spectral lines at resolving powers of 10,000 or greater, consideration of these features seems essential to instrument design and fabrication.

The coating thickness uniformity and coating stresses create issues for both reflected and transmitted wavefront shown in Sec. 2.3. Additional issues with substrate thickness, stiffness, and birefringence require consideration. We showed here coating stress measurements and their temporal evolution with a prebiasing process. This was used to keep the power in the reflected beam below 24-nm RMS with irregularity below 8-nm RMS over that 290 mm aperture with coatings at 8 μm thickness.

A detailed examination on the worst-case DKIST dichroic, BS-950, was shown in Sec. 2.8. We showed examples of substrate intrinsic birefringence and stress birefringence. Spectral features, spatial uniformity variation with these spectral features, and depolarization estimates were created. We summarized the FIDO reflected and transmitted polarization properties with narrow spectral features measured in all our dichroics in [Appendix C](#), in DL-NIRSP commercial dichroics in Sec. 2.10 and other commercial dichroics shown in [Appendix 7.10](#). Figure 31 shows the polarization properties of all the DKIST FIDO dichroics in reflection with our 0.3-nm FWHM system to show the narrow spectral features. Retardance is shown in Fig. 31(a) while the diattenuation is shown Fig. 31(b). With the polarization information measured, we can predict modulation matrices and perform tolerance analyses for the entire Coudé lab optical path.

The suite of FIDO dichroics allows for very diverse distribution of wavelength band passes to different DKIST instruments with either high reflection or transmission as appropriate. With the FIDO dichroic metrology covering UV to thermal IR wavelengths, and all the associated reflectivity and polarization measurements in [Appendix C](#), accurate flux budget estimates are possible for any FIDO configuration including out-of-band performance. Figure 32 compares system throughput of different mirror feeds FIDO dichroic BSs and windows feeding the AO system through BS1 as well as all currently installed DKIST instruments. The CN instrument using the M9a reflective path in magenta has throughput above 75% to the modulator. The ViSP using FIDO CM1 shown in green receives more than 50% throughput at 393 nm using the enhanced silver mirror coatings. Figure 32 shows two options for DL-NIRSP with transmission through BS1 and three other FIDO dichroics shown as red lines. Solid red shows a common configuration with BS-465 sending short wavelengths to another instrument (e.g., VBI-Blue and ViSP). Dashed red shows another common option where BS-465 is used along with BS-950. The two

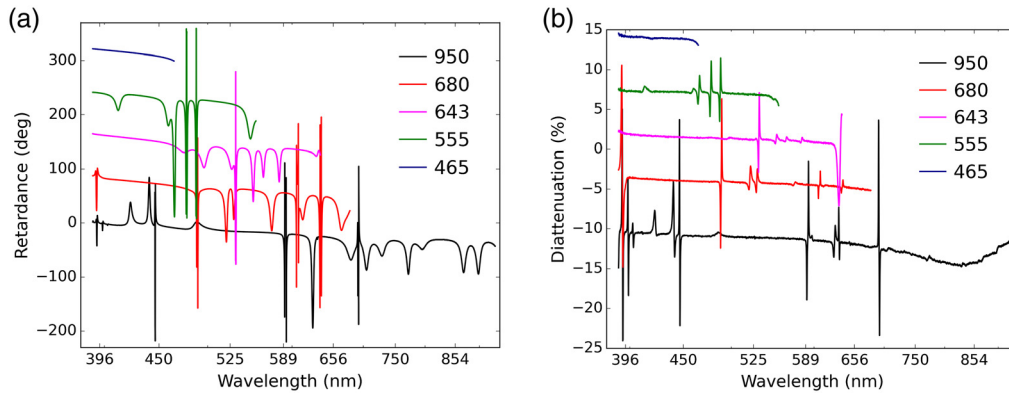


Fig. 31 (a) The FIDO dichroic reflection retardance. (b) Diattenuation. Curves have been offset vertically for clarity. Each dichroic BS is named for the transition wavelength, and we only show the nominal reflection band as appropriate. The narrow spectral features have roughly 1-nm FWHM and will be included in DKIST performance predictions.

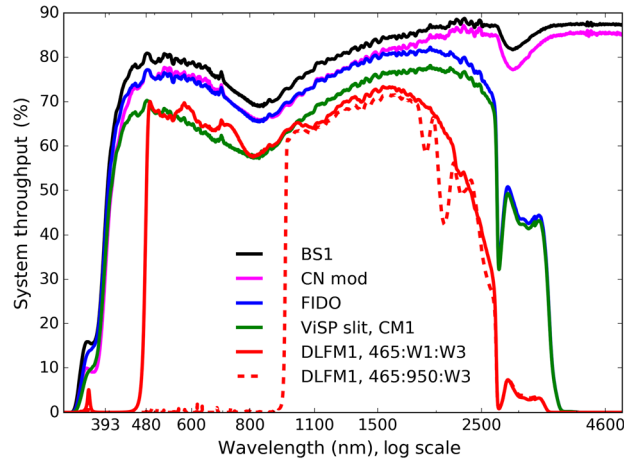


Fig. 32 The DKIST optical system throughput at select optical stations. Black shows the throughput for the beam incident on WFC-BS1 as fed by mirrors 1 to 10. Magenta shows the beam incident on the CN modulator. Blue shows the impact of BS1 substrate absorption for the beam incident on the first FIDO station. Green shows the beam incident on the ViSP slit with C-M1 installed. The red curves show the beam incident on DL-NIRSP FM1 after passing through various FIDO dichroics and windows. In general, the system is 60% to over 80% efficient at flux delivery to the instrument suite.

infrared channels of DL-NIRSP would be active, and now combined with VBI-Red and VTF. These examples show the flexibility available to DKIST users enabled by the FIDO dichroics while preserving high system throughput.

5 Appendix A. ViSP Instrument: Throughput, Coatings, and Modulator

In this appendix, we provide details for creating a polarization and throughput model for the ViSP. We present ellipsometry on optical coatings, contrast, and throughput measurements for the analyzer and details about several optical elements to be considered for the system Mueller matrix model. Several changes have occurred to the ViSP system. Two instrument feed mirrors were stripped and recoated. We have measured reflectivity of many new witness samples at MLO to inform the flux budget. We also have new polarization measurements from NLSF on several optic witness samples including the IOI coated instrument feed optics and the RMI coated spectrograph mirrors. We also have provided a polycarbonate modulator for upgrade that has

Table 8 ViSP optic coating status.

Optic	AOI (deg)	Run	Note
FM1	28	IOI 6-7881	6-7768 stripped
F1	2.2	IOI 6-7879	6-7766 stripped
F2	12.3	IOI 6-7767	Unchanged
Slit	5.4	ECI	BBAR
FM2	47.7	RMI Y31071216	EAg
Mod	0	IOI 12-6719	wbb2-520-bk7
FM3	45	RMI Y31121216	EAg
FM4	45	RMI Y31121216	EAg

different transmission properties than the six-crystal modulator. In Table 8, we show some of the additions and changes to the ViSP feed optics beginning after the last DKIST dichroic feed optic. For instance, the ViSP fold mirror 2 is ahead of the modulator at 47.7 deg incidence. The reflectivity and polarization properties were reported in Appendix C5, Figs. 37 and 38 of Ref. 87.

The first and second ViSP feed mirrors were stripped and recoated after the results published in Ref. 86 after some mild scuffing was discovered inside the clear aperture. To achieve uniformity and consistency on the relatively large ViSP optics, IOI performed two separate coating runs. Coating run 6-7879 contained the ViSP fold mirror 1, denoted F1. Coating run 6-7881 contained the ViSP feed mirror 1, denoted FM1.

5.1 ViSP Fold Mirrors 2,3,4: RMI Multilayer Silver Coatings

The ViSP team procured many-layer protected silver-coated mirrors from Rocky Mountain Instrument. Note that limited reflectivity measurements on the ViSP FM2 coating performed by RMI for both S and P polarization states was published in Appendix C.9, Fig. 66 of Ref. 86. In Fig. 34(a), we show the collected reflectivity testing done at RMI as well as our scans from the MLO Cary system. The RMI reflectivity measurements for ViSP FM2 are shown as solid lines with blue and red as the S and P polarization states, respectively. The solid black line shows the average of these two data sets to represent unpolarized reflectivity. The dashed black line shows the RMI data on ViSP FM3&4 coated in the same run as no polarization information was collected. The MLO data set shown in purple is significantly lower than the RMI data

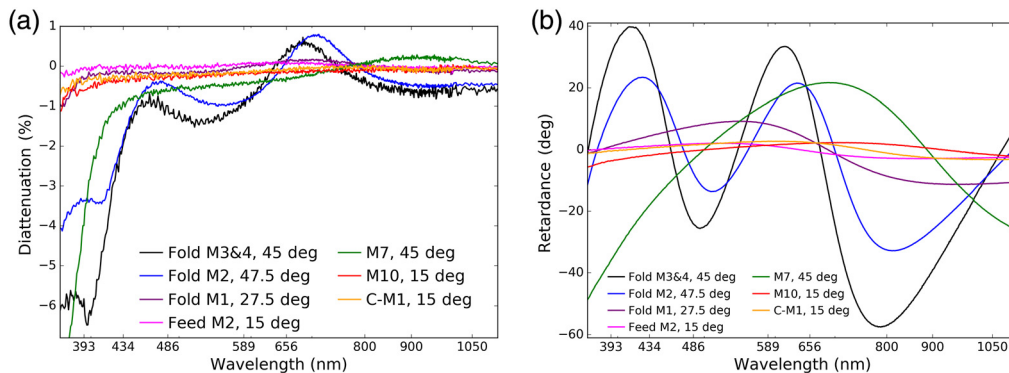


Fig. 33 (a) The diattenuation of the various mirrors used in the groupings to derive the modulation matrix in a particular ViSP configuration derived from Woollam ellipsometry Mueller matrix measurements. (b) Retardance. Each mirror is graphed at the appropriate incidence angle. As all the mirrors fold in the horizontal (local Q) plane, these terms simply add to first order.

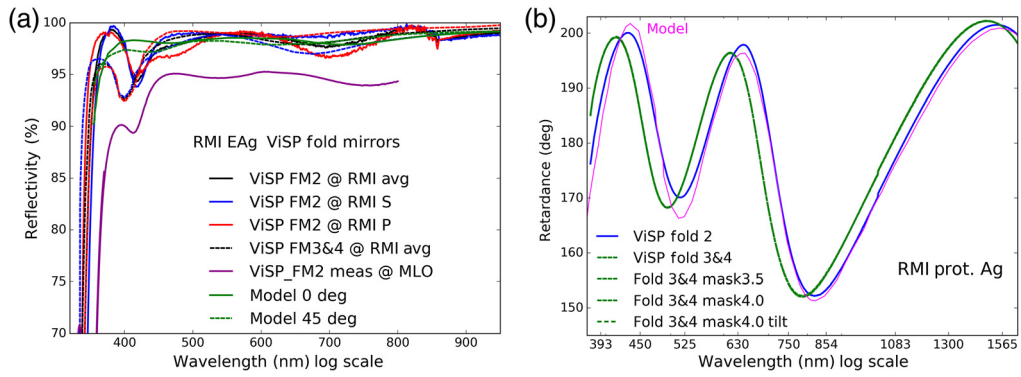


Fig. 34 (b) RMI reflectivity data done at the time of coating as well as our Cary scans with the MLO system and the associated RMI TFCalc model. (a) Retardance derived for a many layer protected silver coating from the commercial vendor Rocky Mountain Optics (RMI) compared with our metrology data.

sets on different samples. The RMI TFCalc model predictions are shown in green at two incidence angles and are much smoother than the RMI data sets.

The DKIST team procured one sample from each coating run from RMI and ran a reflective retardance and diattenuation measurement in our Boulder-based custom lab system (NLSP). Retardance is shown in Fig. 34(b). Note that alignment and repeatability tests were done with the RMI sample for the coating used on the ViSP fold mirrors 3 and 4. NLSP lamp masks were exchanged and the sample was also mildly tilted to change the optical alignment of the setup. The retardance curves vary by less than ± 0.2 deg peak to peak shown as the good agreement between the four green curves in Fig. 34(b). The blue curve shows the FM2 coating sample NLSP data. The magenta curve shows a vendor model for retardance which closely tracks the blue curve for the FM2 sample measurements.

5.2 ViSP: Polarizing Beam Splitter, FM5, and Beam Combiner

The PBS functions as the analyzer with a contrast ratio always above 20. This represents signal preservation of 95% or better. The fifth ViSP fold mirror (FM5) and beam combiner mirror together contribute mildly to throughput losses. Figure 35(a) shows an annotated image of one of the ViSP camera arms. Figure 35(b) shows the Zemax optical design beginning from the order sorting filter station through the sensor focal plane. This assembly consists of a BS cube operating at 45-deg incidence with telecentric lenses on both entrance and exit interfaces of the cube.

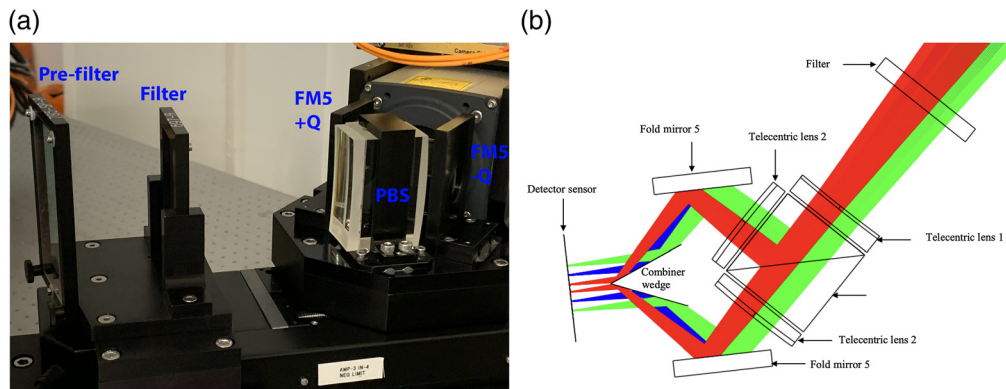


Fig. 35 (a) A single ViSP camera arm with the two rectangular filters, PBS cube assembly and fold mirror 5 reflections for both $\pm Q$ beams exiting the PBS. The beam combiner wedge is not visible in the image as it is hidden behind the PBS immediately in front of the Andor Zyla sensor. (b) The Zemax optical design for this assembly.

The BS has local $\pm Q$ Stokes parameters exit the assembly with linear polarization states fixed in time and closely aligned with horizontal and vertical directions referenced to the optical bench.

The ViSP PBS was made of a high index Ohara S-LAH-65-V glass with high transmission at short wavelengths. The surfaces were coated by OptiMax and had 0.93% average unpolarized reflectivity from 380 to 900 nm wavelength. Spectral oscillations shown for this coating in Fig. 72 of Ref. 86 were present with reflectivity between 0.67% and 1.20% over the bandpass. Figure 36 shows the contrast ratio measured for both beams exiting one of the ViSP PBSs. The beam internally reflected within the cube has a contrast above 20 at the shortest wavelength rising to over 150 for all other wavelengths. The beam internally transmitted through the cube interface has a contrast oscillating from 20 up over 200 with a somewhat erratic wavelength dependence.

Both orthogonally polarized beams exiting the PBS reflect off the fifth fold mirror (FM5) which is an off the shelf Thorlabs mirror. The nominal coating performance published (as of August, 2021) for the “P2”-type protected silver on Thorlabs website shows good performance at 45 deg incidence angle. Unpolarized reflectivity is greater than 95% at 380 nm rising toward 98% reflectivity at 1000 nm covering all ViSP wavelengths. The diattenuation is 3% at 380 nm falling to 2% at 440 nm and is below 1% longer than 480 nm.

Commercial coatings are commonly not required to use the same materials, same formula, or to have repeatable polarization performance. For instance, we showed Thorlabs protected silver coatings varying substantially shot to shot in Fig. 40 of Ref. 87. We showed in Fig. 54 of Ref. 86 some variation at small amplitudes measured in three Thorlabs mirrors bought at the same time in the same order. We funded J.A. Woollam to perform ellipsometry on a spare ViSP FM5 procured in the same batch with the other three ViSP FM5 mirrors included in each ViSP camera arms. Figures 37(a)–37(c) show the incidence angle-dependent reflectivity, diattenuation, and retardance, respectively. The black curve shows the nominal 45-deg incidence angle usage. For reflections after the analyzer exit, any differences in *S*- and *P*-reflections lead only to intensity differences on the sensor (beam imbalance). This coating should maintain the beam balance to the nominal diattenuation values of a few percent or better.

The beam combiner is made from a prism with two sides reflecting at 67.5 deg incidence. The prism uses a special Opto-Sigma coating designed with a >99% reflectivity goal over the bandpass. The ellipsometry performed by J.A. Woollam on both sides of a spare coated prism is shown in Fig. 38. The unpolarized reflectivity in Fig. 38(a) shows both sides have similar behavior with relatively narrow spectral features from this relatively thick coating. The *S*- and *P*-transmission differences (diattenuation) shown in Fig. 38(b) contribute to beam imbalance

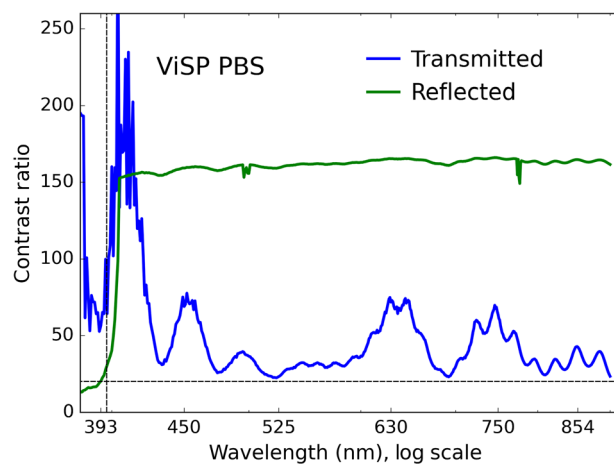


Fig. 36 The contrast ratios for both beams exiting the ViSP PBS cube. Green shows the beam reflected off the internal interface at 45 deg incidence with contrast near 20 for the 393 nm line, rising to 28 for the 396 nm line then rapidly rising to over 150 for the rest of the ViSP bandpass. The blue line shows the beam transmitted through the internal PBS cube interface. Contrast varies somewhat erratically with wavelength between 20 and over 200.

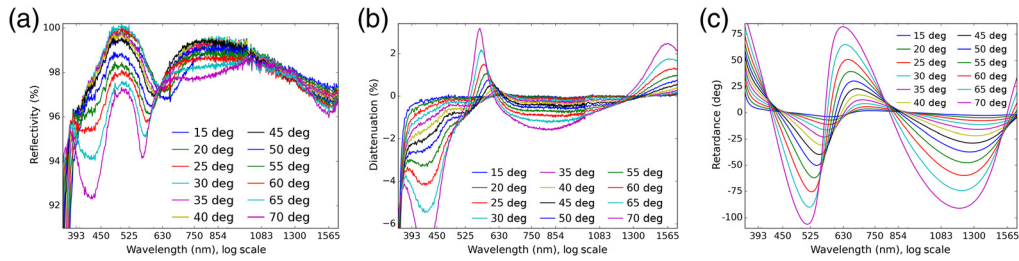


Fig. 37 The Woollam ellipsometry measured on one of the ViSP fold mirror 5 spare mirrors measured at incidence angles of 15 deg to 70 deg in steps of 5 deg. These three commercial Thorlabs mirrors use protected silver coatings and nominally fold at 45 deg incidence. (a) Reflectivity, (b) diattenuation, and (c) retardance.

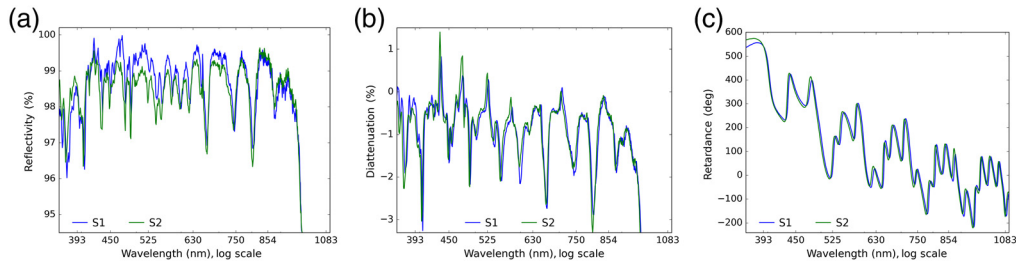


Fig. 38 Ellipsometry on the spare ViSP beam combiner prism coated faces measured at 65 deg incidence. We note the optic normally reflects 2.5 deg higher incidence of 67.25 deg. (a) Unpolarized reflectance, (b) diattenuation, and (c) retardance. The blue curves show one side of the prism. Green curves show the opposite side coated in a different run.

delivered to the ViSP cameras, but are less than a few percent in the ViSP bandpass. The grating polarization shown in Sec. 3.3.2 (Fig. 30) is very dependent on the grating angle and camera configurations and combines with all other Q diattenuation terms contributing to the beam imbalance. The retardance for this prism coating oscillates by a few waves as a strong function of wavelength. As this optic is after the analyzer and is mounted to see a fully Q polarized beam, the retardance can be ignored to first order. The optic is in an $F/7$ converging beam with some significant angular spread, but the retardance would only marginally contribute to spatial transmission inhomogeneities and other higher order effects.

5.2.1 ViSP: Slit Polarization

The slit masks are etched from an aluminum coating on a 12.5-mm-thick fused silica glass substrate reflecting and transmitting at 5.4-deg incidence angle. The etched masks are then overcoated with the ECI antireflection coating. We showed Fig. 72 of Ref. 86 all the antireflection coating curves for the ViSP optics. We also showed that the diattenuation caused by the nonzero incidence angle with DKIST AR coatings was well below 1% for 15-deg incidence. The diattenuation at 5.4-deg incidence is negligible. The polarization in transmission through a slit could possibly contain some mild diattenuation. The ViSP slits range from 17 to 130 μm in width with diffraction playing a small but nonzero role. Substrate birefringence as well as stress birefringence are also possible with any transmissive substrate. For polarization calibration of the ViSP, we note that the polarization behavior of the slit is captured in the calibration of the instrument modulation matrix. Provided the polarization artifacts are stable, they will be calibrated. For the performance predictions here, we ignore estimation of the small diattenuation and retardance terms from the coated glass slit mask.

Figure 39 shows the ViSP slit optic station during installation in 2020. Figure 39(a) shows the view looking at the slit station from a position just behind the ViSP feed mirror 2 station as illuminated by the GOS calibration lamp. The 2.8-arc minute field stop at Gregorian focus

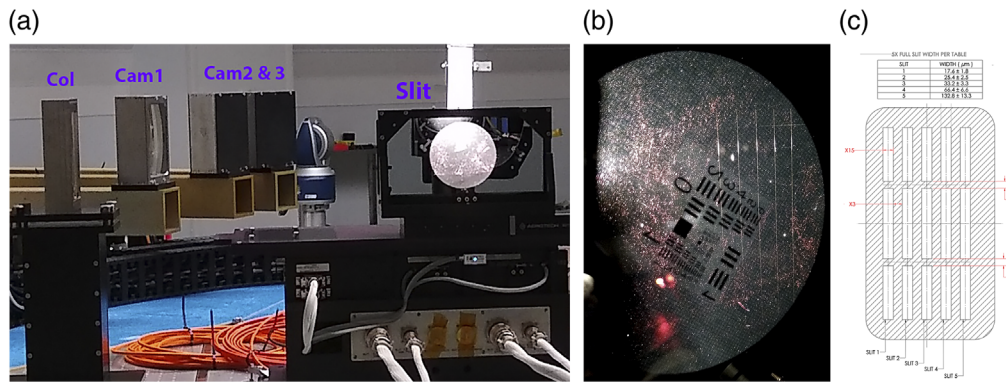


Fig. 39 The ViSP slit station. (a) The rectangular slit mask optic illuminated by the 2.8 arc minute circular field using the GOS lamp. The beam is mostly reflected by the aluminum coating on the front of the slit optic glass towards an absorbing beam dump. In the graphic a few other ViSP optics can be seen: the collimator (Coi) and the three camera lenses (Cam 1, 2, and 3) within each of the three spectrograph arms. (b) The air force resolution target deployed at Gregorian focus as reimaged onto the ViSP slit mask. The slits can be seen as the narrow vertical features in the coating decentered to the right glinting slightly. (c) The drawing of the etched slit masks with exaggerated vertical and horizontal size for clarity.

defines the circular beam delivered to ViSP. We note that the FIDO configuration for maximum power to ViSP delivers a 61-W beam to the ViSP slit station. Figure 39(b) shows a side looking view on the reflective side of the slit mask. The air force resolution target is deployed at Gregorian Focus. The thin vertical stripes seen decentered on the right side of the illuminated region are the slits etched into the aluminum coating. Figure 39(a) shows a drawing of the slit masks with great exaggeration in sizes. Slit widths range from 17 to 133 μm .

5.3 IOI Coatings: FIDO C-M1, ViSP Fold Mirrors, DKIST M9, and NCSP Folds

For this ViSP coating model, the FIDO mirror used at station CL2 provides the maximal throughput and spectrally smoothest polarization. The IOI coating EAgl-420 run number 6-7766 coats the FIDO C-M1. The same coating formula from IOI run 6-8065 coats the NCSP light weighted elliptical pickoff at AOI = 45 deg. Figure 40(a) shows retardance and diattenuation derived from Woollam ellipsometry on these two very similar coating runs.

The ViSP fold mirror 1 is coated with IOI formula EAgl-420 in run 6-7879. This mirror reflects at an incidence angle of 28 deg. The same coating formula with run 9-3095 was deposited on DKIST M9 folding at 10 deg incidence. Figure 40(b) shows retardance on top and diattenuation on bottom.

An IOI coating formula EAgl-420 run 6-7767 was deposited on ViSP feed mirror 2 reflecting at an incidence angle of 12.3 deg. This retardance is small but not zero. An IOI run 6-8410 coats the NCSP fold mirror 1 spare light weighted elliptical pickoff folding at an incidence angle of 45 deg. Figure 40(c) shows retardance on top and the diattenuation on bottom. The second run of this coating has a shorter zero-retardance wavelength and a generally higher diattenuation peak at 650 nm wavelength seen by comparing the dashed lines to the solid lines.

This particular coating recipe was chosen to ensure high reflectivity for spectral lines around 393 nm in addition to longer wavelengths. Figure 41(a) shows the reflectivity for several shots of this IOI coating at 60-deg incidence angle. There is mild variation in the exact wavelength of the reflectivity dip between 650 and 750 nm wavelength. The dashed blue line shows a slightly different formula for reference that does not exhibit the 2% drop at red wavelengths, but the 393 nm performance is near 88% instead of the goal >95%. The incidence angle behavior of reflectivity is mild from 15 deg to 60 deg. Figure 41(b) shows the unpolarized reflectivity for two particular coatings representing two substantially different coating layer thicknesses.

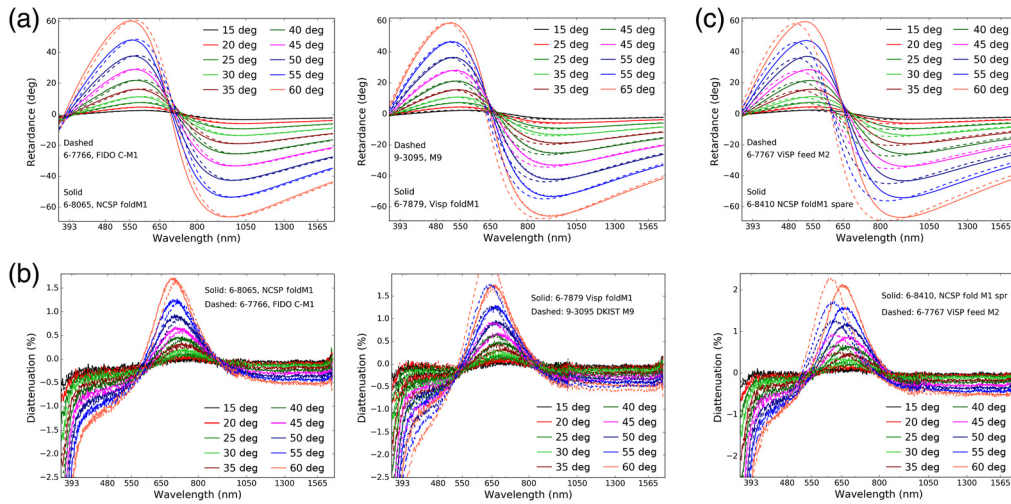


Fig. 40 The Woollam ellipsometry for the similar IOI coatings. (a) Retardance over incidence angles from 15 deg to 60 deg in steps of 5 deg. The left two graphics show two similar coatings on DKIST FIDO C-M1 reflecting at 15 deg incidence and the NCSP fold mirror 1 reflecting at 45 deg incidence. The middle two graphics show the DKIST M9 reflecting at 10 deg incidence and ViSP fold mirror 1 reflecting at AOI = 28 deg. The right two graphics show the ViSP feed M2 reflecting at 47.7 deg and a spare NCSP fold mirror working at 45 deg incidence.

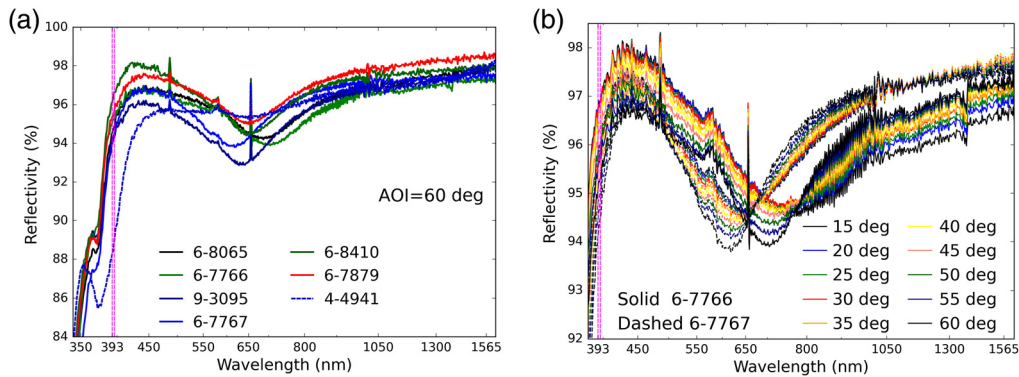


Fig. 41 The unpolarized reflectivity for several IOI EAg1-420 coating runs. (a) Several different coating runs deposited on optics used within DKIST. We show a 60-deg incidence angle. The dashed blue line shows a slightly different formulation (EAg1-450) that has reduced performance at 393 nm but better performance near 700 nm. (b) The reflectivity over the full incidence angle range for two selected coating runs with mildly different coating layer thicknesses.

6 Appendix B. Coating versus Substrate Spatial Variation

Coating uniformity specifications can vary widely depending on the process and equipment used by vendors. Coating formulas themselves can be designed to have lower sensitivity to layer thickness nonuniformities. We show in this appendix examples of protected metal coating variation as well as dichroic spatial variation through both the coating and the substrate properties.

6.1 Spatial Variation of Protected Metal Coatings: UH PanStarrs

Protected and/or enhanced metal coatings show spatial variation in performance similar to our FIDO dichroics. We reported in Ref. 86 variations detected between multiple different coating runs but also within a single coating using multiple witness samples distributed throughout the coating chamber. We show in this section some typical spatial variation of metal coatings using

ellipsometric data we funded at J.A. Woollam, as well as data contributed from the University of Hawaii PanStarrs telescope project (UH PS).

6.1.1 Protected aluminum coatings

The secondary mirror for the first PanStarrs (PS) telescope was recoated in June, 2021. An enhanced aluminum coating from EMF was selected as the same coating on other PS mirrors proved durable in Haleakala summit conditions. This mirror has a 900-mm diameter aperture with a hole through the center. EMF distributed five samples around the inner hole diameter as well as another three samples around the outer diameter (OD). We received four of the five inner samples and two of the three outer samples. Figure 42 shows the EMF enhanced aluminum coating properties as measured with Woollam ellipsometry around August, 2021. The incidence angle dependence in Fig. 42(a) shows mild unpolarized reflectivity sensitivity. Figure 42(b) shows the outer samples are significantly different in spectral dependence from the inner samples. This variation is well within the 15% uniformity of reflection specification for this mirror. Figures 42(c) and 42(d) show diattenuation and retardance, respectively. We only graph sample positions 1 and 6 as examples of the two maximally different coating samples.

We note that this kind of spatial uniformity was typical of prior EMF coatings for UH PS. Figure 43 shows a 2013 coating for the primary mirror on PS1 telescope (PS1 M1). A similar coating sample arrangement was followed. Coating spatial variation was detected across the aperture but the uniformity was well below the 15% specification at all wavelengths in the PS bandpass, with reflectivity variations only above 10% at ultraviolet wavelengths.

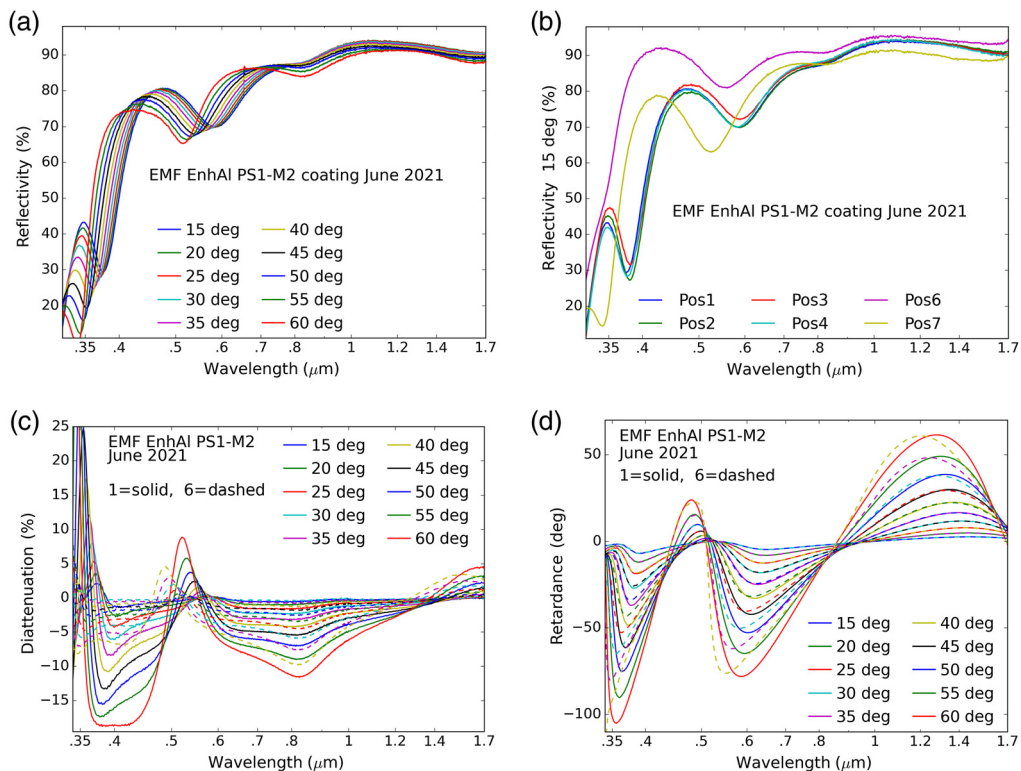


Fig. 42 Example ellipsometric data from the UH PanStarrs enhanced aluminum coating deposited on the first telescope’s secondary mirror (PS1, M2). Samples 1 to 5 were positioned within the inner mirror hole near the center of the aperture. Samples 6 to 8 were positioned around the OD of the 900 mm aperture mirror. Positions 1 to 4 as well as 6 and 7 were measured by Woollam. (a) The reflectivity changing with incidence angle for position 1. Other positions are similar. (b) The spatial variation of reflectivity between all samples at 15 deg incidence. (c) Diattenuation for position 1 as solid lines and position 6 as dashed lines. (d) Retardance. We note that polarization properties for samples 1 to 4 were nearly identical.

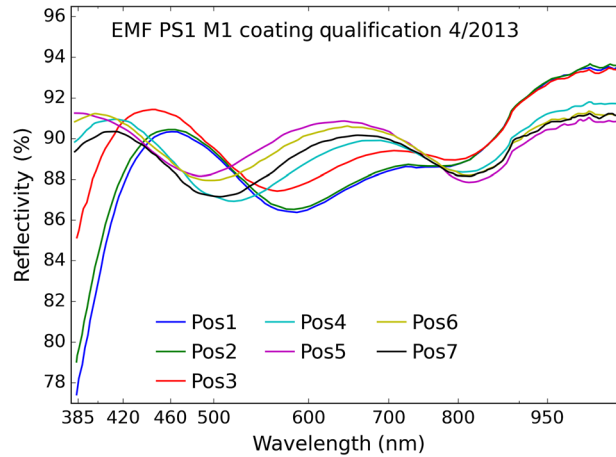


Fig. 43 The reflectivity of witness samples in the EMF protected aluminum coating on the UH PanStarrs telescope primary mirror (PS1 M1) from a 2013 run. Each color shows a different spatial location throughout the chamber.

6.1.2 Protected silver coatings

There are multiple optics that had been coated by the PS project with protected silver coatings. Vendors EMF and H. L. Clausing had performed coatings on at least two PS optics where metrology results were sufficient to assess spatial variation of coatings. Figure 44 shows spatial variation of two silver coatings within the UH PanStarrs system. Figure 44(a) shows an EMF protected silver coating deposited on the PS2 primary mirror (M1). PS2 M1 reflects roughly 95% at wavelengths beyond 500 nm with the typical blue performance degradation of silver coatings. Reflectivity drops below 80% reflectivity short of 400 nm. Figure 44(b) shows the H. L. Clausing coating protected silver coating deposited on the 900-mm diameter PS second telescope secondary (PS2 M2). The H. L. Clausing report contains aperture positions for the samples as within 1 to 3 in. of the inner diameter (ID) and OD of the secondary. The two samples placed inside the inner mirror hole are shown in black. Blue shows the OD samples. There is a 7% reflectivity difference at 400 nm wavelength between the inner and outer samples. There is much better agreement in the metrology for the two samples placed at similar distances from the optic center.

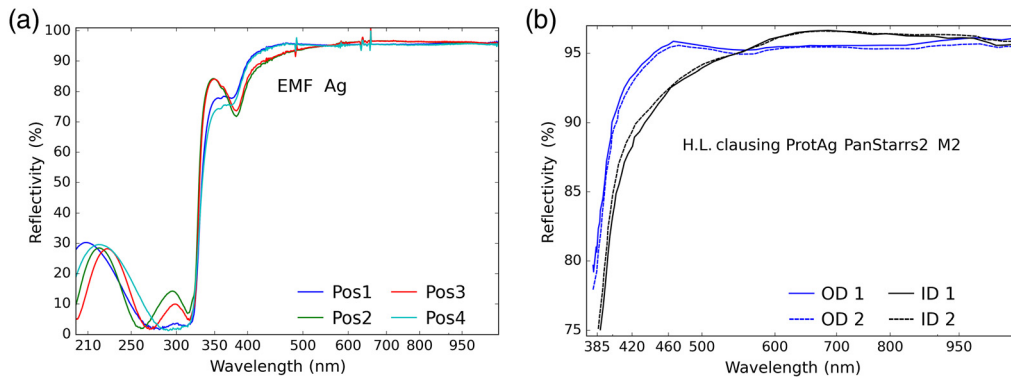


Fig. 44 The spatial variation of protected silver coatings used in PanStarrs. (a) An EMF silver coating at four positions throughout the chamber. (b) An H. L. Clausing coating on the second PS telescope secondary mirror (PS2 M2). Curves within the ID inside the inner aperture hole are denoted ID. Samples mounted around the outside of the 900-mm aperture mirror are denoted OD.

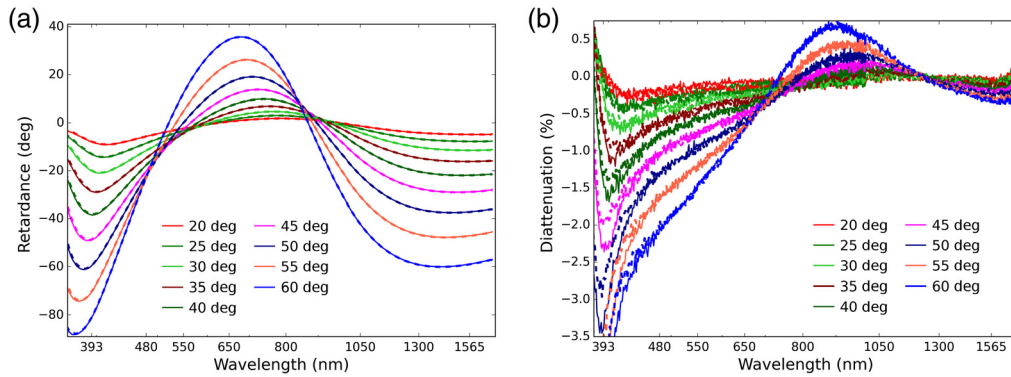


Fig. 45 The ellipsometry from Woollam for samples in coating runs for M9a as solid lines and DL-FM1 as dashed lines. (a) Retardance and (b) the diattenuation. Each color shows a different incidence angle. The two coatings are very similar.

6.2 Spatial Variation of Protected Metal Coatings: DKIST M9a and DL-FM1

Zygo was the vendor chosen to coat a longer wavelength optimized protected silver coating on mirrors feeding infrared instruments. The removable M9a pick-off flat feeding CN at AOI = 9 deg was coated as well as the first fold for DL-NIRSP at AOI = 45 deg called DL-FM1. Figures 45(a) and 45(b) show ellipsometric data from Woollam with retardance and diattenuation, respectively.

As part of qualifying the coatings, Zygo provided samples measured at ± 205 and ± 95 mm as well as at chamber center to cover an aperture of over 400 mm. Figures 46(a) and 46(b) show retardance and diattenuation for the uniformity qualification run, respectively. We only show an incidence angle of 45 deg to match DL-FM1 and note that the 9 deg incidence on M9a would see substantially lower polarization. We include the differences between measurements as the magenta curves about zero. The retardance difference curves are multiplied by five to highlight the differences. The PV retardance differences are < 1 deg over a 405-mm aperture. The diattenuation differences were not significant compared with the noise floor for all but the shortest wavelengths. At 393 nm, there is 1% PV nonuniformity in diattenuation, but these mirrors do not feed instruments working at wavelengths shorter than 500 nm (DL). We note that the reflectance uniformity was also better than 1% for all measurements, likely limited by systematic errors, with very little wavelength dependence.

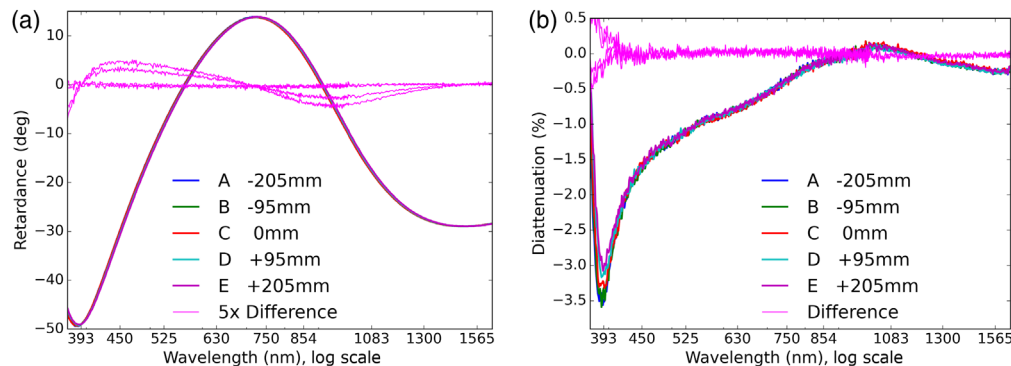


Fig. 46 The spatial variation estimated for the Zygo coating on DKIST M9a and DL-FM1 using the uniformity jig with five samples labeled A, B, C, D, and E covering a 410-mm-diameter aperture. We compute the difference between uniformity samples measured using the Woollam ellipsometry at an incidence angle of 45 deg. (a) The retardance and (b) diattenuation. The magenta curves show the difference between the uniformity sample measurements multiplied by five to highlight the small differences between spectra.

6.3 Spatial Variation of Protected Metal Coatings: DKIST M2, M4, M10

The DKIST nominal enhanced protected silver coating deposited on multiple mirrors show measurable retardance differences between multiple samples from the same coating shot. As examples, we had ellipsometric measurements done on multiple samples from DKIST M2, M4, and M10. For M10, we had four samples with chamber positions 4, 9, 12, and unknown with a clear aperture of 220 mm. For M2, we had samples labeled for positions A and M with the optic having a clear aperture of 620 mm. For M4, we had samples from positions 3 and 4 with the optic having a 450-mm clear aperture.

DKIST M2 and M10 have very similar incidence angle behavior. Figures 47(a) and 47(b) show retardance and diattenuation, respectively, derived from the Woollam ellipsometry over incidence angles from 15 deg to 60 deg. The coating diattenuation is <1% for all but the shortest wavelengths (see also Fig. 47 of Ref. 86).

We do not have information from the vendor about which spatial positions these labels may correspond to within the coating chamber as mounted for our particular mirror coating shots. We do detect small variation in all cases. Commonly samples are placed either around the OD of the mirror or often in a uniformity jig on an adjacent planetary system for smaller mirrors. Figures 48(a) and 48(b) show retardance differences and diattenuation differences, respectively. The DKIST nominal silver coating has maximal retardance near 650 and 1300 nm as detailed in Fig. 29 of Ref. 86. The coating retardance has the strongest spectral gradients near 390 and 850 nm where the retardance spectra cross through zero retardance. These correspond to the largest retardance spatial nonuniformities detected of up to 2 deg in Fig. 48(a). The diattenuation spatial variation is below 0.2% for all wavelengths beyond 393 nm in Fig. 48(b).

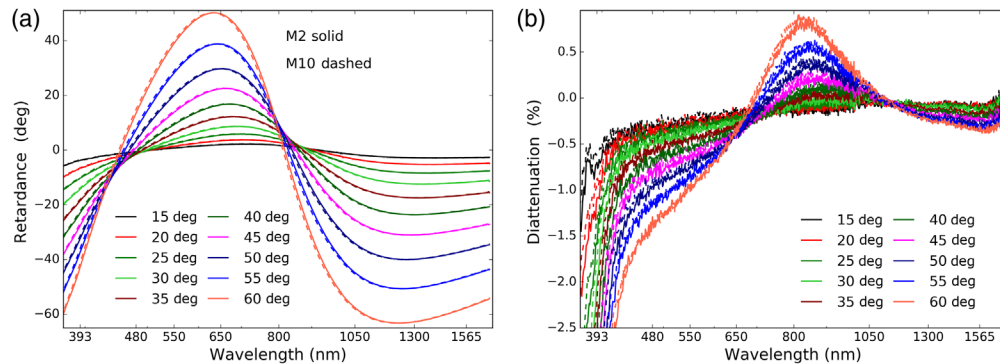


Fig. 47 (a) The retardance and (b) the diattenuation for the DKIST M2 and M10 coating witness sample ellipsometry. The solid lines show M2 while the dashed lines show M10. These two coating runs are very similar.

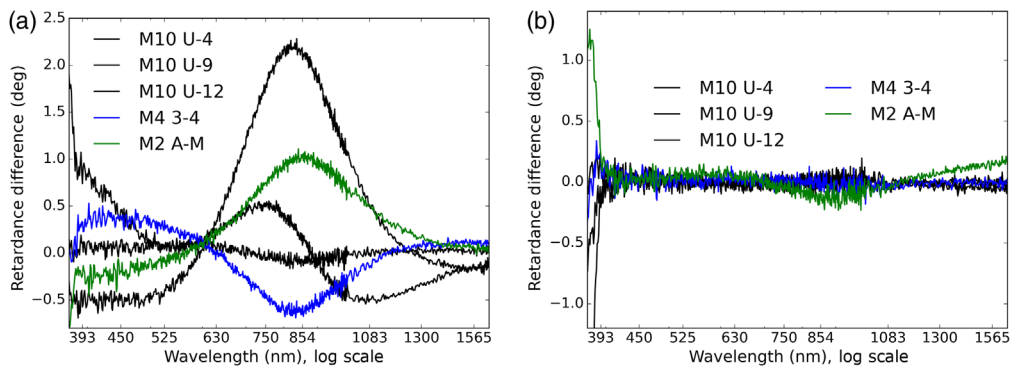


Fig. 48 (a) The retardance differences between multiple repeated samples. We subtract M10 samples 4, 9, and 12 from the Unknown (U) sample as the three black curves. The two samples for M2 and M4 are differenced and shown as green and blue curves, respectively. (b) The diattenuation differences between multiple repeated samples computed the same way.

6.3.1 Ellipsometry for DKIST M8: EMF-coated enhanced protected silver

The DKIST M8 mirror is coated with an EMF blue optimized enhanced protected silver coating formula AG-99. Figures 49(a) and 49(b) show retardance and diattenuation, respectively, derived from Woollam ellipsometry on the DKIST M8 witness samples. We include this coating here as it is an alternate formula for potential future recoating of DKIST system mirrors and already likely coats a few DL-NIRSP instrument mirrors.

6.4 Spatial Variation of Bare Metal Coatings: DKIST M1

DKIST M1 is bare aluminum coated at the AFRL. The full sized commissioning blank was coated initially as a test. The science mirror was coated in 2017 and used on the telescope until September, 2020. The science mirror was recoated in October, 2020. The bare aluminum coating used on DKIST M1 is much more uniform in reflectivity.

The natural aluminum oxide layer is expected to be in the range of 3 to 5 nm and forms within hours of coating.⁹⁸ We note that the conformal Al_2O_3 coating protecting our calibration polarizers from Moxtek presented in Ref. 88 is nominally 3.8 nm thick. We also show polarization fits to DKIST primary mirror (M1) in Appendix C, Fig. 68 of Ref. 86. We have interferometric testing of larger samples distributed throughout the chamber during the initial coating shown in Fig. 50(b). The samples show that the coating was physically between 90 and 150 nm thick across the 4-m aperture. We compare the 2018 and 2020 coating thicknesses in Table 9.

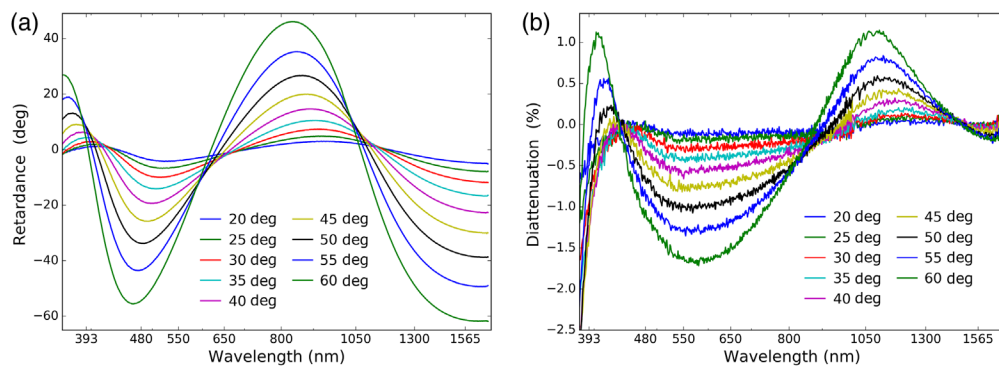


Fig. 49 The Woollam ellipsometry for DKIST M8 coating sample. (a) The retardance and (b) the diattenuation at a range of incidence angles.

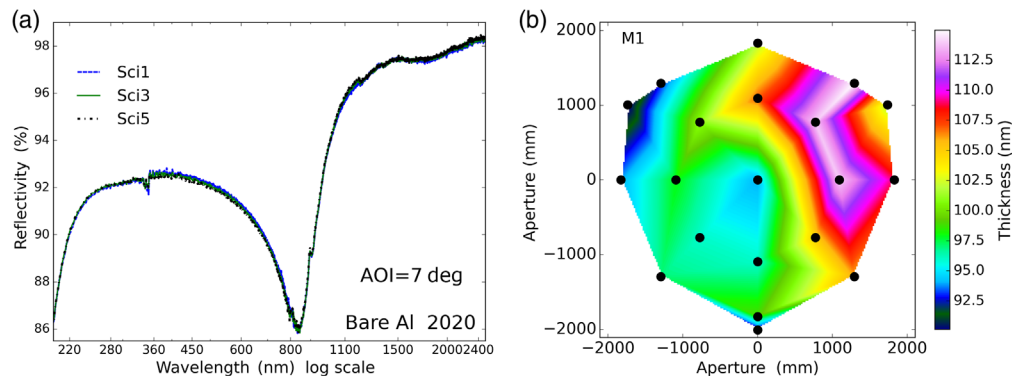


Fig. 50 (a) The reflectivity of the bare aluminum coating at three spatial locations just outside the DKIST M1 optic diameter. Minimal variation is detectable in this September 2020 coating. (b) The measured aluminum coating thickness in nanometers on multiple witness samples distributed across the 4 m aperture in the coating chamber during a 2018 coating run. Dots show the spatial location of the samples throughout the 4 m chamber. Measurements were interpolated onto a fine mesh grid covering the 4m aperture. Some of the aperture edge areas are not covered by interpolation. Similar behavior was seen in 2020.

Table 9 M1 thickness.

Pos	2020	2018
A	97.4	90.3
B	107.7	117.7
C	107.5	124.3
D	103.0	107.7
E	81.1	94.0
F	80.4	93.7

The reflectivity is spatially uniform as measured by three samples distributed in the chamber with the DKIST mirror substrate just outside the 4-m aperture.

The spatial variation of reflectivity in this 2020 coating is undetectable within measurements limits, somewhat better than Ref. 86; Sec. C.11, Fig. 67. We found in Ref. 86 a coating model of 2.5-nm Al_2O_3 over 50-nm aluminum when using TFCalc provided default aluminum metal refractive indices and 45-deg incidence polarimetric data. We found the same 2.5 nm of aluminum oxide but a thinner 40-nm metal layer when using an internal NSO aluminum metal interpolation. Both of the aluminum metal layer thickness fits are a factor of 2 too small compared with the direct thickness measurements on witness samples included in the chamber shown in Fig. 50.

A recent study on polarization aberrations and the impact on the Habex system by Breckenridge et al.⁹⁰ shows spatial variation in the retardance in reflection for a 3.75-m-diameter mirror coated at the University of Arizona in Fig. 19.⁹⁰ This form birefringence measurement at magnitudes of 0.002 radians retardance required a special setup developed, built, and measured by B. Daugherty.⁹⁰ The Breckenridge et al.⁹⁰ work shows spatial variation is present and measurable across large area mirrors. Given the factor of ~ 2 thickness variation in the DKIST aluminum coating, we certainly anticipate spatial variations in the mirror at some undetermined magnitude due to the varying properties of the aluminum across the mirror. Given the large incidence angle range for DKIST shown in Ref. 66, we also anticipate a fraction of a percent depolarization and some very mild elliptical retardance as second-order impacts from the $F/2$ DKIST M1. See Ref. 66 for examples of the depolarization calculations from a spatially variable AOI for DKIST coatings.

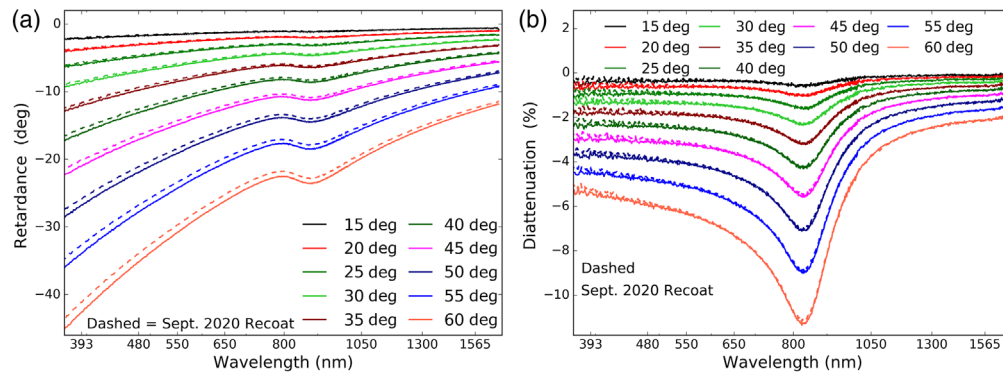


Fig. 51 (a) The retardance and (b) the diattenuation for the DKIST primary mirror (M1) bare aluminum witness samples included with the 4 m primary mirror in the coating chamber. Each color represents a different incidence angle from 15 deg to 60 deg in steps of 5 deg. The dashed lines show the September 2020 recoat samples while solid lines show the 2017 coating samples (both measured in late 2020).

Ellipsometry performed in late 2020 on witness samples from both the 2017 and 2020 DKIST aluminum coatings are shown in Fig. 51. Figure 51(a) shows the retardance and Fig. 51(b) shows the diattenuation.

7 Appendix C. DKIST Final Fido Coatings

We made an extensive example of the BS-950 performance in the main body text in Sec. 2.8. We show here the final as built performance of the other DKIST BSs and windows for use by the community for observation planning and awareness of spectral considerations during calibration. We highlight the retardance and diattenuation for both transmission and reflection. The narrow spectral features are present in the reflected beam of all DKIST dichroic coatings except for the BS-465. We also show the spatial uniformity of several dichroic coatings over 100 mm apertures. We cover the back-side antireflection coatings used on all the dichroics and windows. We also compare the spatial uniformity and narrow spectral features in both short-pass and long-pass type commercial dichroic mirrors from Thorlabs.

7.1 FIDO Dichroic Beam Splitter C-BS-465

This dichroic coating design and uniformity testing was already presented in Ref. 86. IOI has tested a design with 24 layers at 1.5- μm total thickness. The coating design has a strippable layer, 22 oscillating layers of SiO_2 and TiO_2 with a thicker SiO_2 outer layer. In Table 10, we show some coating tests done for the development of this coating. The first column shows the coating run name. The uniformity runs included the nine samples at 1-in. diameter. There were two runs using 4-in.-diameter parts to test coating stress. The full-sized optic substrate was subsequently tested before coating the final optic delivered to the summit. The back side antireflection coating is WBBAR1N formula.

7.1.1 BS-465 reflection and transmission from IOI

The final metrology for the as built BS-465 coated optic shows transmission and reflection in the appropriate design bandpasses easily above 95%. Figure 52 compares the IOI metrology for reflection and transmission of S and P polarization states. Figures 52(a) and 52(c) show the full metrology bandpass. Figures 52(c) and 52(d) highlight the transition wavelength.

7.1.2 BS-465 transmission spatial uniformity from NDSP3

These FIDO dichroic coatings have measurable spatial variation in transmission over relatively smaller apertures. As examples, we had included 4-in.-diameter fused silica substrates in preliminary coating stress testing from SN1, run 10-0265. With our Maui-based three spectrograph NDSP3 setup, we measured spatial maps of transmission variation in April, 2021. We used a rosettes spatial sampling with a 2-mm diameter collimated beam and 1.5-mm spatial steps

Table 10 BS-465 coating runs.

Optic	BS run	wbbar1n
Uniformity	10-0150	—
Uniformity	10-0153	—
Stress 4" SN07	10-0237	10-0230
Stress 4" SN01	10-0265	10-0248
Stress full	10-0339	10-0337
As-built	10-0374	10-0372

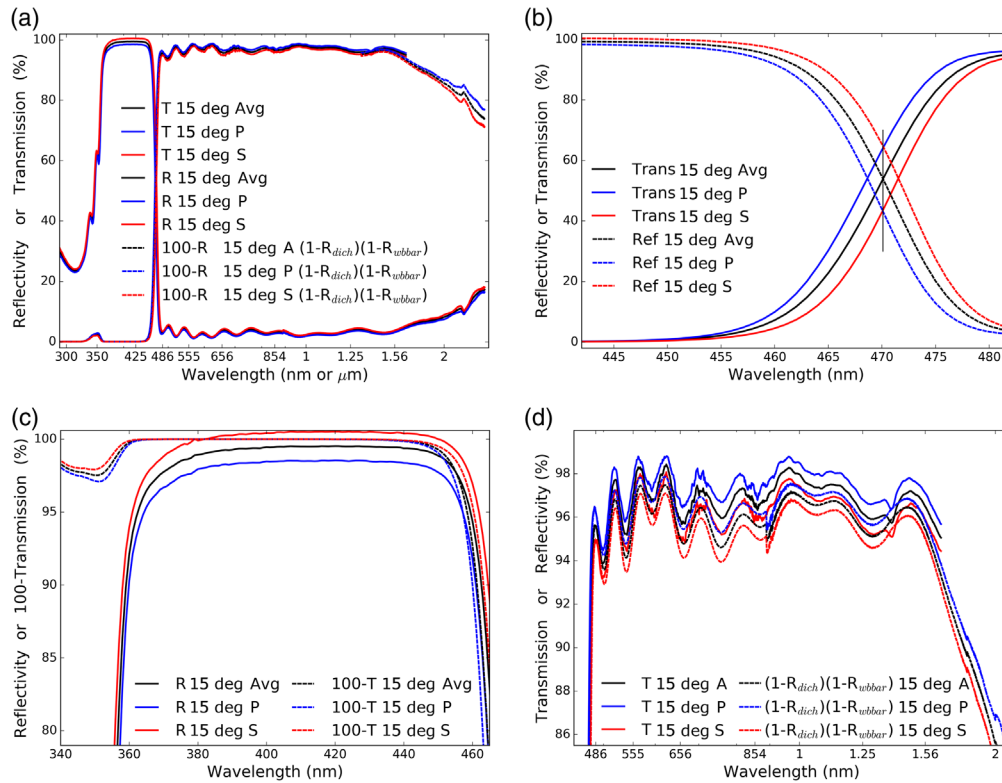


Fig. 52 The C-BS-465 final as built coating performance for run 10-0374. (a) The reflection and transmission spectra over the full 0.2 to 2.4 μm metrology bandpass. Red shows *S*, blue shows *P*, and black shows the average. (b) The transition bandpass where *S* and *P* polarization states transition from reflective to transmissive with a slight shift in wavelength. (c) The reflection bandpass with 1-transmission overplotted to show some mild short wavelength coating absorption. (d) The transmission bandpass with 1-reflectivity essentially mirroring transmission within metrology limits. Note that we compensated for the as-coated back surface antireflection coating when doing the 1-reflection calculation.

covering a 103-mm diameter aperture (see Fig 42. of Ref. 84 for example rosette sampling). Figures 53(a)–53(c) show example spatial maps of transmission at 521.7, 758.8, and 1680.5 nm, respectively. We note that a constant positive offset was applied to Fig. 53(a) (521.7 nm) to account for a misalignment impacting all wavelengths.

7.1.3 BS-465 retardance and diattenuation with NLSP in transmission: as built

The polarization properties in transmission are spectrally smooth for this relatively thin coating. Diattenuation is below 1% magnitude with retardance below 8 deg dropping with wavelength away from the 465 nm transition. Figure 54 shows the retardance and diattenuation in transmission for a range of low incidence angles. The repeated dashed lines show the nominal FIDO 15 deg incidence.

7.1.4 BS-465 retardance and diattenuation with NLSP in reflection: as built

The reflection band for the BS-465 coating is spectrally smooth in diattenuation and retardance, matching the design prediction. We measured one of the coating samples included with the dichroic run 10-0374. Figure 55 shows the retardance of the K-cell in the reflection band for the dichroic coating. We show ellipsometry for the bare aluminum mirrors in Appendix B.4, Fig. 51. We do not show diattenuation or reflectivity measured with this setup as there is good agreement with the IOI metrology, given the lack of narrow spectral features for this coating.

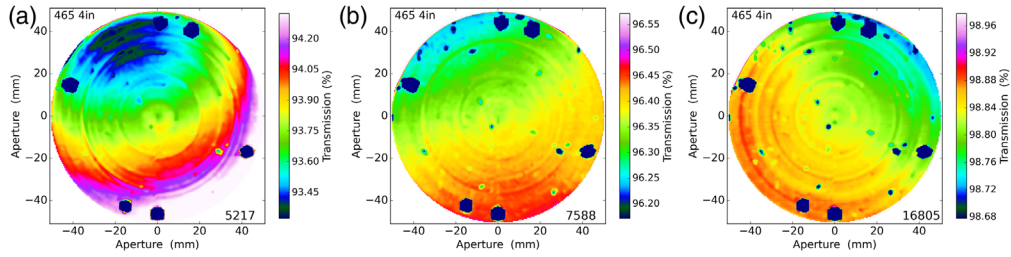


Fig. 53 The spatial variation of transmission over a 103-mm diameter aperture measured with NDSP3 for a preliminary coating stress test on the C-BS-465 dichroic formula (run number 10-0265 stress sample SN1). There are a series of square and circular dots on the outer edge of the aperture used to co-align the interferometric wavefront measurements that show up as nearly zero transmission. (a) 521.7 nm, (b) 758.8 nm, and (c) 1680.5 nm. The color scale has been set as the median of the transmission over the aperture with a scale of (a) $\pm 0.4\%$, (b) $\pm 0.16\%$, and (c) $\pm 0.07\%$. Note that the general form of the spatial variation is a strong function of wavelength.

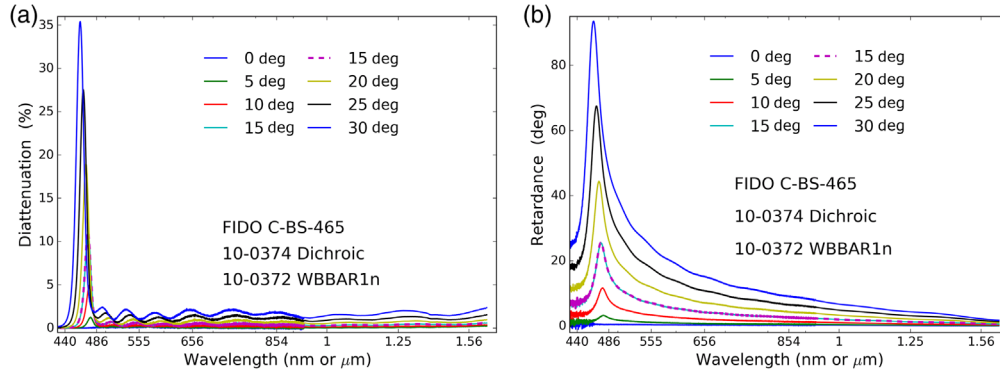


Fig. 54 The FIDO 465 coating data from coating run 10-0374 on the full sized part in transmission measured in our Boulder NLSP setup at 0.3 nm spectral resolving power (FWHM). (a) Diattenuation and (b) retardance. Each color shows a different incidence angle with the nominal 15 deg as the dashed line.

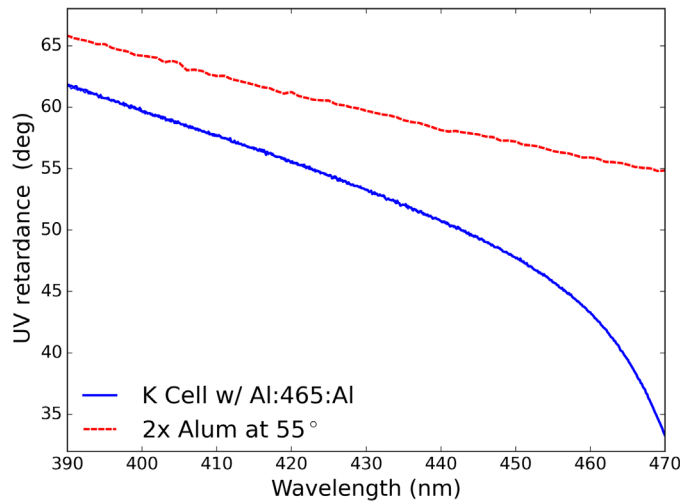


Fig. 55 The reflected beam retardance in an K-cell setup with two bare aluminum reflections near 55 deg incidence and the BS-465 coating witness sample at 15 deg incidence. We show ellipsometry of bare aluminum samples for reference.

7.2 FIDO Dichroic Beam Splitter C-BS-555

In Table 11, we show some coating tests done for the development of this coating. Preliminary testing of 48 and 64 layer designs did not give acceptable reflection band performance. The coating stress test involved the dichroic BS-555 coating formula for run 10-0241 with a back-side antireflection coating in run 10-0229 done in April, 2019. We note that the incorrect coating formula was deposited for run 10-0229 so we do not include this coating run in the complete testing. The run 10-0229 reflectivity was below 3% for wavelengths where the BS-555 coating reflects. There were somewhat inconsistent coating reflected wavefront power results leading the team to perform an additional coating test in run 10-0296. The coating was successful. However, the glass substrate had not been MRF subaperture finished leading to larger TWE than specified. This part was stripped and recoated again to achieve the final as-built coating runs in 10-0362 for the dichroic and 10-0360 for the antireflection coating.

7.2.1 BS-555 reflection and transmission from IOI

Figure 56 compares the IOI metrology for reflection and transmission of *S* and *P* polarization states. Figure 56(a) shows the full performance bandpass. Figure 56(b) shows reflectivity compared to 1-transmission to identify coating absorption bands. There is effectively no detectable transmission through the coating in the 380 to 540 nm bandpass. Reflection losses of 1% to 2% are seen across the bandpass with some 2% additional absorption spectral features near 410 nm and in the 450 to 500 nm wavelength range. The diattenuation is mostly constant with wavelength as seen by the constant difference between *S* and *P* curves (red versus blue).

Table 11 BS-555 coating runs.

Optic	BS run	WBBAR1n
Stress 555	10-0241	10-0229
C-BS-555t	10-0296	10-0292
C-BS-555	10-0362	10-0360

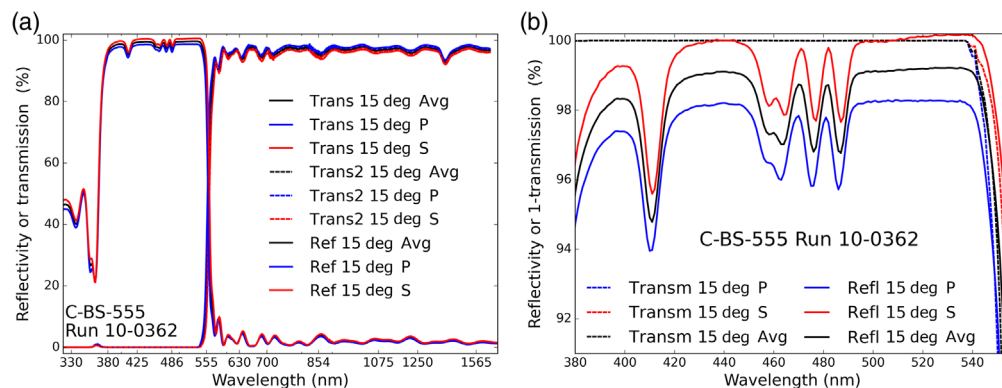


Fig. 56 The C-BS-555 final as built coating performance for run 10-0362. (a) The reflection and transmission spectra over the full 0.2 to 2.4 μm metrology bandpass. Red shows *S*, blue shows *P*, and black shows the average. A repeated polarized transmission data set is shown as dashed lines. (b) The reflection and 1-transmission curves in the reflection bandpass to highlight coating absorption spectral features.

7.2.2 BS-555 transmission spatial uniformity from NDSP3

These FIDO dichroic coatings have measurable spatial variation in transmission over relatively smaller apertures. As examples, we had included 4-in.-diameter fused silica substrates in preliminary coating stress testing from SN9, run 10-0241. With our Maui-based three spectrograph NDSP3 setup, we measured spatial maps of transmission variation in April, 2021. We used a rosettes spatial sampling with a 2-mm diameter collimated beam and 1.5 mm spatial steps covering a 103-mm diameter aperture (see Fig. 42 of Ref. 84 for example rosette sampling). Figures 57(a)–57(c) show example spatial maps of transmission at 594.3, 705.9, and 1566 nm, respectively.

7.2.3 BS-555 retardance and diattenuation with NLSP in transmission

The final as-built C-BS-555 has very low diattenuation and spectrally smooth retardance in transmission. Figure 58 shows the retardance and diattenuation in transmission for a range of incidence angles measured in NLSP. Thick blue lines show the nominal DKIST FIDO 15 deg incidence angle measurements.

7.2.4 BS-555 retardance and diattenuation in reflection with NLSP K-cell

The BS-555 dichroic coating has a band with three narrow spectral features. Figure 59 shows the polarization and intensity measured with our NLSP setup in the Boulder labs in early 2021.

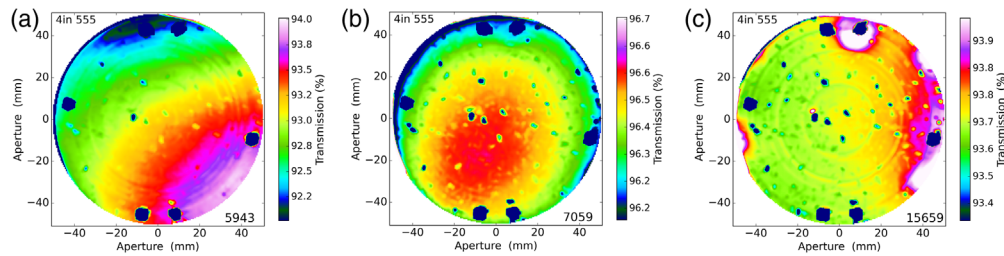


Fig. 57 The spatial variation of transmission over a 103-mm diameter aperture measured with NDSP3 for a preliminary coating stress test on the C-BS-555 dichroic formula (run number 10-0241 stress sample SN9). There are a series of square and circular dots on the outer edge of the aperture used to coalign the interferometric wavefront measurements that show up as nearly zero transmission. (a) 594.3 nm, (b) 705.9 nm, and (c) 1565.9 nm. The color scale has been set as the median of the transmission over the aperture with a scale of (a) $\pm 1\%$, (b), (c) $\pm 0.3\%$. Note that the general form of the spatial variation is a strong function of wavelength.

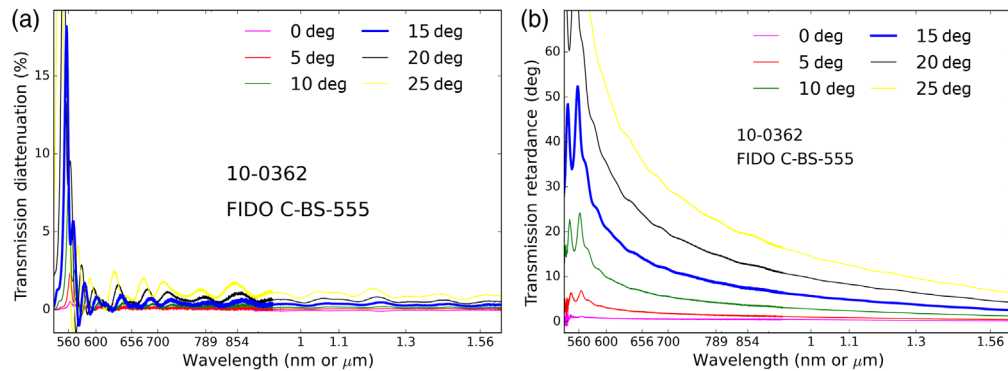


Fig. 58 The FIDO BS-555 as built polarization metrology from coating run 10-0362 on the full sized part in transmission measured with NLSP in February, 2020. (a) The diattenuation. (b) The retardance. A range of incidence angles is covered about the nominal 15 deg shown as the thicker blue line.

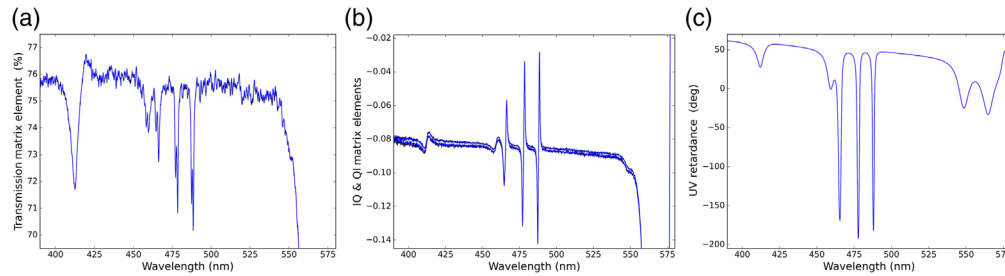


Fig. 59 (a) The intensity, (b) diattenuation, and (c) retardance in reflection for the final delivered C-BS-555 coating. Our NLSP system measured coating witness sample at 15 deg incidence angle from run 10-0362 in a K-cell type test setup. Most of the throughput loss can be attributed to the bare aluminum mirrors at the two high incidence stations in the K-cell. The narrow spectral features are attributable to the dichroic coating.

Two bare aluminum coated mirrors were used at roughly 50 deg incidence while the BS-555 witness sample was mounted at 15 deg. The reflectivity is shown in Fig. 59(a), diattenuation in Fig. 59(b), and retardance in Fig. 59(c). There are a few features representing roughly 5% throughput losses. The cluster of diattenuation features at $\pm 6\%$ magnitude also correlate with retardance features at ± 300 deg magnitudes.

In Fig. 60, we highlight a 16-nm spectral window between 475 and 491 nm encompassing the two largest features using the same data set on the final BS-555 dichroic coating from run 10-0362. Reflectivity shown in Fig. 60(a), diattenuation in Fig. 60(b), and retardance in Fig. 60(c). The H_β line observed with ViSP is at 486.2 nm on the wing of one spectral feature.

7.2.5 BS-555 modeling retardance and diattenuation narrow features

The narrow spectral features in diattenuation and retardance vary substantially with coating shot. Figure 61 shows the retardance and diattenuation in reflection in NLSP with a K-cell for the BS-555 coating done during stress testing nominally around 12 deg incidence angle. Black shows the NLSP data at 12 deg incidence. Blue shows the TFCalc design at 15 deg incidence. Dark blue shows the TFCalc design model at the 12-deg metrology incidence angle. The coating designs were created with targets to drive the diattenuation toward zero. However, manufacturing tolerances lead to narrow spectral features. The exact wavelength and magnitude of these features depends substantially on the coating model details.

7.3 FIDO Dichroic Beam Splitter C-BS-643

This BS was optimized to perform a particularly narrow transition from reflective to transmissive. The Fe I spectral line at 630.2 nm wavelength needs to be reflected efficiently and with benign polarization. The H_α line at 656 nm needs to be transmitted similarly with benign polarization properties. In Table 12, we show some coating runs done for the development and delivery

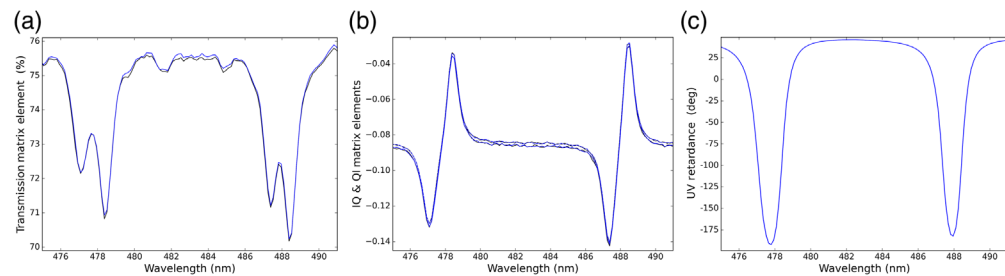


Fig. 60 (a) The intensity, (b) diattenuation, and (c) retardance in reflection for the final delivered C-BS-555 coating in a narrow 16 nm bandpass. Our NLSP system measured coating witness sample at 15 deg incidence angle from run 10-0362 in a K-cell type test setup.

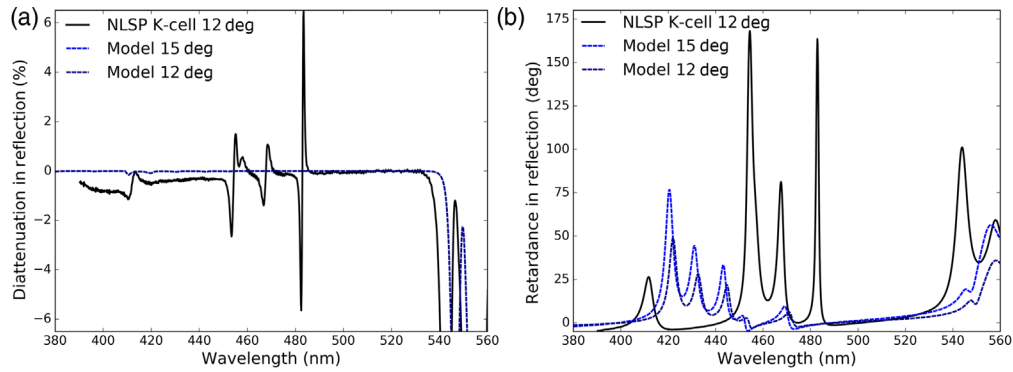


Fig. 61 The FIDO BS-555 coating data from stress test coating run 10-0296 on the full sized part. The BS-555 coating is measured in reflection using a K-cell in NLSP. (a) The diattenuation and (b) the retardance. Both have had the two high incidence mirror polarization properties subtracted to isolate the BS-555 coating performance.

Table 12 C-BS-643 coatings.

Optic	BS run	WBBAR2
Design 643	10-0280	10-0278
Stress 643	10-0367	10-0337
C-BS-643	10-0482	10-0481

of this optic. Coating run 10-0280 was the design verification testing of the FIDO 643 dichroic. The full sized stress test optic was coated in run 10-0367. The final coating run 10-0482 was done in spring 2021. The WBBAR2 formula was coated on the back side of all dichroics.

7.3.1 BS-643 reflection and transmission from IOI

The BS has a mild spectral ripple in the transition bandpass but the coating does marginally achieve the >80% transmission at 656.3 nm requirement. The 630.2-nm reflection is nearly 100%. Figure 62 shows the metrology in reflection and transmission. Figure 62(a) shows the full metrology range. Figure 62(b) highlights the reflection bandpass comparing the reflectivity data to 1-transmission as a proxy for coating absorption. Figure 63 highlights the performance

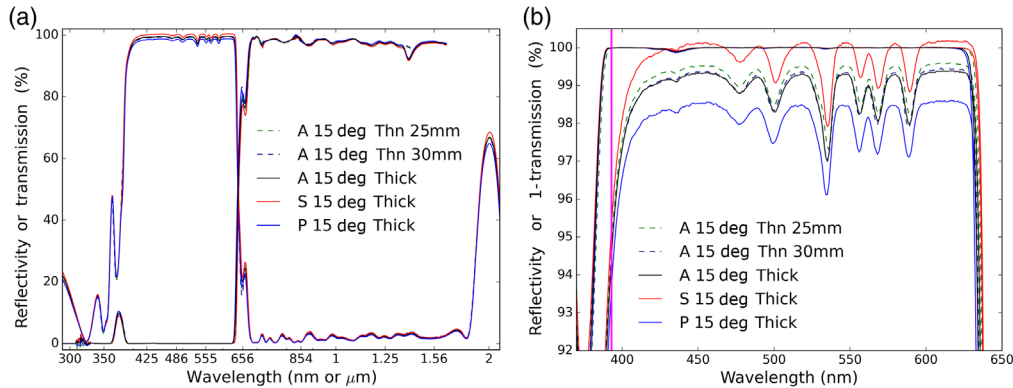


Fig. 62 Reflectivity and transmission data sets measured by IOI at 15-deg incidence on many samples. (a) The reflection and transmission data for *S* and *P* linear polarization states as well as the average (*A*). (b) The reflection band comparing the measured reflectance with 1-transmission. The difference is attributable to coating absorption.

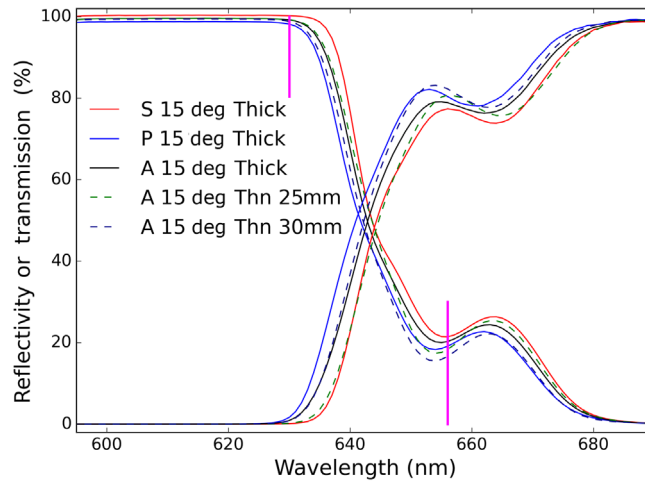


Fig. 63 The transmission and reflection data near the 643-nm transition wavelength highlighting the 630.2- and 656.3-nm key lines.

for the critical transition wavelength for the final coating on this dichroic coating. We highlight these two key scientific observing wavelengths with the vertical magenta lines. Multiple samples were tested. Samples with 5 mm thickness denoted as thick with solid lines. We had 1-mm thick samples at 25 and 30 mm diameter also tested with and without a thermal bake-out process applied. There is little change in performance with the substrate change and thermal process.

7.3.2 BS-643 retardance and diattenuation with NLSP in transmission

The diattenuation response is well below 1% in transmission for all wavelengths beyond the transition. Retardance decays smoothly with wavelength beyond the transition. Figure 64 shows the retardance and diattenuation in transmission for a range of low incidence angles on the final BS-643 coating run 10-0482. Thick blue shows the nominal DKIST FIDO 15 deg incidence.

7.3.3 BS-643 retardance and diattenuation in reflection with NLSP K-cell

The BS-643 dichroic coating has one major narrow spectral feature. Figure 65 shows the polarization and intensity measured with our NLSP setup in the Boulder labs in early 2021 at 0.3-nm spectral resolving power (FWHM). Two bare aluminum coated mirrors were used at roughly 50 deg incidence while the BS-643 witness sample was mounted at 15 deg. The reflectivity is shown in Fig. 65(a), diattenuation in Fig. 65(b), and retardance in Fig. 65(c). Most of the bandpass has high reflectivity with one single narrow feature near 531 nm wavelength.

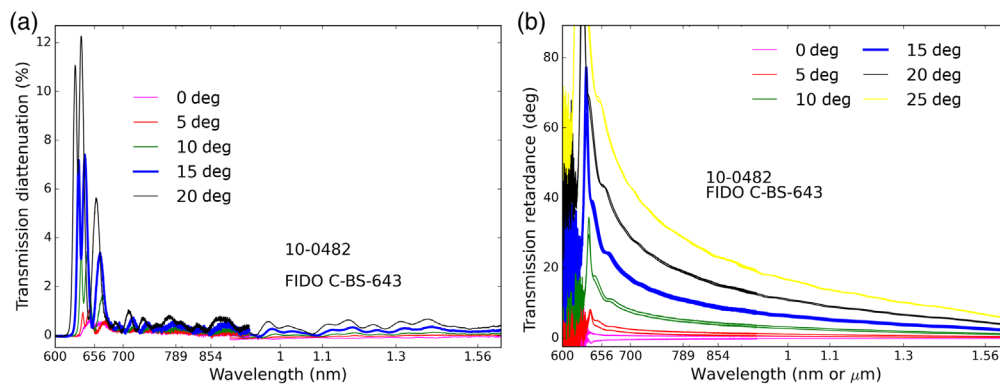


Fig. 64 The FIDO 643 coating polarization metrology data from the final as-built coating run 10-0482 on the full sized part in transmission. (a) The diattenuation and (b) the retardance. The nominal 15-deg incidence is shown as the thicker blue line.

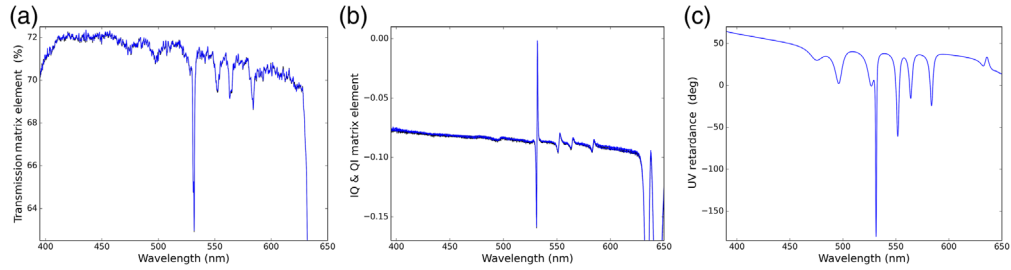


Fig. 65 (a) The intensity, (b) diattenuation, and (c) retardance in reflection for the final delivered C-BS-643 coating. Our NLSP system measured coating witness sample at 15-deg incidence angle from run 10-0482 in a K-cell type test setup.

Figure 66 shows the same data set on the final BS-643 dichroic coating from run 10-0482. For this figure, we highlight a 7-nm spectral window from 527.5 to 534.5 nm. Reflectivity is shown in Fig. 66(a), diattenuation in Fig. 66(b), and retardance in Fig. 66(c). The common Fe XIV line observed with ViSP is at 530.3 nm just on the wing of the spectral feature observed in these images. We note that our measurement of incidence angle in the metrology equipment is a manual process. A shift in wavelength for this narrow feature is well within our error margin.

7.3.4 BS-643 modeling retardance and diattenuation narrow features

The models have a difficult time predicting the exact wavelength and spectral character of these narrow spectral features. Figure 67 shows the retardance and diattenuation in reflection in NLSP with a K-cell nominally around 12-deg incidence angle. Black shows the NLSP data at 12-deg

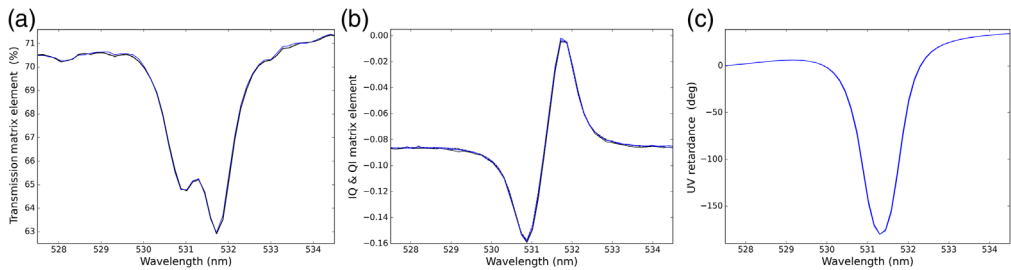


Fig. 66 (a) The intensity, (b) diattenuation, and (c) retardance in reflection for the final delivered C-BS-643 coating in a narrow 7 nm bandpass. Our NLSP system measured coating witness sample at 15 deg incidence angle from run 10-0482 in a K-cell type test setup.

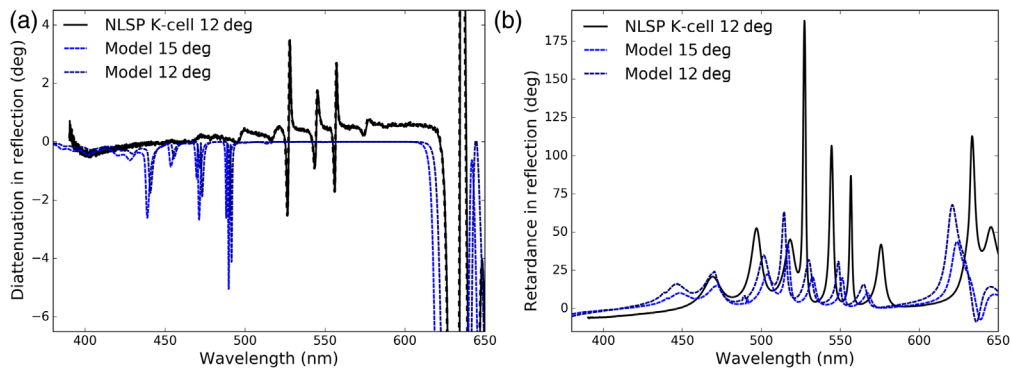


Fig. 67 The FIDO 643 coating data from coating run 10-0280 on the design test run in reflection in an NLSP K-cell. (a) The diattenuation and (b) the retardance. Both TFCalc models have small diattenuation spikes near 440 nm wavelength but the actual coating shows a cluster of spikes near 530 to 560 nm.

incidence. Blue shows the TFCalc design at 15-deg incidence. Dark blue shows the TFCalc design at 12-deg incidence. The wavelength and magnitude of the narrow features do not match well. A coating design sensitivity analysis did show sensitivity at the wavelengths presently modeled. The actual narrow spectral features are observed for diattenuation at roughly 50 nm longer wavelengths.

7.4 FIDO Dichroic Beam Splitter C-BS-680

IOI proposed and tested a design with 104 layers at 8.04- μm total thickness. The coating design has a strippable layer, 102 oscillating layers of SiO_2 and TiO_2 with a thick outer SiO_2 layer. A preliminary design verification run was shot in February, 2020. The full sized stress test coating was shot in March, 2020. The final as-built coating was shot in March, 2021. Table 13 shows the nominal coating runs. The WBBAR2 coating was put on the back surface of the full-sized parts.

7.4.1 BS-680 reflection and transmission from IOI full sized stress sample

This 104 layer design has substantially larger spectral and spectrally narrower oscillations in the transmission bandpass. Figure 68 compares the IOI metrology for reflection and transmission of S and P polarization states with some example metrology with our NLSP system. Figure 68(a) shows the full performance bandpass. Issues with the IOI metrology equipment during this particular fabrication led to an incomplete data set with missing spectra and other spectra collected on different equipment. Figure 68(b) shows the reflection spectra compared to 1-transmission as a proxy for coating absorption. There are two notable absorption bands roughly 8% deep near 480 and 525 nm.

There are only two spectrally sharp transmission spectral features that correlate with the coating absorption. We show the NLSP-derived transmission at 0 deg- and 15-deg incidence angles

Table 13 BS-680 runs.

Optic	BS run	WBBAR2
Design 680	10-0359	—
Stress 680	10-0370	10-0338
C-BS-680	10-0502	10-0500

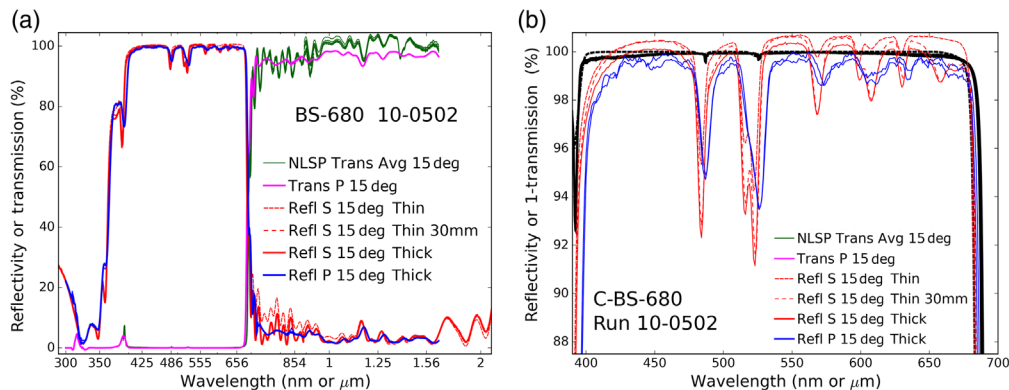


Fig. 68 The reflection and transmission for the final coated BS-680 dichroic run 10-0502. (a) The full inhomogeneous data set with multiple instruments measuring various samples. Our NLSP system with 0.3-nm FWHM clearly resolves spectral oscillations in transmission shown as the green curves. (b) The reflection as red and blue alongside 1-transmission in black. There is essentially no transmission through this coating in the reflection band. Differences correspond to coating spectral absorption features.

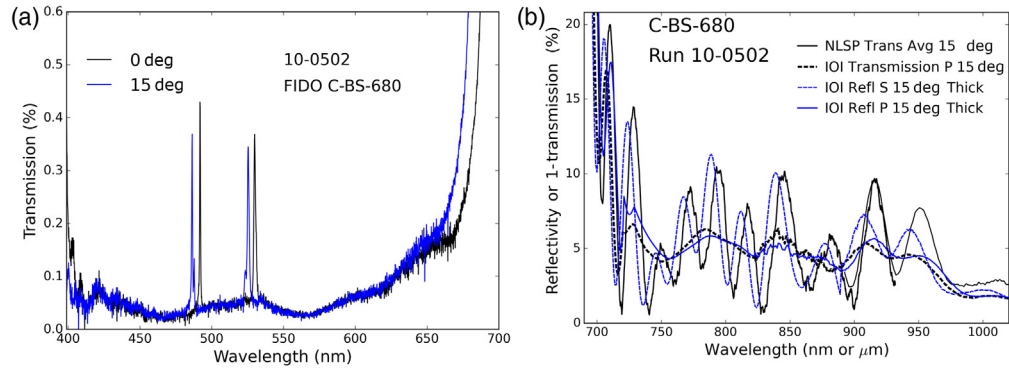


Fig. 69 (a) The narrow spectral features in transmission derived with the 0.3-nm FWHM configuration of NLSP with a coating witness sample at 0 deg (black) and 15 deg (blue) incidence angle. (b) The reflection and 1-transmission spectra for different metrology tools at different spectral resolving power. NLSP transmission measures large spectral oscillations (solid black) similar to the IOI S reflection measurement in dashed blue. The IOI P reflection (solid blue) and IOI P transmission (dashed black) are both at much lower spectral resolving power.

in Fig. 69(a). These two narrow spectral features have $<0.4\%$ transmission at the same wavelengths where 8% coating absorption is estimated.

Figure 69(b) shows example impacts of the metrology system spectral resolving power on the derived coating properties. In our NLSP measurements with 0.3-nm FWHM optical performance, we see spectral oscillations at 10% peak-to-peak magnitude in transmission. IOI measurements with lower spectral resolving power reduce these oscillations by at least a factor of 4. Diattenuation spectra derived with these different instruments would suffer from large errors.

7.4.2 BS-680 retardance and diattenuation with NLSP in transmission: as built

Figure 70 shows the retardance and diattenuation in transmission for a range of low incidence angles measured on multiple witness samples with our NLSP system. The thick blue lines shows the nominal DKIST FIDO 15-deg incidence.

7.4.3 BS-680 retardance and diattenuation in reflection with NLSP K-cell

The BS-680 dichroic coating has several narrow spectral bandpasses where the transmission can drop by more than 10%, the diattenuation can reach more than 20%, and the retardance can change by more than 250 deg over 1 nm wavelength. Figure 71 shows the polarization and intensity measured with our NLSP setup at 0.3-nm spectral resolving power (FWHM) in the Boulder labs in early 2021. The reflectivity is shown in Fig. 71(a), diattenuation in

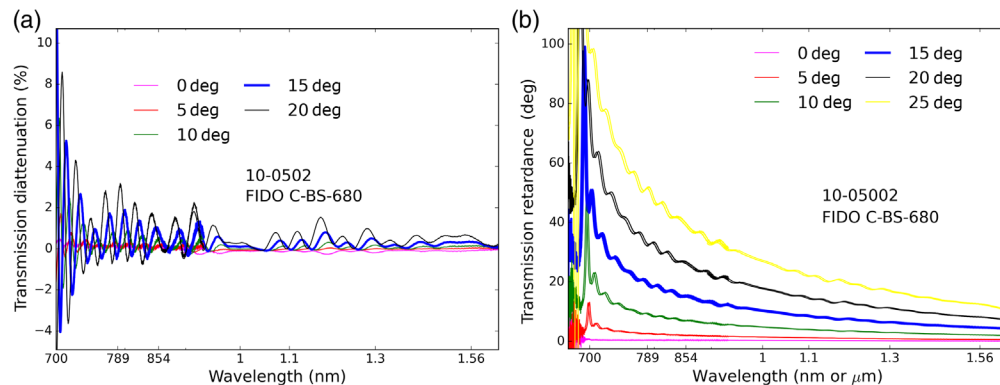


Fig. 70 The FIDO 680 coating polarization data from the final as built coating run 10-0502 measured with NLSP in transmission. (a) The diattenuation and (b) the retardance.

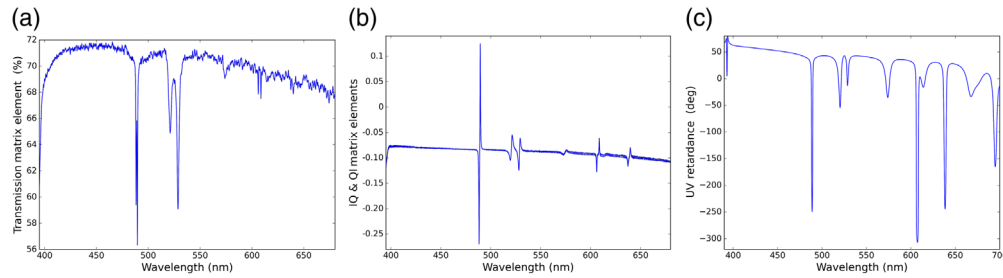


Fig. 71 (a) The intensity, (b) diattenuation, and (c) retardance in reflection for the final delivered C-BS-680 coating. Our NLSP system measured coating witness sample at 15-deg incidence angle from run 10-0502 in a K-cell type test setup.

Fig. 71(b), and retardance in Fig. 71(c). Two bare aluminum-coated mirrors were used at roughly 50-deg incidence while the BS-680 witness sample was mounted at 15 deg.

Figure 72 shows the same data set on the final BS-680 dichroic coating from run 10-0502 with reflectivity shown in Fig. 72(a), diattenuation in Fig. 72(b), and retardance in Fig. 72(c). In this figure, we highlight a 7-nm bandpass spectral window from 485.5 to 492.5 nm surrounding the worst spectral feature seen in this coating. The diattenuation is larger than $\pm 15\%$ with retardance varying close to 300 deg. The commonly observed H_{β} line at 486.2 nm is roughly 1.2 nm wavelength away from this spectral feature.

7.5 FIDO Dichroic Beam Splitter C-BS-950

We performed more than 13 coating runs during development of the C-BS-950 dichroic coating. Information gained from these coating tests informed the refractive index modeling of the TiO_2 and SiO_2 in the actual deposition conditions as well as the tolerancing.

7.5.1 BS-950 coating design and stress testing summary

Table 14 shows the coating runs done on the BS-950 dichroic design. Initially, a 97-layer design was proposed as shown in Ref. 86. Initial spectral uniformity testing was done in run 10-0168 using this design. After this and other testing, a design change was made to use 88 layers. Preliminary coating stress testing was performed with six separate coating shots using 4-in.-diameter samples as well as many individual witness samples in summer 2018. Subsequently, extracoating runs were performed in May and July, 2019. Full-sized BS substrates were used in the test in addition to 4-in.-diameter substrates and witness samples.

The coating shot 10-0193 had a strong and narrow transmission leak of roughly 30% seen in the Shimadzu 3101 reflectivity at 0-deg and 12-deg incidences on both Heraeus and IOI stock fused silica as well as the Lambda 1050 URA spectral system in reflection at 12-deg incidence.

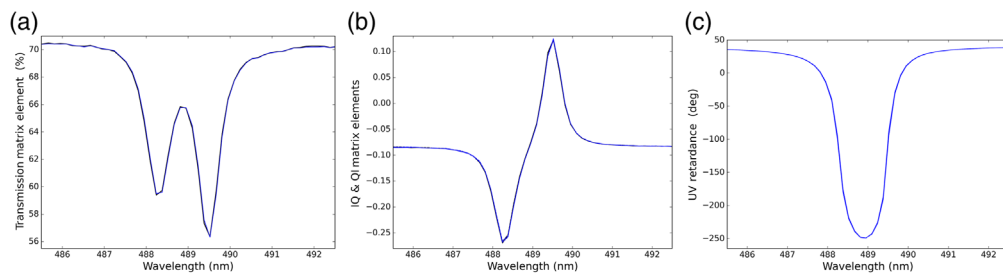


Fig. 72 (a) The intensity, (b) diattenuation, and (c) retardance in reflection for the final delivered C-BS-680 coating in a narrow 7-nm bandpass from 485.5 to 492.5 nm. Our NLSP system measured coating witness sample at 15-deg incidence angle from run 10-0502 in a K-cell type test setup.

Table 14 BS-950 coating runs.

Optic	Date	BS run	WBBAR2
Unif. 950 97lyr	July, 2018	10-0168	—
Design 950	July, 2018	10-0173	—
Stress 950 SN5	July, 2018	10-0174	10-0188
Stress 950 SN6	July, 2018	10-0175	10-0187
Stress 950 SN4	August, 2018	10-0178	10-0186
Stress 950 SN10	September, 2018	10-0193	10-0180
Stress 950 SN11	October, 2018	10-0194	10-0181
Stress 950 SN12	October, 2018	10-0195	10-0182
Stress 950	May, 2019	10-0274	10-0271
Stress 950	July, 2019	10-0287	10-0284
Stress 950	September, 2019	10-0304	10-0303
Final 950 fail	February, 2020	10-0364	10-346
Final 950	November, 2020	10-0475	10-0471

Figure 73 shows reflection and transmission spectra from all data sets provided by IOI during metrology. We note that for almost all spectra, the average polarization property was computed as the average of measurements from both *S* and *P* polarization states.

7.5.2 BS-950 final coating absorption

The C-BS-950 dichroic coating has several spectral absorption features at magnitudes of a few percent over features several nanometers wide. Figure 74 shows the difference between IOI reflection data and the 1-transmission data curves. We attribute absorption to the spectral features, given that there is undetectable transmission yet substantial reflection loss. These absorption features also correlate with the amplitude and phase effects seen in the narrow spectral features both in transmission and reflection.

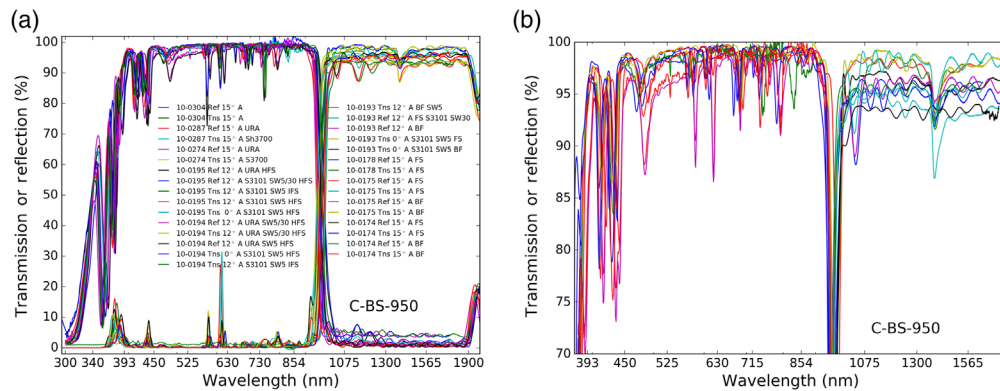


Fig. 73 Reflectivity and transmission measured by IOI at 0-deg and 12-deg incidences. (a) A wide wavelength and transmission range. (b) The nominal DKIST first light bandpass 380 to 1800 nm with coating runs 10-0195 and 10-0174 removed from the set.

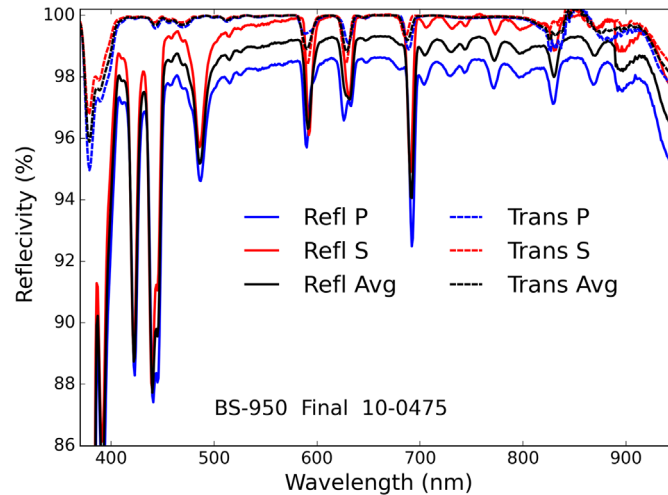


Fig. 74 Reflection and 1-transmission metrology from Infinite Optics at roughly 2-nm slit bandwidth for the C-BS-950 final coating run 10-0475. The solid lines show polarized reflection at the nominal DKIST incidence angle of 15 deg. The dashed lines show 1-transmission as an estimate for the combination of absorption and reflection. Blue shows the P linear polarization state. Red shows S . Black shows the average of the two for unpolarized reflection and transmission. There are several substantial spectral features showing reflection losses without a corresponding transmission feature making the spectral features attributable to coating absorption.

7.5.3 BS-950 retardance and diattenuation with NLSP in transmission: as built

Figure 75 shows the retardance and diattenuation in transmission for a range of low incidence angles. The thick blue lines shows the nominal DKIST FIDO 15 deg incidence.

7.5.4 BS-950 transmission spatial variation: 100 mm aperture and NDSP3

We easily detect spatial differences in transmission that are strong functions of wavelength. Dichroic coating designs are expected to have strong wavelength-dependent performance changes that are easily modeled during the coating design sensitivity phase. We collected a detailed spatial mapping data set for transmission on a BS-950 dichroic coating stress sample SN4 in spring of 2021. Spatial sampling used a rosette pattern with 1.0 mm spatial steps and a beam with a 1.5-mm-diameter optical beam. Our NDSP3 system recorded 7651 spectra per map with five repeated maps for 38,255 total spectra recorded using each of the three spectrographs. Figure 76 shows example transmission spectra. The blue and red bandpass spectrographs have had the measured transmission multiplied by 10 \times to make the spectrally narrow transmission

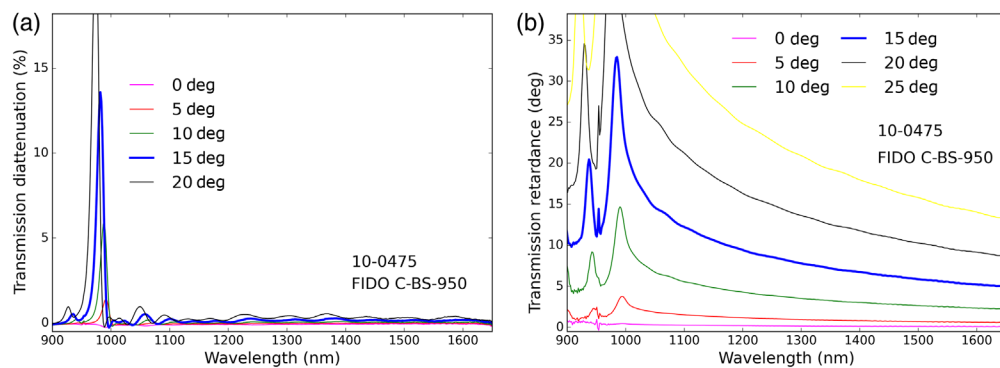


Fig. 75 The FIDO 950 coating data from coating run 10-0475 on the full sized part in transmission measured with our Boulder based NLSP. Each color shows a different incidence angle. (a) The diattenuation and (b) retardance.

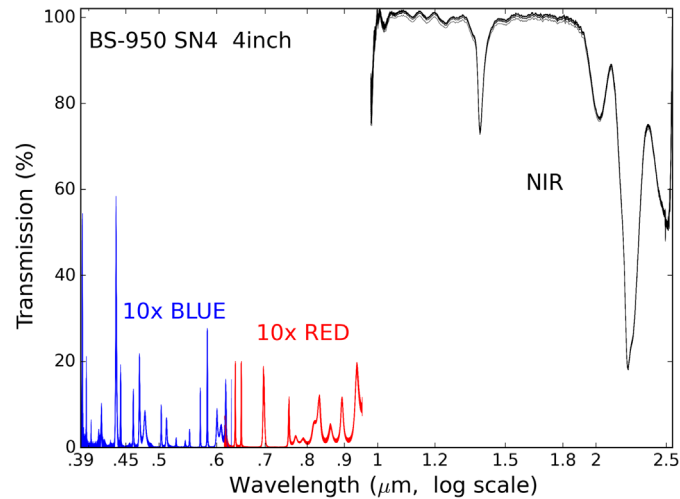


Fig. 76 Transmission spectra for BS-950 stress test sample SN4 recorded over a 100-mm aperture using our NDSP3 system. The blue line and red line show 10× the transmission measured with the blue and red spectrographs, respectively. The black curve shows the NIR spectrograph data.

leaks of few percent magnitude easily visible in the graphic. We note that this test sample did not use IR grade low OH fused silica giving rise to the spectral absorption bands seen at 1.4 μm and wavelengths beyond 2 μm .

The wavelength-dependent behavior of the transmission spatial variation is characterized by low order functions. Figure 77 shows example transmission spatial variation maps recorded with NDSP3 in spring of 2021. We choose three wavelengths as typical of the BS-950 dichroic coating at NIR wavelengths measured in NDSP3. Gradients across the aperture are obvious but the orientation of these features does change with wavelength.

7.5.5 BS-950 coating polarization in reflection: repeatability of narrow spectral features

The samples for BS-950 coating runs in chamber 10-number 0193, 0194, and 0195 were measured with NLSP in a K-cell configuration. Three DKIST silver witness samples were used initially from the M10 coating run with spatial positions in the ordering 9, unknown, 12. This provides a known and spectrally smooth polarization curve with almost all the polarization contributions from the two outer mirrors at high incidence angles. From our previous setup shown in Fig. 48 of Ref. 86, we estimate the inner K-cell optic is at incidence angles between

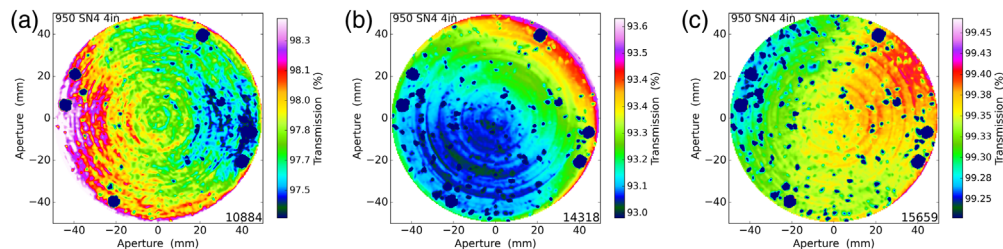


Fig. 77 The spatial variation of transmission over a 100-mm-diameter aperture measured with NDSP3 for a preliminary coating stress test on the C-BS-950 dichroic formula (run number 10-xxx stress sample SN4). There are a series of square and circular dots on the outer edge of the aperture used to co-align the interferometric wavefront measurements that show up as nearly zero transmission. (a) 1088.4 nm, (b) 1431.8 nm, and (c) 1565.9 nm. The color scale has been set as the median of the transmission over the aperture with a scale of (a) $\pm 1.5\%$ and (b), (c) $\pm 0.3\%$. Note that the general form of the spatial variation is a strong function of wavelength.

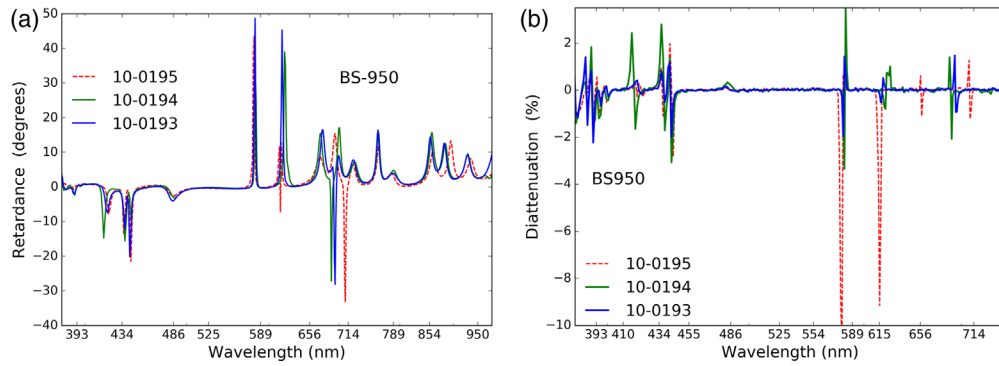


Fig. 78 (a) The retardance in transmission for the BS-950 dichroic chamber 10 coating runs 0193, 0194, and 0195 done in a K-cell configuration. (b) The diattenuation in transmission. (a), (b) The narrow spectral features estimated by comparing K-cell this configuration with the configuration using metal-coated mirrors.

9 deg and 11 deg while the two outer mirrors are within 1-deg of 50-deg incidences. Figures 78(a) and 78(b) show retardance and diattenuation, respectively, for the K-cell setup after subtracting out the three mirror K-cell polarization properties. Narrow spectral features are seen at ± 50 deg retardance and $\pm 3\%$ diattenuation even at this low incidence angle.

7.6 Antireflection: WBBAR1 on WFC-BS1, PA&C Window, and Tests

WBBAR1 is a 16-layer coating used on the back surface of WFC-BS1, some PA&C system windows, and other test optics. The coating design starts with a strippable layer, then 14 layers oscillating between SiO_2 and HfO_2 , ending with a MgF_2 outer layer. The coating design is $0.76 \mu\text{m}$ total physical thickness. Figure 79 shows the reflectivity measured for several coating runs including metrology on the as-delivered WFC-BS1 optic. We had previously described initial test on this coating in Figs. 69–71 of Ref. 86. We highlight here the WFC-BS1 optic now coated and permanently mounted within DKIST used in the initial on-sun observing campaigns.

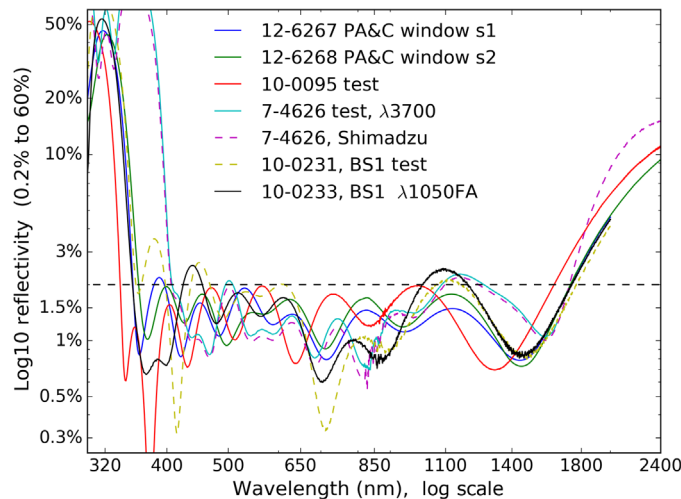


Fig. 79 Reflectivity for the WBBAR1 16 layer coatings measured by IOI at 6-deg incidence and roughly 2-nm slit bandwidth. This coating covers the BS used with the wavefront sensor for the AO system (WFC-BS1). The nominal absolute value specification of 2% reflectivity or below at any individual wavelength from 390 to 1600 nm is shown as the horizontal dashed line. Three different spectrophotometry tools were tested: a Shimadzu, a Lambda Research 1050FA and 3700 systems. We also tested the formula in chambers 7, 10, and 12. Significant spectral ripple variability was observed.

7.7 Antireflection: WBBAR1n on FIDO Windows, Dichroic BS-465, and BS-555

The spectral oscillations in the WBBAR1 coating prompted a coating design change before coating the FIDO windows and dichroics. The WBBAR1 design was a SiO_2 - HfO_2 14-layer stack with a strippable layer and outer MgF_2 layers for 16-total layers at $0.76 \mu\text{m}$ total physical thickness. The new WBBAR1n design has the same 16-total layer design but at $0.69 \mu\text{m}$ total physical thickness. The new WBBAR1n design is an oscillating $\text{MgF}_2 - \text{Ta}_2\text{O}_5$ stack with a strippable layer and similar outer MgF_2 layer. The design targets remain the same at an average reflectivity below 1.5% and no single peak above 2% in the 380- to 1650-nm wavelength range.

In Table 15, we compile the FIDO system optics this antireflection coating formula. The second column shows which side of the optic is coated. The third column shows the coating chamber and run number. The two FIDO windows C-W1 and C-W3 were coated at the same time. Both surfaces were coated. The FIDO window C-W2 was only back-side-coated at a later date.

Figure 80 shows the TFCalc design covering the full DKIST wavelength range along with the IOI spectrophotometry in reflection. In the right-hand graphic, we show a wide spectral range and include both the TFCalc design and many coating test runs. In the left-hand graphic, we only show the as-coated DKIST optics highlighting the design transmission bandpass. Note that the back side coating on the BS-555 shows a large artifact around the 850-nm grating changeover wavelength.

7.8 Antireflection: WBBAR2 for FIDO Dichroics 643, 680, 950

The WBBAR2 coating is nominally designed for the 630 to 1800 nm bandpass. It is intended for use only on the back surfaces of the longer wavelength FIDO dichroics, which reflect wavelengths shorter than 630 nm. The coating is nominally eight oscillating layers of SiO_2 and ZrO_2 with a MgF_2 outer layer and thin strippable layer at the glass interface. The coating design is $0.79 \mu\text{m}$ total physical thickness.

Figure 81 shows the reflectivity of WBBAR2 measured at IOI for various coatings done to date. Initial coating stress tests of the BS-950 dichroic coating called for six repeated WBBAR2 coatings on the back sides. Table 16 lists these six WBBAR2 coating runs in chamber 10 with serial numbers between 0180 and 0188 performed in fall of 2018. IOI measured reflectivity for *S*- and *P*-polarization states with a Lambda-1050 URA spectrograph at 12 deg incidence covering 300 to 2000 nm. Additional WBBAR2 coating runs have been performed since for additional coating design and stress testing of other FIDO formulas.

Table 15 WBBAR1n.

Optic	Side	Run
C-W1	Front	10-0261
C-W1	Back	10-0263
C-W3	Front	10-0261
C-W3	Back	10-0263
C-W2	Back	10-0289
ST-555	Back	10-0229
BS-555t	Back	10-0292
BS-555	Back	10-0360
ST-465	Back	10-0337
BS-465	Back	10-0372

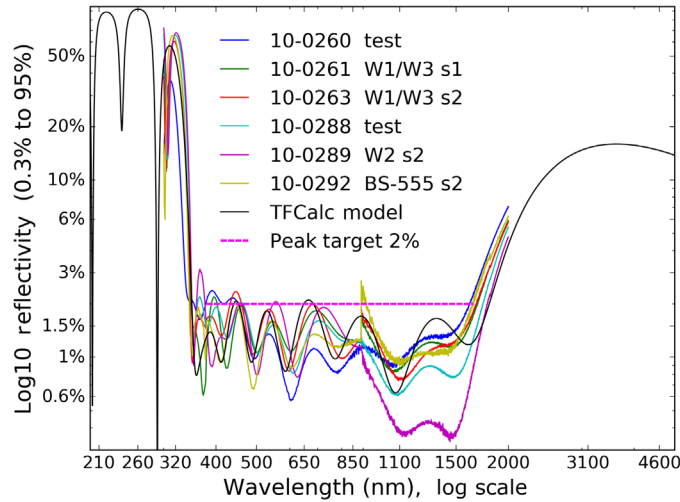


Fig. 80 The WBBAR1N reflectivity from the TFCalc design and compiled IOI spectrophotometry. The magenta horizontal dashed line shows a 2% threshold specified for the transmission band-pass 390 to 1600 nm. The nominal TFCalc coating model is shown as the solid black line. This 16-layer coating uses different materials and delivered somewhat less variable spectral ripples. The FIDO windows C-W1 and C-W3 were coated in the same chamber shots for the two respective sides of the optic (s1/s2). FIDO window C-W2 and BS BS-555 have this formula on the back surface. Two additional coating tests are also shown.

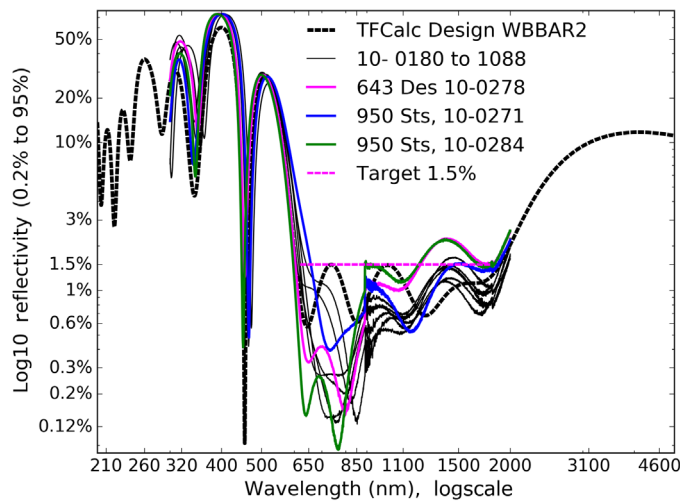


Fig. 81 Reflectivity measured by IOI at 12-deg incidence for several WBBAR2 coating shots at a slit bandwidth around 2 nm. The horizontal dashed magenta line shows the specification of less than 1.5% peak reflection at any individual wavelength between 630 and 1800 nm. These coatings were optimized for the BSs with 643, 680, and 950 nm wavelengths. The coating TFCalc design model is shown as the thick dashed line.

7.9 Substrate Internal Transmittance and Fresnel Losses: Heraeus Infrasil

The internal transmission losses can be computed with Beers law through absorption coefficients derived from the Heraeus catalog transmission values using their standard 10-mm-thick Infrasil 301 model. Figure 82 shows the internal transmittance for Heraeus Infrasil for the 12.5-mm-thick ViSP slit, the 35-mm-thick WFC-BS1 substrate, and the 43-mm-thick FIDO beamsplitter and window substrates. The vendor model for a 10-mm-thick glass substrate was converted to internal absorption coefficients and then propagated for the ViSP Slit, WFC-BS1, and FIDO substrates at 12.5, 35, and 43 mm thicknesses, respectively. These substrates were then interpolated onto our wavelength array and combined to show the transmission losses from glass absorption

Table 16 WBBAR2.

Optic	Side	Run
Stress 950	Unif.	10-0180
Stress 950	Unif.	10-0181
Stress 950	Unif.	10-0182
Stress 950	Unif.	10-0186
Stress 950	Unif.	10-0187
Stress 950	Unif.	10-0188
Stress 950	Back	10-271
Stress 950	Back	10-284
Des. 643	Back	10-0278
BS-643	Back	10-0481
BS-680	Back	10-0500
BS-950t	Back	10-0346
BS-950	Back	10-0471

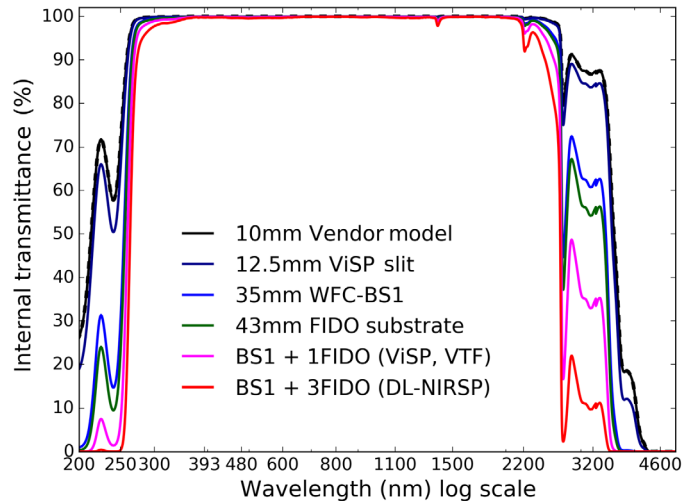


Fig. 82 The internal transmittance for Heraeus Infrasil of various thicknesses. Black shows the catalog transmission for 10 mm glass thickness. This vendor curve was expanded to all other thicknesses. Dark blue shows 12.5 mm thickness. Blue shows 35 mm thickness. Green shows 43 mm thickness. WFC-BS1 combines with one FIDO substrate to feed ViSP and VTF, giving the magenta absorption curve. The transmission to DL-NIRSP includes two more substrates at 43 mm thickness each, shown in the red curve with absorption above 80% for wavelengths longer than 2500 nm.

for the combinations of BSs in the various coudé pathways. Absorption losses vary significantly for wavelengths below 300 nm and above 2200 nm. Each substrate must also include the appropriate coatings over the entire bandpass on both surfaces in optic transmission. The Fresnel surface losses are computed for a single surface reflection from the refractive index model. For wavelengths longer than 3000 nm, fused silica becomes absorptive and the refractive index begins to vary quite widely (e.g., Ref. 99). For the purpose of our flux budget, we just replicate

the 3000 nm value to all longer wavelengths. Absorption and coating uncertainties are much greater than the surface reflection for this highly absorptive bandpass. We note that BS-643, BS-680, and C-W2 are a synthetic Suprasil 3002 variant due to particular schedule and procurement issues during the project but with identical performance parameters to natural fused silica to many decimal places.

7.10 Thorlabs: Commercial Off the Shelf Dichroics

Commercial dichroics often have narrow spectral features, similar to the DKIST FIDO dichroics and DL-NIRSP beam splitting dichroics. The thicker the coating, the narrower the spectral features can become. We compare in this appendix two commercial coatings bought from a Thorlabs catalog.

7.10.1 Thorlabs DMSP1000L short pass dichroic mapping at 0 deg and 45 deg incidence

We purchased a 50-mm-diameter DMSP 1000L part for lab use and demonstration testing. The Thorlabs commercial dichroic shows similar behavior as expected for the DKIST FIDO dichroics as well as the DL-NIRSP instrument dichroics. We show additional examples of the spatial nonuniformity in the nominal transmission band as well as other bandpasses.

The specification was at a design incidence angle of 45 deg for a transmission band in the 520 to 985 nm wavelength range. The transmission spec stated a bandpass average above 90% with an absolute value spec where any individual wavelength would be above 85% ($T_{\text{avg}} > 90\%$, $T_{\text{abs}} > 85\%$). The reflection bandpass covered 1020 to 1550 nm with only an absolute value specification above 90% ($R_{\text{abs}} > 90\%$). We mapped one of these parts first over a 45-mm aperture using the rosette spatial pattern at 1.5 mm step size with a 2.0-mm-diameter optical beam. We use normal incidence of 0 deg to provide the lowest systematic error limits in our NDSP3 system with a large circular aperture. We also did spatial mapping over a 44-mm aperture with a rosette spatial pattern and a 1.0-mm step size with the same 2.0-mm diameter beam. We see an elliptical aperture in projection and see systematic errors caused by the beam translation through a 45-deg tilted 2-mm thick glass substrate. We note that the dichroic would not be expected to pass specification at 0 deg incidence as many-layer coatings often are designed for a single incidence angle.

The coating bandpasses shift strongly with incidence for thick coatings and the spectral features are expected to grow large. Figure 83(a) shows example transmission spectra across the circular aperture for the 0-deg incidence case. Figure 83(b) shows example transmission spectra across the circular aperture for the 45-deg incidence case. The NDSP3 configuration from spring 2021 is more sensitive to beam alignment changes. A 45-deg substrate translates the collimated beam. We apply a correction to the three separate spectrographs, scaling the three units by a

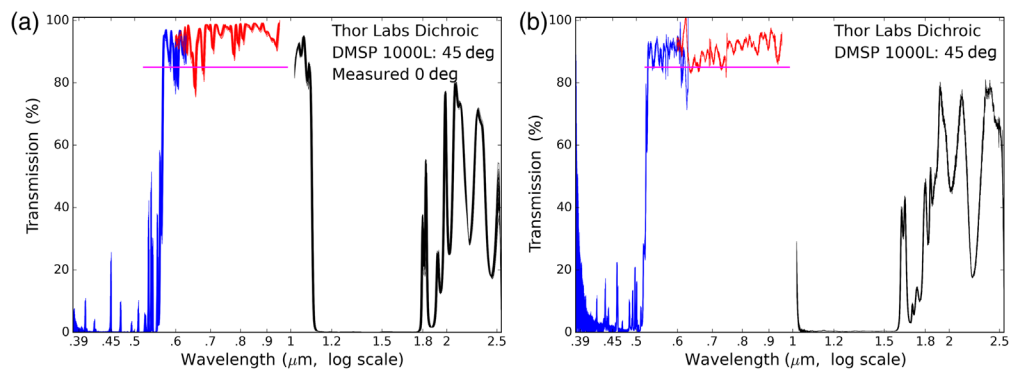


Fig. 83 Transmission spectra across the aperture for the Thorlabs dichroic DMSP 1000L mapped in NDSP3. (a) The 0-deg AOI spectrum. (b) The dichroic coating is designed for 45-deg AOI with measurements at 45 deg.

constant factor to show spectral continuity and similar behavior to our more accurate 0 deg measurements. We note that the constant scaling will not impact the aperture spatial variation nor the spectral features seen at adjacent wavelengths within the same spectrograph. We show both incidence angles here as the systematic errors in absolute transmission are larger with higher incidence angles on thicker substrates. The spatial maps derived in both cases, however, detect significant and repeatable spatial variation.

The top row of Fig. 84 shows three select spatial maps in the normal transmission band wavelengths of 654.9 in the left, 666.5 nm in the middle, and 677.2 nm in the right. This represents transmission uniformity in the nominal transmission bandpass. The bottom row of Fig. 84 shows three select spatial maps at closely spaced wavelengths of 492.4 in the left, 493.6 nm in the middle, and 493.9 nm in the right in the reflection bandpass. A high spectral-resolving power instrument working at this particular bandpass would see strong aperture spatial variation in transmission and significant leakage in a dichroic nominally blocking in this bandpass. This strong change in transmission across the aperture over just 1.9 nm wavelength would average substantially for systems with spectral resolving power below $R = 300$.

Measuring at 45-deg incidence, the coating nonuniformity is still present and at similar magnitudes over an elliptical projected aperture. We show in the top row of Fig. 85 example aperture transmission spatial variation maps at a few select wavelengths at the design 45-deg incidence angle chosen to match Fig. 84. There is clear aperture variation in transmission at levels of more than 3% peak-to-peak. Some wavelengths are more uniform than Fig. 84, but the aperture variation spectrally oscillates between more and less spatially uniform. The bottom row of Fig. 85 shows three select spatial maps chosen to match Fig. 84 as similar as possible using closely spaced wavelengths of 491.2 in the left, 491.9 nm in the middle, and 493.1 nm in the right.

7.10.2 Thorlabs DMLP567L long pass dichroic mapping at 0 deg incidence

We show another Thorlabs commercial dichroic as an example of smoother spectral performance and alternate design sensitivity. This design likely has fewer layers and lower thickness, given the wider spectral features resolved in our measurements. We choose a 2-in.-diameter DMLP567L as a long pass style dichroic mirror with a transition wavelength of 567 nm. This part nominally has guaranteed performance for reflection in the 380 to 550 nm bandpass and for transmission in the 584 to 800 nm bandpass.

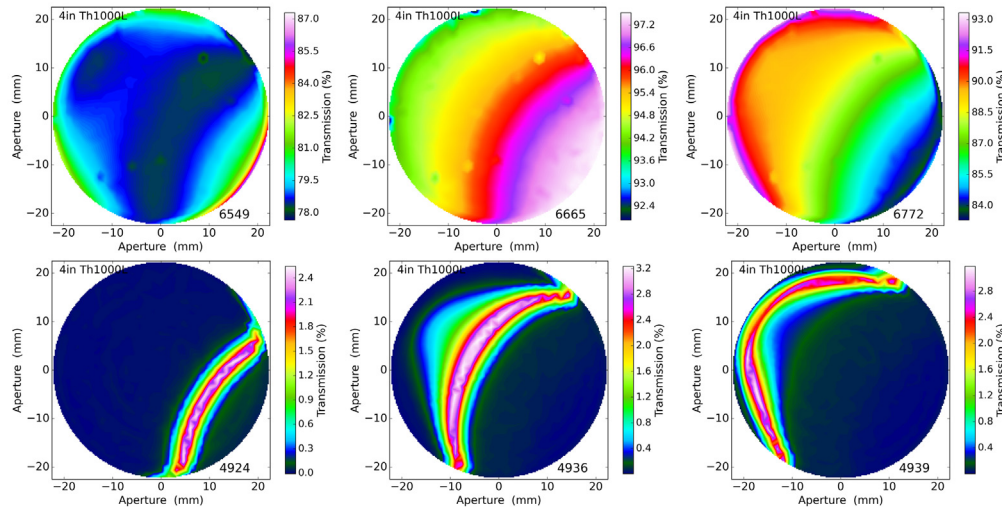


Fig. 84 The spatial variation of transmission over a 45-mm-diameter aperture measured with NDSP3 for a Thorlabs DMLP567L dichroic at a few closely spaced wavelengths in the guaranteed transmission bandpass of 520 to 985 nm. We note that the part is designed for 45-deg incidence to guarantee performance within 520 to 985 nm. We are measuring at 0 deg incidence which would change transmission properties. Coating nonuniformities, however, are detectable at all incidence angles.

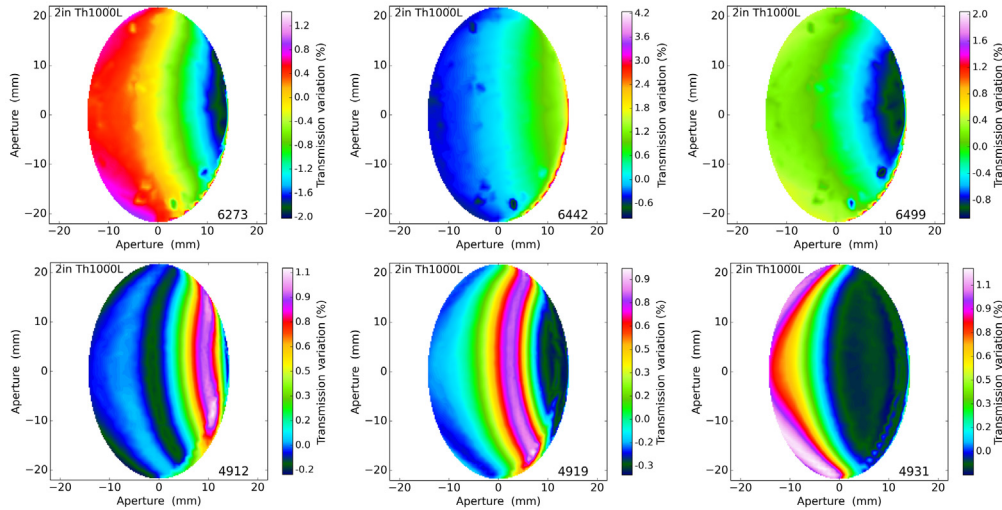


Fig. 85 The spatial variation of transmission over a 44-mm-diameter aperture measured with NDSP3 for a Thorlabs DMSP 1000L dichroic at a few closely spaced wavelengths in the reflection bandpass. The part is designed for 45-deg incidence and this graphic is measuring at 45-deg incidence. Coating nonuniformities, however, are detectable at all incidence angles.

We show the transmission spectra measured in NDSP3 at 0 deg incidence in Fig. 86 from spring 2021. The reflection bandpass is visible wavelengths short of 550 nm with the transmission band to roughly 850 nm. The IR performance was uncontrolled. In the transmission spectrum, we see some spectrally broad (>10 nm) spectral features in the reflection bandpass representing mild leaks. The transmission band also has spectral oscillations over 10% but similarly broad spectral features.

Figure 87 shows four select spatial maps of transmission across the aperture. We choose wavelengths to highlight the spatial variation in each bandpasses. The left-hand graphic shows 516.0 nm representing a transmission leak in the reflection band but with less than 0.2% amplitude. The second graphic shows 580.0 nm wavelength in the transition bandpass with a similar spatial pattern but much larger magnitude variations close to 4% peak-to-peak transmission. The third graphic shows the transmission band at 652.2 nm. There is a large transmission leak of over 10% outside an 80% clear aperture region that is off the color scale. The rest of the aperture shows transmission spatial variation at roughly 1% peak-to-peak amplitudes. The right-most

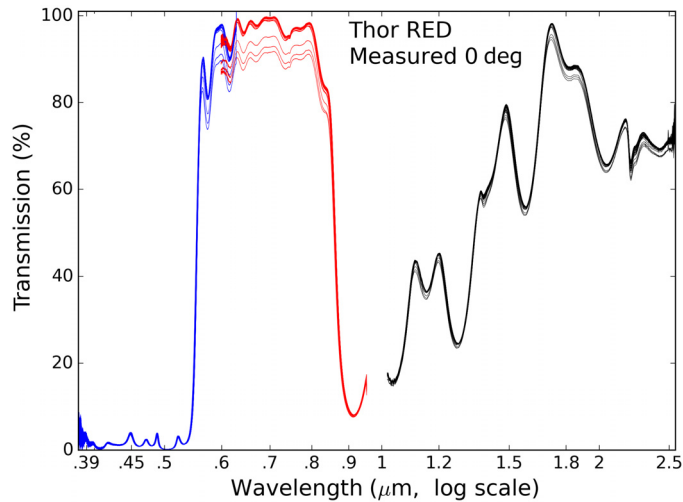


Fig. 86 Transmission across the aperture for the Thorlabs red dichroic mapped in NDSP3. We show the 0-deg AOI spectrum with constant spectral scaling applied to data from each of the three spectrographs. The coating is designed for 45-deg AOI.

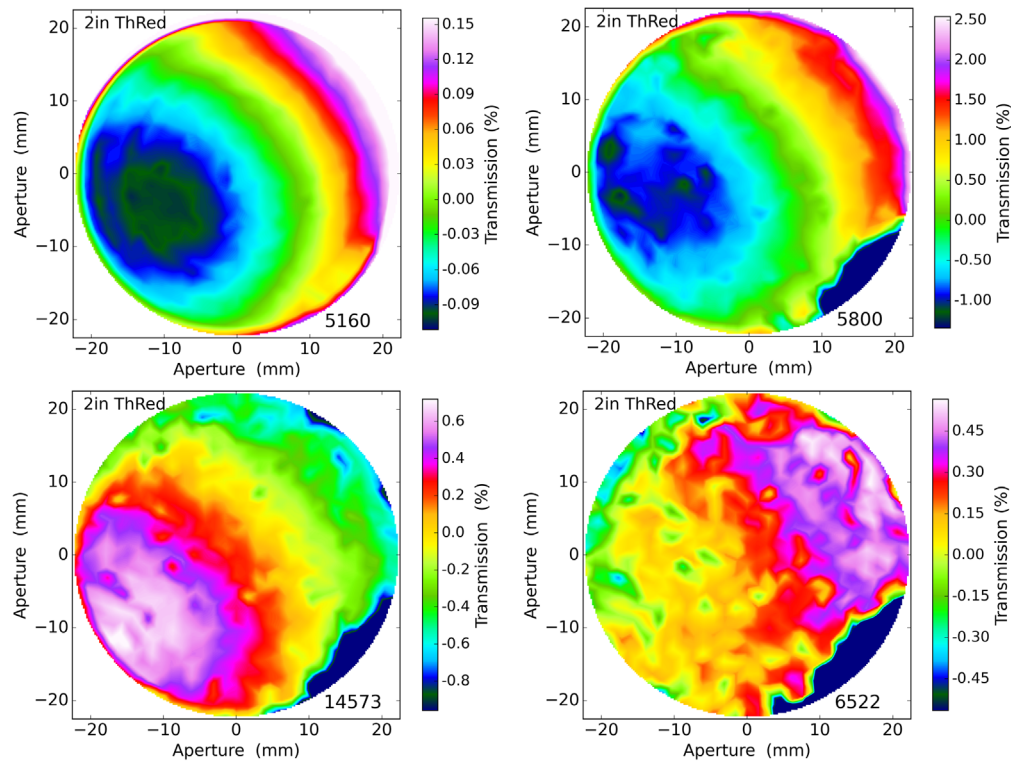


Fig. 87 The spatial variation of transmission over a 45-mm diameter aperture measured with NDSP3 for a 2-in.-diameter Thorlabs DMLP567L red dichroic at four select wavelengths in the different design bandpass. The part is designed for 45-deg incidence with a transition wavelength of 567 nm. This graphic shows measurements at 0-deg incidence. Wavelengths are 516.0, 580.0, 652.2, and 1457.3 nm.

graphic shows 1457.3 nm wavelength where this dichroic has a roughly 50% transmission and 50% reflection with spatial variation of transmission across the aperture at more than 1.5%.

Acknowledgments

This work was supported by the National Science Foundation's (NSF's) Daniel K. Inouye Solar Telescope project (DKIST). DKIST was operated by NSF's National Solar Observatory under a cooperative agreement with the Association of Universities for Research in Astronomy, Inc. (AURA). DKIST was located on land of spiritual and cultural significance to Native Hawaiian people. The use of this important site to further scientific knowledge is done so with appreciation and respect. We are honored to have the opportunity to conduct astronomical research on Haleakala on the Island of Maui in Hawaii. We recognize and acknowledge the very significant cultural role and reverence that this site has to the Native Hawaiian community. This project would not have been possible without the massive effort of the DKIST construction team. In particular, the summit team for their dedication and for dealing with all the challenges from building such a complex custom facility. We thank the DKIST M1 coating and recoating teams including Chen Liang, Predrag Sekulic, and Erik Starman. We thank Tom Schneider at Gemini Hilo for M1 sample reflectance measurements. We thank Peter Onaka and the University of Hawaii PanStarrs project for providing coating information. We thank Roberto Casini and Alfred de Wijn at the High Altitude Observatory for working with us on the ViSP optical system. We thank Sarah Jaeggli for discussions of the DL-NIRSP and for providing coating samples. We thank David Elmore for his contributions to the FIDO system initial layout and functional design. We thank the members of the DKIST Science Working Group for their participation in scoping the required dichroic use cases. Amanda White acknowledges funding from the George Ellery Hale Graduate Fellowship at the University of Colorado Boulder. This research made use of Astropy, a community-developed core Python package for Astronomy.^{100,101}

References

1. T. R. Rimmele et al., “The Daniel K. Inouye solar telescope: observatory overview,” *Solar Phys.* **295**, 172 (2020).
2. S. L. Keil et al., “ATST: the largest polarimeter,” in *Proc. Conf. Solar Polariz. 6*, Maui Vol. 437, p. 319 (2011).
3. T. R. Rimmele et al., “Instrumentation for the advanced technology solar telescope,” *Proc. SPIE* **5492**, 944 (2004).
4. J. Marino, E. Carlisle, and D. Schmidt, “Simulation of DKIST solar adaptive optics system,” *Proc. SPIE* **9909**, 99097C (2016).
5. J. P. McMullin et al., “Construction status of the Daniel K. Inouye solar telescope,” *Proc. SPIE* **9906**, 99061B (2016).
6. L. C. Johnson et al. “Status of the DKIST system for solar adaptive optics,” *Proc. SPIE* **9909**, 99090Y (2016).
7. D. F. Elmore, S. R. Sueoka, and R. Casini, “Performance of polarization modulation and calibration optics for the Daniel K. Inouye Solar Telescope,” *Proc. SPIE* **9147**, 91470F (2014).
8. D. F. Elmore et al., “The Daniel K. Inouye Solar Telescope first light instruments and critical science plan,” *Proc. SPIE* **9147**, 914707 (2014).
9. P. Sekulic et al., “Daniel K. Inouye Solar Telescope optical alignment plan,” *Proc. SPIE* **9906**, 990653 (2016).
10. R. Hubbard, S. Craig, and R. Kneale, “Daniel K. Inouye Solar Telescope systems engineering update,” *Proc. SPIE* **9911**, 99112F (2016).
11. S. R. Sueoka, R. A. Chipman, and D. F. Elmore, “Characterization of DKIST retarder components with polarization ray tracing,” *Proc. SPIE* **9293**, 929308 (2014).
12. D. F. Elmore et al., “Utilization of redundant polarized solar spectra to infer the polarization properties of the new generation of large aperture solar telescopes,” *Proc. SPIE* **7735**, 77354E (2010).
13. D. Elmore, “Telescope calibration using polarization calibration data,” *Astron. Nachr.* **331**(6), 655–657 (2010).
14. S. Sueoka, “Polarization optical components of the Daniel K. Inouye Solar Telescope,” PhD thesis, University of Arizona (2016).
15. J. C. Guzman and J. Ibsen, Eds., *Motor Control for 0.1-Meter Diameter Crystal Retarders on the Daniel K. Inouye Solar Telescope*, SPIE (2018).
16. A. Ferayorni et al., “DKIST controls model for synchronization of instrument cameras, polarization modulators, and mechanisms,” *Proc. SPIE* **9152**, 91520Z (2014).
17. W. Schmidt et al., “End-to-end simulations of the visible tunable filter for the Daniel K. Inouye Solar Telescope,” *Proc. SPIE* **9908**, 99084N (2016).
18. W. Schmidt et al., “A two-dimensional spectropolarimeter as a first-light instrument for the Daniel K. Inouye Solar Telescope,” *Proc. SPIE* **9147**, 91470E (2014).
19. F. Woeger et al., “The Daniel K. Inouye Solar Telescope (DKIST)/visible broadband imager (VBI),” *Solar Phys.* **296**, 145 (2021).
20. F. Wöger, “DKIST visible broadband imager interference filters,” *Proc. SPIE* **9147**, 91479I (2014).
21. A. Ferayorni et al., “Bottom-up laboratory testing of the DKIST Visible Broadband Imager (VBI),” *Proc. SPIE* **9911**, 991106 (2016).
22. A. Beard, B. Cowan, and A. Ferayorni, “DKIST visible broadband imager data processing pipeline,” *Proc. SPIE* **9152**, 91521J (2014).
23. P. Sekulic et al., “DKIST visible broadband imager alignment in laboratory: first results,” *Proc. SPIE* **9908**, 99085A (2016).
24. A. Ferayorni, “Instrument control software for the Visible Broadband Imager using ATST common services framework and base,” *Proc. SPIE* **8451**, 845113 (2012).
25. F. Wöger and A. Ferayorni, “Accelerated speckle imaging with the ATST visible broadband imager,” *Proc. SPIE* **8451**, 84511C (2012).
26. W. R. McBride et al., “ATST visible broadband imager,” *Proc. SPIE* **8446**, 84461B (2012).

27. L. C. Johnson et al., “Quasi-static wavefront control for the Advanced Technology Solar Telescope,” *Proc. SPIE* **8444**, 84443O (2012).
28. L. C. Johnson et al., “Solar adaptive optics with the DKIST: status report,” *Proc. SPIE* **9148**, 91481S (2014).
29. K. Richards et al., “The adaptive optics and wavefront correction systems for the Advanced Technology Solar Telescope,” *Proc. SPIE* **7736**, 773608 (2010).
30. J. Marino, “Expected performance of solar adaptive optics in large-aperture solar telescopes,” *Opt. Eng.* **51**(10), 101709 (2012).
31. D. Schmidt et al., “A review of solar adaptive optics,” *Proc. SPIE* **9909**, 99090X (2016).
32. H. Socas-Navarro et al., “High precision polarimetry with the Advanced Technology Solar Telescope,” *Proc. SPIE* **5901**, 590105 (2005).
33. S. Berukoff et al., “Petascale cyberinfrastructure for ground-based solar physics: approach of the DKIST data center,” *Proc. SPIE* **9913**, 99131F (2016).
34. F. T. Watson et al., “Calibration development strategies for the Daniel K. Inouye Solar Telescope (DKIST) data center,” *Proc. SPIE* **9910**, 99101G (2016).
35. C. Mayer, S. Wampler, and B. Goodrich, “World coordinate information for the Daniel K. Inouye Solar Telescope,” *Proc. SPIE* **9913**, 99130S (2016).
36. J. P. McMullin et al., “Construction status of the Daniel K. Inouye Solar Telescope,” *Proc. SPIE* **9145**, 914525 (2014).
37. W. H. Schubert, E. Petrak, and T. G. Baur, “Measurement of polarization assemblies for the Daniel K. Inouye Solar Telescope,” *Proc. SPIE* **9369**, 93690N (2015).
38. A. G. de Wijn et al., “Preliminary design of the visible spectro-polarimeter for the Advanced Technology Solar Telescope,” *Proc. SPIE* **8446**, 84466X (2012).
39. J. Sánchez-Capuchino et al., “Current concept for the 4m European Solar Telescope (EST) optical design,” *Proc. SPIE* **7733**, 773336 (2010).
40. F. C. M. Bettonvil et al., “The polarization optics for the European Solar Telescope (EST),” *Proc. SPIE* **7735**, 77356I (2010).
41. M. Collados et al., “European Solar Telescope: project status,” *Proc. SPIE* **7733**, 77330H (2010).
42. M. De Juan Ovelar et al., “Instrumental polarisation at the Nasmyth focus of the E-ELT,” *Astron. Astrophys.* **562**, A8–8 (2014).
43. F. Joos et al., “Reduction of polarimetric data using Mueller calculus applied to Nasmyth instruments,” *Proc. SPIE* **7016**, 70161I (2008).
44. C. U. Keller and F. Snik, “Polarimetry from the ground up,” in *Solar Polarization 5: In Honor Jan Stenflo ASP Conf. Ser.*, Vol. 405, p. 371 (2009).
45. C. U. Keller et al., “EPOL: the exoplanet polarimeter for EPICS at the E-ELT,” *Proc. SPIE* **7735**, 77356G (2010).
46. C. U. Keller, “Solar polarimetry close to the diffraction limit,” *Proc. SPIE* **4843**, 100 (2003).
47. M. Rodenhuis et al., “The extreme polarimeter: design, performance, first results and upgrades,” *Proc. SPIE* **8446**, 84469I (2012).
48. R. Roelfsema et al., “The ZIMPOL high-contrast imaging polarimeter for SPHERE: design, manufacturing, and testing,” *Proc. SPIE* **7735**, 77354B (2010).
49. J. Sánchez Almeida, “Instrumental polarization in the focal plane of telescopes. 2: Effects induced by seeing,” *Astron. Astrophys.* **292**, 713–721 (1994).
50. J. Sánchez Almeida and V. Martinez Pillet, “Instrumental polarization in the focal plane of telescopes,” *Astron. Astrophys.* **260**, 543–555 (1992).
51. J. Sánchez Almeida, V. Martinez Pillet, and A. D. Wittmann, “The instrumental polarization of a Gregory-coude telescope,” *Solar Phys.* **134**, 1–13 (1991).
52. W. Schmidt et al., “POLIS: a spectropolarimeter for the VTT and for GREGOR,” *Astron. Nachr.* **324**, 300 (2003).
53. F. Snik et al., “Design of a full-Stokes polarimeter for VLT/X-shooter,” *Proc. SPIE* **8446**, 844625 (2012).
54. F. Snik et al., “The upgrade of HARPS to a full-Stokes high-resolution spectropolarimeter,” *Proc. SPIE* **7014**, 70140O (2008).

55. F. Snik, “Calibration strategies for instrumental polarization at the 10^{-5} level,” *Proc. SPIE* **6269**, 62695P (2006).
56. H. Socas-Navarro et al., “Characterization of telescope polarization properties across the visible and near-infrared spectrum. Case study: the Dunn Solar Telescope,” *Astron. Astrophys.* **531**, 2 (2011).
57. H. Socas-Navarro, “Polarimetric calibration of large-aperture telescopes. II. Subaperture method,” *J. Opt. Soc. Am. A* **22**, 907 (2005).
58. H. Socas-Navarro, “Polarimetric calibration of large-aperture telescopes. I. Beam-expansion method,” *J. Opt. Soc. Am. A* **22**, 539 (2005).
59. P. Spano et al., “Optical design of CAOS: a high-resolution spectropolarimeter for the Catania Astrophysical Observatory 0.91-m telescope,” *Proc. SPIE* **5492**, 373 (2004).
60. K. G. Strassmeier et al., “PEPSI: the Potsdam Echelle polarimetric and spectroscopic instrument for the LBT,” *Proc. SPIE* **7014**, 70140N (2008).
61. K. G. Strassmeier et al., “PEPSI spectro-polarimeter for the LBT,” *Proc. SPIE* **4843**, 180 (2003).
62. J. Tinbergen, “Accurate optical polarimetry on the Nasmyth platform,” *Publ. Astron. Soc. Pac.* **119**, 1371–1384 (2007).
63. C. Beck et al., “A polarization model for the German Vacuum Tower Telescope from in situ and laboratory measurements,” *Astron. Astrophys.* **443**, 1047–1053 (2005).
64. C. Beck et al., “Polarimetric Littrow spectrograph: instrument calibration and first measurements,” *Astron. Astrophys.* **437**, 1159–1167 (2005).
65. L. Kleint et al., “GREGOR: optics redesign and updates from 2018–2020,” *Astron. Astrophys.* **641**, A27–A10 (2020).
66. D. M. Harrington and S. R. Sueoka, “Polarization modeling and predictions for DKIST part 1: telescope and example instrument configurations,” *J. Astron. Telesc. Instrum. Syst.* **3**, 018002 (2017).
67. D. M. Harrington, J. R. Kuhn, and A. L. Ariste, “Daytime sky polarization calibration limitations,” *J. Astron. Telesc. Instrum. Syst.* **3**, 018001 (2017).
68. M. Semel, “Spectropolarimetry and polarization-dependent fringes,” *Astron. Astrophys.* **401**, 1–14 (2003).
69. D. Clarke, “Interference effects in compound and achromatic wave plates,” *J. Opt. A: Pure Appl. Opt.* **6**, 1041–1046 (2004).
70. D. Clarke, “Effects in polarimetry of interference within wave plates,” *Astron. Astrophys.* **434**, 377–384 (2005).
71. D. Clarke, “Interference effects in single wave plates,” *J. Opt. A: Pure Appl. Opt.* **6**, 1036–1040 (2004).
72. D. Clarke, “Interference effects in Pancharatnam wave plates,” *J. Opt. A: Pure Appl. Opt.* **6**, 1047–1051 (2004).
73. D. Clarke, *Stellar Polarimetry*, John Wiley & Sons, Weinheim, Germany (2009).
74. O. S. Heavens, *Optical Properties of Thin Solid Films (Dover Books on Physics)*, Dover, New York (1965).
75. D. K. Aitken and J. H. Hough, “Spectral modulation, or ripple, in retardation plates for linear and circular polarization,” *Publ. Astron. Soc. Pac.* **113**, 1300 (2001).
76. T. J. Harries and I. D. Howarth, “Linear spectropolarimetry of the H α emission line of ζ Puppis,” *Astron. Astrophys.* **310**, 533 (1996).
77. D. M. Harrington et al., “Correcting systematic polarization effects in Keck LRISp spectropolarimetry to 0.05 percent,” *Publ. Astron. Soc. Pac.* **127**, 757–775 (2015).
78. F. Snik et al., “A multi-domain full-Stokes polarization modulator that is efficient for 300–2500 nm spectropolarimetry,” *Proc. SPIE* **9613**, 96130G (2015).
79. A. Derks, C. Beck, and V. Pillet, “Inferring telescope polarization properties through spectral lines without linear polarization,” *aanda.org* **615**, A22 (2018).
80. P. M. Rojo and J. Harrington, “A method to remove fringes from images using wavelets,” *Astrophys. J.* **649**, 553–560 (2006).
81. D. M. Harrington and S. R. Sueoka, “Polarization modeling and predictions for DKIST part 3: focal ratio and thermal dependencies of spectral polarization fringes and optic retardance,” *J. Astron. Telesc. Instrum. Syst.* **4**(01), 018006 (2018).

82. D. W. Berreman, "Optics in stratified and anisotropic media: 4X4-matrix formulation," *J. Opt. Soc. Am.* **62**, 502 (1972).
83. M. W. McCall, I. J. Hodgkinson, and Q. Wu, *Birefringent Thin Films and Polarizing Elements*, Vol. **1**, 2nd ed., Imperial College Press, London (2014).
84. D. M. Harrington et al., "Polarization modeling and predictions for DKIST part 6: fringe mitigation with polycarbonate modulators and optical contact calibration retarders," *J. Astron. Telesc. Instrum. Syst.* **6**, 038001 (2020).
85. D. M. Harrington and S. R. Sueoka, "Polarization modeling and predictions for DKIST part 4: calibration accuracy over field of view, retardance spatial uniformity, and achromat design sensitivity," *J. Astron. Telesc. Instrum. Syst.* **4**, 044006 (2018).
86. D. M. Harrington, S. R. Sueoka, and A. J. White, "Polarization modeling and predictions for DKIST part 5: impacts of enhanced mirror and dichroic coatings on system polarization calibration," *J. Astron. Telesc. Instrum. Syst.* **5**, 038001 (2019).
87. D. M. Harrington et al., "Polarization modeling and predictions for Daniel K. Inouye Solar Telescope, part 7: preliminary NCSP system calibration and model fitting," *J. Astron. Telesc. Instrum. Syst.* **7**, 018004 (2021).
88. D. M. Harrington et al., "Polarization modeling and predictions for DKIST, part 8: calibration polarizer spatial variation impacts," *J. Astron. Telesc. Instrum. Syst.* **7**, 038002 (2021).
89. J. B. Breckinridge, W. S. T. Lam, and R. A. Chipman, "Polarization aberrations in astronomical telescopes: the point spread function," *Publ. Astron. Soc. Pac.* **127**, 445–468 (2015).
90. J. B. Breckinridge et al., "Terrestrial exoplanet coronagraph image quality: study of polarization aberrations in Habex and LUVOIR update," *Proc. SPIE* **10698**, 106981D (2018).
91. R. A. Chipman, W. S. T. Lam, and J. Breckinridge, "Polarization aberration in astronomical telescopes," *Proc. SPIE* **9613**, 96130H (2015).
92. J. B. Breckinridge and B. R. Oppenheimer, "Polarization effects in reflecting coronagraphs for white-light applications in astronomy," *Astrophys. J.* **600**, 1091 (2004).
93. J. C. Carson et al., "The effects of instrumental elliptical polarization on stellar point spread function fine structure," *Proc. SPIE* **6265**, 62653M (2006).
94. J. Heath et al., "Mueller matrix maps of dichroic filters reveal polarization aberrations," *Proc. SPIE* **11443**, 1144341 (2020).
95. R. A. Chipman, W. S. T. Lam, and G. Young, *Polarized Light and Optical Systems*, CRC Press, Boca Raton, Florida (2018).
96. P. G. Nelson and R. Casini, "On the intensity distribution function of blazed reflective diffraction gratings," *J. Opt. Soc. Am. A* **31**, 2179–2184 (2014).
97. R. Casini et al., "Measured performance of shadow-cast coated gratings for spectro-polarimetric applications," *Appl. Opt.* **57**, 7276–7280 (2018).
98. G. van Harten, F. Snik, and C. U. Keller, "Polarization properties of real aluminum mirrors, I. Influence of the aluminum oxide layer," *Publ. Astron. Soc. Pac.* **121**, 377 (2009).
99. R. Kitamura, L. Pilon, and M. Jonasz, "Optical constants of silica glass from extreme ultraviolet to far infrared at near room temperature," *Appl. Opt.* **46**, 8118–8133 (2007).
100. T. A. Collaboration et al. "The Astropy project: building an inclusive, open-science project and status of the v2.0 core package," *Astron. J.* **156**(3), 123 (2018).
101. T. A. Collaboration et al., "Astropy: a community Python package for astronomy," arXiv.org, p. A33 (2013).

Biographies of the authors are not available.